1-1-2017

Elucidation Of The Cation And The Anion Doping Mechanism Of Nanoparticulate Manganese Arsenide: Effect Of Doping On The Magnetostructural Properties

Surangi Hasitha Roshini Pimmachcharige
Wayne State University,

ELUCIDATION OF THE CATION AND THE ANION DOPING MECHANISM OF NANOPARTICULATE MANGANESE ARSENIDE: EFFECT OF DOPING ON THE MAGNETOSTRUCTURAL PROPERTIES

by

ROSHINI PIMMACHCHARIGE

DISSERTATION

Submitted to the Graduate School

of Wayne State University,

Detroit, Michigan

in partial fulfillment of the requirements

for the degree of

DOCTOR OF PHILOSOPHY

2017

MAJOR: CHEMISTRY (Inorganic)

Approved By:

_____

Advisor Date

_____

_____

_____

DEDICATION

To my parents, my husband, son and daughter for their unconditional love

ACKNOWLEDGMENTS

I would like express my sincere gratitude to my research advisor Prof. Stephanie L. Brock for her motivation, guidance, and the enormous intellectual and moral support she extended during my stay at Wayne State University. I greatly appreciate her encouraging remarks and wonderful inputs she channeled to make my research work fruitful and keep me up to date with new science emerging in every minute. It was great to work with her and again I am really grateful to her for what I have achieved as a synthetic materials chemist.

I would like to take this opportunity to appreciate my dissertation committee members, Prof. Matthew Allen, Prof. Louis Romano, and Prof. Zhixian Zhou for their valuable advice, comments, which have served enormously to improve my research and the outcome of the dissertation. I am honored to have these faculty members in my dissertation committee. I would like to mention here about Prof. Gavin Lawes, who was a member of my dissertation committee but unfortunately had to be replaced due to his untimely departure. He has been one of the most admirable people to me.

Next, my thanks go to my collaborators Prof. Boris Nadgorny and his student, Ehab Abdelhamid, at the Department of Physics and Astronomy, Wayne State University. They helped me acquiring magnetic data of MnAs samples in timely manner. I greatly appreciate their contribution to this work and ideas and valuable information provided to get this work done in timely fashion.

I am grateful to Dr. Zhi Mei, the manager of electron microscopy facility of department of Chemistry, for helping me with TEM imaging and valuable suggestions. I also like to thank Dr. Mary Jane Heeg, Dr. Philip Martin, Dr. Yuriy Danylyuk for their help and training on how to use the X-ray diffractometers. My thanks also go to Dr. Olena Danylyuk and Dr. Johnna Birbeck for helping me with collecting ICP-MS data. I would like to thank all the office staff members of the Department of Chemistry, with especial mention to Melissa Barton and computer specialist Nestor Ocampo for their

support throughout my stay at Wayne State University. I received great help from past Brock group members: Dr. Shreyashi Ganguly, Dr. Irina Pala, Dr. Layan Savitrha, Dr. Yanhua Zhang, Dr. Lasantha Korala, Dr. Asha Bandara, Dr. Derak James, Dr. Ruchira Liyanage and Dr. Jessica Davis. I specially thank Dr. Shreyashi Ganguly and Dr. Yanhua Zhang for training me how to use inert atmosphere synthetic techniques. I greatly appreciate Dr. Asha Bandara who helped me in numerous ways since I came to Wayne State University. I would like to thank current Brock group members, Indika Hewavitharana, Da Li, Malsha Hettiarachchi, Samuel Mutinda, Lalani Pathmakumari, Lakmini Samantha and Tepora Su. They are great colleagues to work with and share research experience.

I take this moment to thank my parents for their wonderful support, love and encouragement. Their utmost guidance and care helped me to achieve so many things I have never thought of and to be a humble man. It is not complete if I do not mention my sister who has been with me whenever necessary throughout my life. I greatly respect and appreciate her commitment to take care of my parents on behalf of me.

Finally I thank my wonderful husband, Kasun, and my precious son and daughter, Vimukthi and Kaushi for their love, encouragement and patience expressed throughout my studies.

TABLE OF CONTENTS

LIST OF TABLES

LIST OF FIGURES

LIST OF SCHEMES

CHAPTER 1 INTRODUCTION

Nanomaterials exhibit distinct catalytic,[1,2] magnetic[3,4] and optical[5] properties compared to their bulk counterpart as a result of the large surface-to-volume ratio and changes in electronic/magnetic interactions on the nanoscale. Owing to these inherent properties, nanomaterials find applications in medicine,[6] energy,[7,8] and the environment.[9] Transition metal pnictides (transition metal compounds of group 15 elements) are a large group of materials with diverse properties relevant for technological applications. Applications in clean and renewable energy, energy storage, data storage and microclimate control[10,11]employing transition metal pnictides can benefit from controlling the structure and composition of the material on the nanoscale. However, nano scale transition metal pnictides are relatively unexplored due to challenges in the synthesis. Among transition metal pnictides, MnAs has been extensively studied in the bulk and as epitaxially produced thin films and dots because of its phase and composition dependant magnetic properties and potential applications in data storage/processing and magnetic refrigeration.[12,13] The Brock group has developed, for the first time, a solution-phase arrested precipitation method for MnAs that enables formation of nanoparticles without epitaxially induced strain, [14] and consequently, an understanding of the intrinsic effects of size on properties.

In this dissertation, the solution-phase growth mechanism of MnAs nanoparticles is determined and the effect of cation and anion doping on the magnetostructural properties of discrete nanoparticles is evaluated. This chapter introduces the general properties of nanoparticles, their synthesis and the magnetostructural characteristics of MnAs.

1.1. Transition metal pnictides

Depending on the phase and composition, transition metal pnictides exhibit physical properties including semiconductivity, ferromagnetism, thermoelectricity and superconductivity, that find wide range of potential technological applications. Scheme 1.1 summarizes some transition metal pnictides and their associated properties.

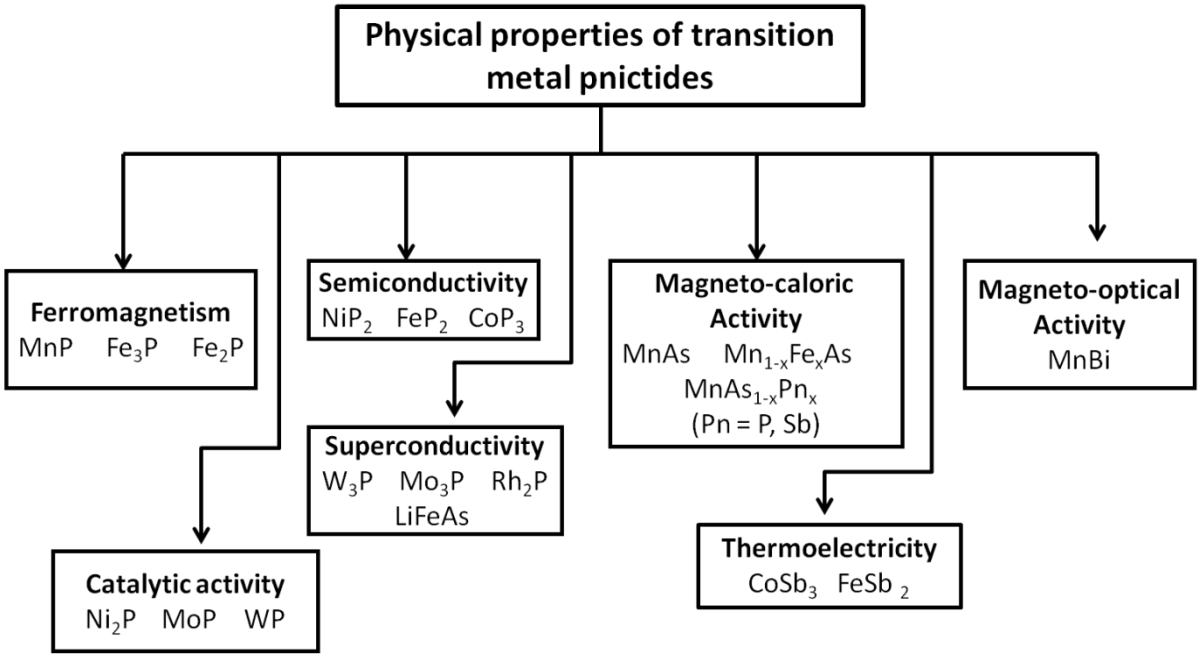

Scheme 1.1 Physical properties of transition metal pnictides and some examples (based on references [15, 13, 16, 17])

A considerable amount of research has been done on transition metal pnictides as bulk phases. However, a lack of synthetic methods to fabricate nanostructures has restricted research on transition metal pnictide nanomaterials. Among transition metal pnictides, phosphide based discrete nanoparticles have received much attention. However, studies on arsenide and antimonide based discrete nanostructures are rare despite their potential applications in superconductivity,[18,19] magnetic refrigeration[20] and optical fibers.[21] The focus of this dissertation is on manganese arsenide nanoparticles, a material extensively studied in its bulk phase for its potential applications in magnetic refrigeration and data storage.

1.2. Nanomaterials

Materials of which a single dimension is smaller than one tenth of a micrometer are defined as nanomaterials. Upon reducing the size down to the nanoscale, materials have a tendency to exhibit unique properties including, but not limited to, enhanced surface area (catalysis),[1,2] reduction in size (data storage, batteries),[22,23] enhanced surface functionalities (drug delivery),[24,25] and phonon scattering (thermoelectrics).[26] Top-down and bottom-up approaches are the frequently used synthesis methods for fabrication of nanomaterials. The top down approach involves milling or etching a bulk material to produce nanostructures. The bottom up approach involves building the nanomaterial from molecular precursors. A major disadvantage of top-down methods is the imperfections that can arise in the resultant nanostructures and/or epitaxial strain, which lead to challenges in device fabrication and characterization. A key advantage of the bottom-up method is the ability to control the size, composition and surface functionality.[27] A brief description of commonly used bottom-up and top-down methods for transition metal pnictides' synthesis are discussed in Section 1.3.

1.3. Synthesis of nanoparticles

Nanoparticles have been fabricated by using chemical and physical methods. Chemical syntheses of nanoparticles usually employ the bottom-up technique. Solvothermal methods[28] and the solution-phase arrested-precipitation (SPAP) methods[29,30] are chemical synthetic meathods that have been applied to formation of transition metal pnictides. Molecular beam epitaxy (MBE) and mechanochemical synthesis are the physical methods that have been employed for the fabrication of transition metal pnictide nanostructures.

1.3.1 Physical methods for the synthesis of nanoparticles

Physical methods for the synthesis of nanoparticles fall into two broad categories: mechanical synthesis and vapor methods. Mechanical methods utilize a top-down approach for preparation of nanostructures and ball-milling is one such technique. Sun and coworkers reported fabrication of polycrystalline $MnAs_{1-x}P_x$ by annealing Mn, As and P powders that had been mechanically alloyed by ball-milling.[31]

In vapor-based methods, the bottom-up approach is used for the fabrication of nanostructures, and molecular beam epitaxy (MBE) is one such method that is widely used to fabricate arsenide based nanomaterials. In general, vapor phase methods involve creating thermodynamically unfavorable conditions for the vapor phase mixture compared to the nanomaterial targeted for fabrication. Homogeneous nucleation takes place upon condensation of supersaturated vapor.[32]

The majority of MnAs films,[33] nanodots,[34] and disks[35] have been prepared using MBE. In addition, Ge/MnAs alloys,[36] GaAs nanowires[37] and InAs/InGaAs heterostructures[38] have been fabricated employing this synthesis method. MBE is an ultra-high-vacuum based method used for growing thin, epitaxial layers of a range of materials from metals to insulators and semiconductors. This technique employs molecular or atomic beams under ultra high vacuum to provide constituents to the growing surface of a heated crystalline substrate. MBE is based on a simple principle. It is similar to “spray painting” a substrate with layers of molecules or atoms. However, production of pure, uniform materials requires considerable technological effort. In this technique, precursors (atoms or molecules) are prepared from a solid source of interest and the beam of precursors travel through ultra high vacuum until they reach the heated substrate. The ultra high vacuum provides a collision free pathway for the precursors. The precursors that

don't reach the substrate are condensed by the chilled walls of the chamber and removed from the system. The purity of the prepared material depends on the quality of the material used for generation of precursors and the condition of vacuum. The system is equipped with a shutter that functions to turn off the beam instantly. This feature assists in controlling composition, uniformity, doping, and most importantly, growing of films as monolayers. Because MBE requires a substrate, the resulting structures are often subjected to epitaxial strain. Such epitaxial strain is demonstrated to strongly affect the properties of MnAs and related phases.

1.3.2 Chemical synthesis of nanoparticles

1.3.2.1 Hydrothermal and solvothermal synthesis

Hydrothermal synthesis involves an aqueous medium where materials are synthesized under high pressure and temperature. The high pressure and temperature environment is provided by employing an autoclave. Solvothermal methods differ from hydrothermal methods by using organic solvents in place of water.[39] In general, both synthesis methods involve maintaining the reaction mixture above the boiling point of solvents as the sealed autoclave provides high a pressure environment. Hydrothermal/solvothermal methods lack real time monitoring of the reaction, leading to challenges in probing the growth mechanism of the material. Thus, fine control of particle size, morphology and composition is often restricted with these techniques. Solvothermal and hydrothermal techniques are popular methods for the synthesis of metal pnictides and chalcogenides.[40,41]

While there are a few reports on the synthesis of main group metal arsenides employing hydrothermal/solvothermal methods, corresponding reports on synthesis of transition metal arsenides are relatively rare. Xie and coworkers reported synthesis of FeAs, CoAs and NiAs nanocrystals using solvothermal method.[42] During the reported synthesis, the chlorides of each

metal were held at 100 ^{o}C for extended time (4-24 hours) in a mixture of arsenic, KBH_4 and ethylenediamine. However, they reported the toxicity of the reaction as arsenic reacts with KBH_4.

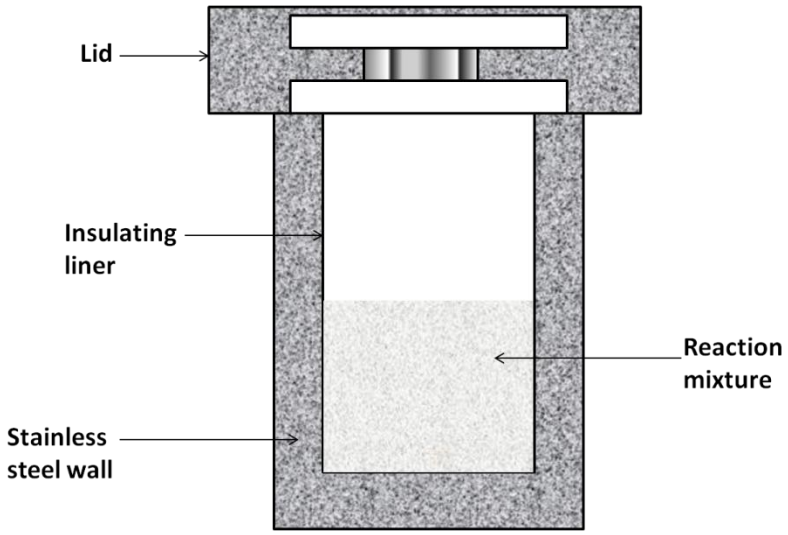

Figure 1.1 Schematic cross-section of an autoclave for hydrothermal/solvothermal synthesis (adapted from Onoki)[43]

1.3.2.2 Solution-phase arrested precipitation (SPAP) synthesis

In this dissertation study, the SPAP method is used for the synthesis of doped manganese arsenide nanoparticles by decomposition of organometallic precursors in high boiling-point solvents in the presence of coordinating ligands. The SPAP method is the most commonly used approach for the synthesis of metals, metal chalcogenides and metal pnictide nanoparticles as it facilitates fine control of particle size, size/morphology uniformity, composition and surface functionalities.[44,45] The SPAP method involves arresting the growth of nanoparticles by addition of inorganic coordinating agents, or organic ligands.[46] Our lab has pioneered the synthesis of discrete transition metal phosphides,[47,48] MnAs[14] and recently, MnSb,[49] using the SPAP method. Prior reports on the synthesis of MnAs and MnSb nanostructures were limited to their growth on substrates using physical methods.[50,51]

The SPAP technique is typically exploited in one of two ways: rapid addition of precursors into a hot coordinating solvent, or slow ramping of the temperature of the pre-mixed reaction mixture containing precursors and coordinating solvents. In the former method, the rapid introduction of reagents causes a burst of precursors, leading to a single, short, nucleation event. In the latter method, a burst of nucleation takes place due to decomposition of precursors as the temperature reaches a critical value. The SPAP technique in this dissertation study involves the former method.

Formation of monodisperse nanoparticles with rapid injection of precursors can be explained by the classical La Mer model for colloidal nanoparticle nucleation and growth.[52] As shown in Figure 1.2, rapid introduction of precursors followed by decomposition causes supersaturation of monomers. The supersaturation of monomers results in a burst of nucleation, which lowers the monomer concentration below the nucleation threshold as monomers are consumed to form nuclei. Below the nucleation threshold, new nuclei are not formed and the monomers add to existing nuclei leading to growth of nanoparticles. Alternately, slow ramping of temperature to the critical temperature at which precursors decompose results in a burst of nucleation. Recently, Desai et al.[53] reported the SPAP synthesis of FeAs nanoparticles with crystalline FeAs core and amorphous carbonaceous shell by injecting the Fe precursor into a hot mixture of hexadecylamine and triphenylarsine. Introduction of the Fe precursor results in a burst of Fe-rich nuclei that reacts with the As-precursor to produce FeAs nanoparticles.

Temperature control at the point of nucleation burst is critical to avoid additional nucleation, causing the monomer addition process to existing nuclei to occur faster than the formation of new nuclei. Hence, particle growth dominates at this stage. The concentration of monomers in the reaction mixture decreases as the nanoparticles grow, and the growth of

nanoparticles continues according to the Ostwald ripening mechanism (Figure 1.3) where larger particles grow at the expense of smaller particles.[54]

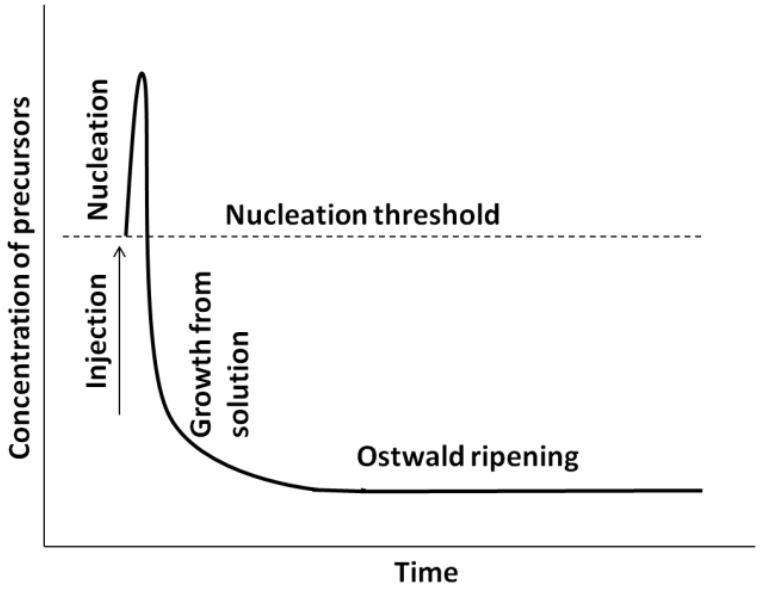

Figure 1.2 Schematic illustration of the La Mer model for nucleation and growth of colloidal nanocrystals (adapted from Klimov)[52]

In nanoparticle synthesis, the availability to tune the particle size, size distribution and morphology is critical. In general, higher growth temperatures, longer reaction times and higher monomer concentrations yield larger particles. However, Ostwald ripening also occurs with longer reaction time and higher temperatures, resulting in a broadening of size distribution. Post synthesis steps such as size selective precipitation allows narrow size distributions to be obtained.[55] Alternatively, arresting the reaction during the rapid growth stage (before Ostwald ripening) yields nanoparticles with narrow polydispersity

In the La Mer model, the overall nanoparticle growth process is thermodynamically controlled and the nanoparticles are spherical due to lower surface energy. In order to obtain nanoparticles with high anisotropy, the growth process needs to be in the kinetic growth regime.[56] In the kinetic growth regime, high-energy facets grow faster than low energy facets

yielding nanoparticles with highly anisotropic shapes. The high monomer concentration allows the kinetic growth regime to be accessed and introduction of surfactants that have a strong binding affinity to certain crystal facets can also facilitate the fine control of nanoparticle shape.[29]

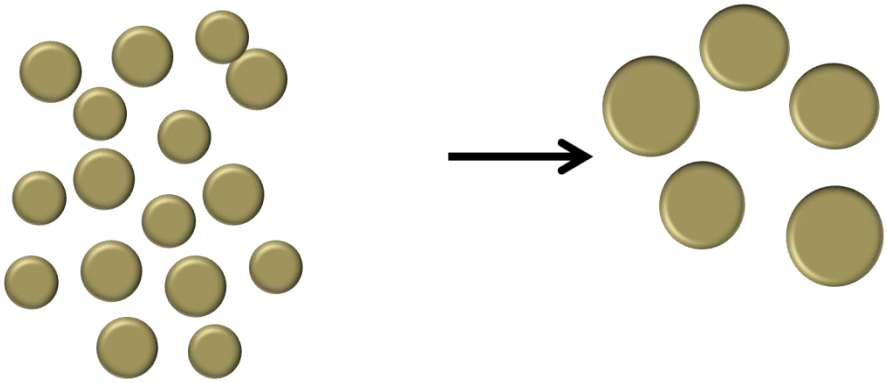

Figure 1.3 Schematic illustration of Ostwald ripening of nanoparticles

1.4. Doping of nanoparticles

In the process of tuning properties of nanoparticles, doping has become a well known technique. The interactions of dopant and the host species are responsible for the new properties observed in doped nanoparticles. The properties observed in doped nanoparticles with respect to their un-doped nanomaterial may be due to isolated electronic states,[57] spin exchange interactions between host and dopant species[58, 59] or structural defects.[60] Despite the advantages doped nanoparticles have to offer, doping on the nano scale is challenging partly due to the thermodynamically lower stability of doped nanoparticles compared to un-doped ones.[61] However, doping is possible during the nucleation and growth of host material, or by direct in situ doping, if the reactivities of dopant and host atoms are similar. Doping of nanoparticles could occur by trapping of the dopant during nucleation, whereas maintaining low reaction temperatures was found to prevent loss of the trapped dopant by self purification during the particle growth process.[62]

The majority of reports of doping on nanoparticles are on colloidal semiconductor nanocrystals, and reports on transition metal arsenides are rare. Recently, the Brock group reported adventitious P doping in discrete type-B MnAs nanoparticles (prepared by the hot injection process). The observed depression of T_C and phase co-existence in type-B MnAs nanoparticles was attributed to P doping.[63] In contrast, type-A MnAs nanoparticles synthesized by a slow heating method with same precursors and surfactants did not result in P incorporation and T_C was found to be similar to that of bulk MnAs. The difference between type-A and B MnAs nanoparticles reflect the influence of synthetic method and temperature on impurity trapping.

In addition to trapping of impurities at nucleation, inward diffusion of the dopant during particle growth can also result in doping.[62, 64] However, inward diffusion of dopants, when facile, can lead to complete ion exchange.[65] Ion exchange has emerged as an alternative method for generation of new nanomaterials.

1.5. Magnetic properties of materials

Magnetism is an intrinsic property of all materials, arising from dipole magnetic fields of electrons and their interaction with each other. The presence or absence of unpaired electrons and their collective interactions determines the magnetic strength of a material. Magnetic susceptibility (χ) is the degree of magnetization (M) of a material in response to the applied magnetic field (H).[66] The magnetism can be classified into five groups: diamagnetism, ferromagnetism, paramagnetism, ferrimagnetism and antiferromagnetism. Previously mentioned magnetism types can be understood with respect to their magnetic moment alignment in the absence of external magnetic fields. Figure 1.4 shows the spin arrangements of magnetic structures and their corresponding magnetic susceptibilities.

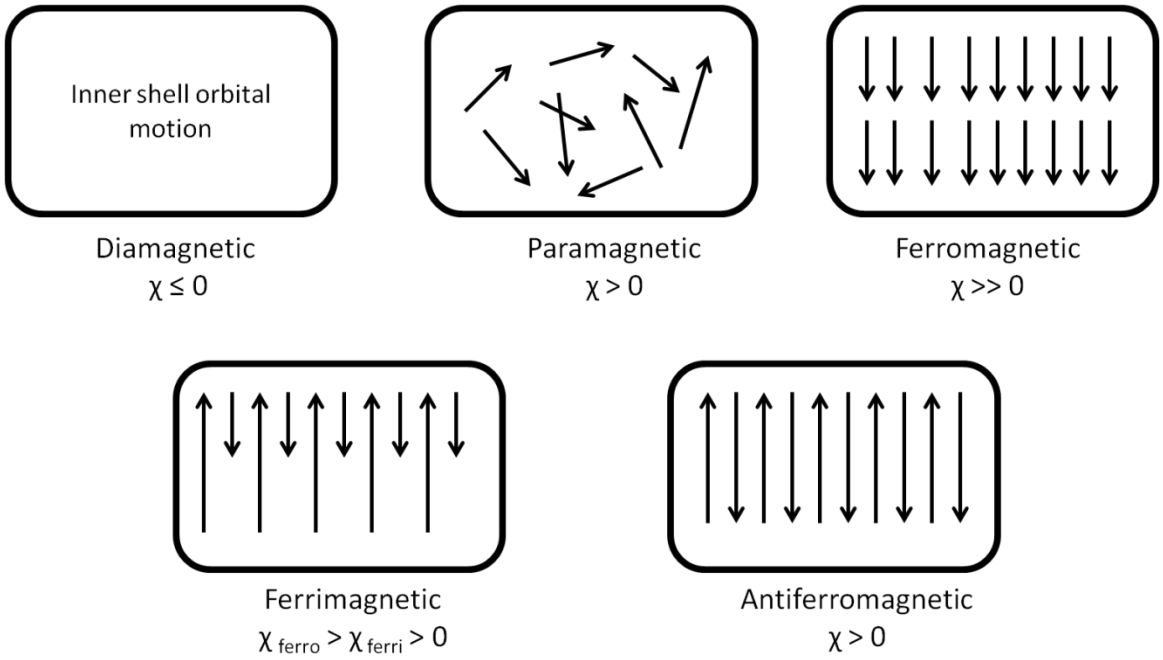

Figure 1.4 Schematic diagram of spin arrangements of magnetic structures and their corresponding magnetic susceptibilities (adapted from Myers).[66]

1.5.1 Diamagnetism

Diamagnetism is an intrinsic property of all materials (except H atoms) due to the presence of paired electrons. Materials categorized as diamagnetic contain only paired electrons. Compared to materials with unpaired electrons, the magnetic susceptibility of diamagnetic materials are either negligibly small (i.e. zero), or negative reflecting the weak expulsion of the magnetic field from the material.[66] The diamagnetic behavior is a result of the orbital motion of electrons and the magnetic susceptibility of diamagnetic materials is independent of temperature. The response of a diamagnetic material to applied magnetic field and temperature is shown in Figure 1.5.

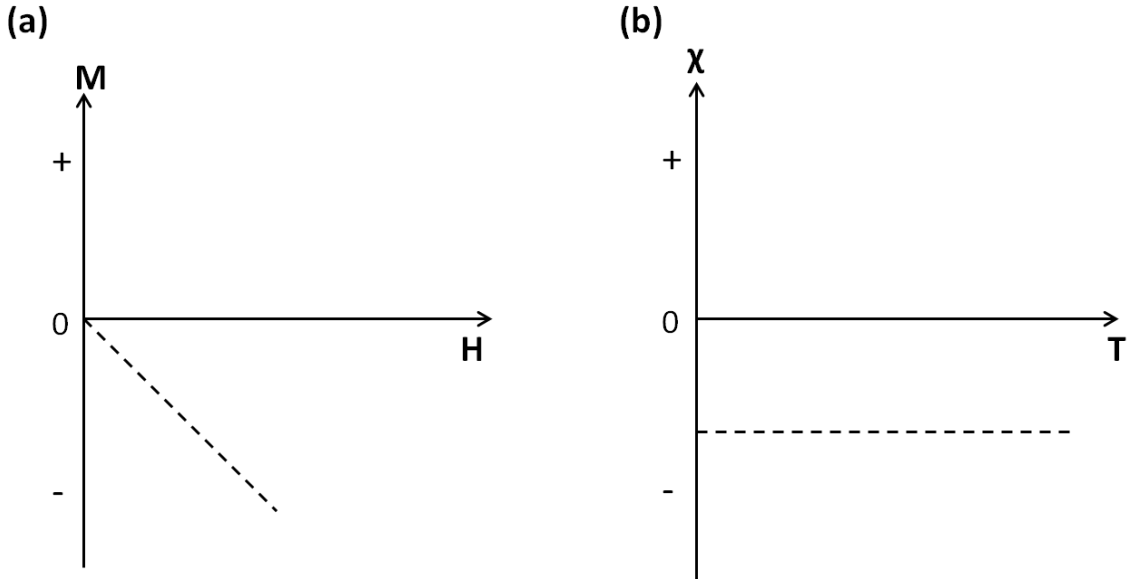

Figure 1.5 Typical (a) M vs H and (b) χ vs T curves of a diamagnetic material

1.5.2 Paramagnetism

In paramagnetic materials, spins are randomly oriented. Similar to diamagnetic materials, the magnetic moments of paramagnetic materials do not interact in the absence of an external magnetic field. When an external magnetic field is provided, the magnetic moments align in the direction of the field and result in a net positive magnetization and a small positive magnetic susceptibility. Thus, paramagnetic materials are attracted to a magnetic field in contrast to the repulsion observed in diamagnetic materials. As shown in Figure 1.6, the magnetization linearly increases with the applied magnetic field, reflecting the gradual orientation of the spins with the field. Unlike ferromagnetic materials, paramagnetic materials do not retain magnetization upon removal of the applied magnetic field. Instead, the magnetization returns to zero. The magnetic susceptibility is temperature dependant and it decreases with increasing temperature as thermal energy enables spins to overcome the orienting force of the external field

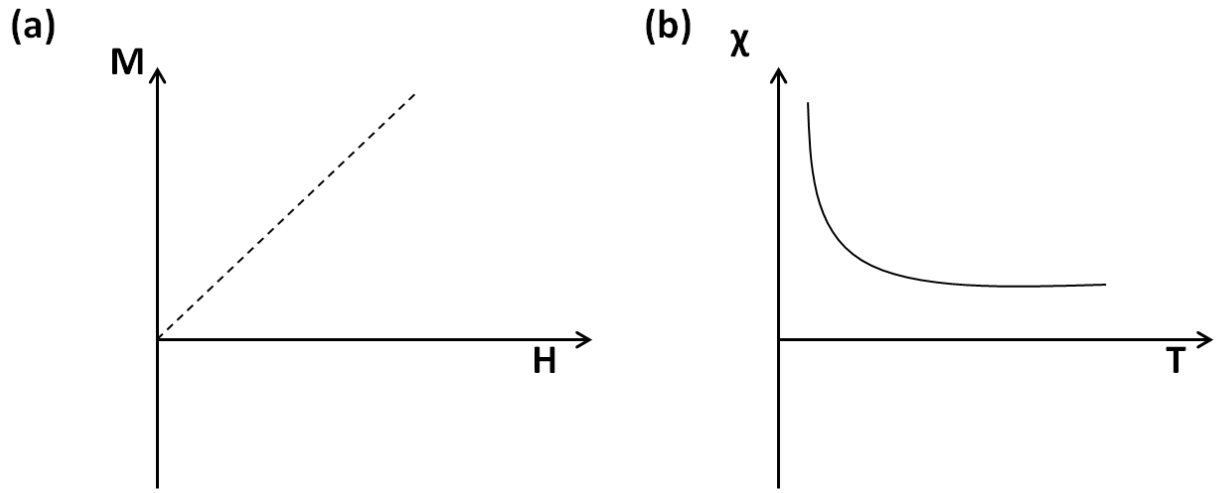

Figure 1.6 Typical (a) applied field and (b) temperature dependant magnetic properties of a paramagnet

1.5.3 Ferromagnetism

Ferromagnetism is the strongest type of response and a large and positive magnetic susceptibility is a characteristic of ferromagnetic materials. When an external magnetic field is applied, magnetic moments on a ferromagnet align parallel to the applied field, similar to a paramagnetic response, but strong forces between magnetic moments lead to saturation, and a large net positive magnetization, that may be retained upon removal of the magnetic field. As shown in Figure 1.7, as the applied field strength increases, the magnetization of a ferromagnetic material increases until it reaches a point where further increase of field does not affect the magnetization. This is the saturation magnetization, M_S; the maximum magnetization the material could reach. As previously mentioned in Section 1.5.2, paramagnetic materials reach zero magnetization upon removal of external magnetic field. However, in ferromagnets, when the applied magnetic field is removed, the electrons may remain in the parallel orientation and retain a residual magnetic moment, the remnant magnetization (M_R). In order to bring the total magnetization to zero, a magnetic field has to be applied in the opposing direction and this is

called the coercive field (H_C). As the magnetic field in the opposite direction increases, the material reaches a point where it becomes magnetically saturated in the opposite direction. Upon removal of the magnetic field, the material again shows a residual magnetization. However, this residual magnetization will be in the opposite (negative) direction of the previously observed M_R. As the applied field strength is increased again in the positive direction, the material reaches its saturation magnetization creating a hysteresis loop. Hysteresis refers to the lack of re-traceability of a physical property with respect to the effect that initiates it. The parallel orientation of magnetic moments assumed upon application of an external magnetic field can be disturbed by application of thermal energy. Thus the ferromagnetic material can transform into a paramagnetic material when the thermal energy is larger than the energy of spin alignment. The temperature at which the ferromagnetic to paramagnetic transition occurs is called the Curie temperature (T_C).

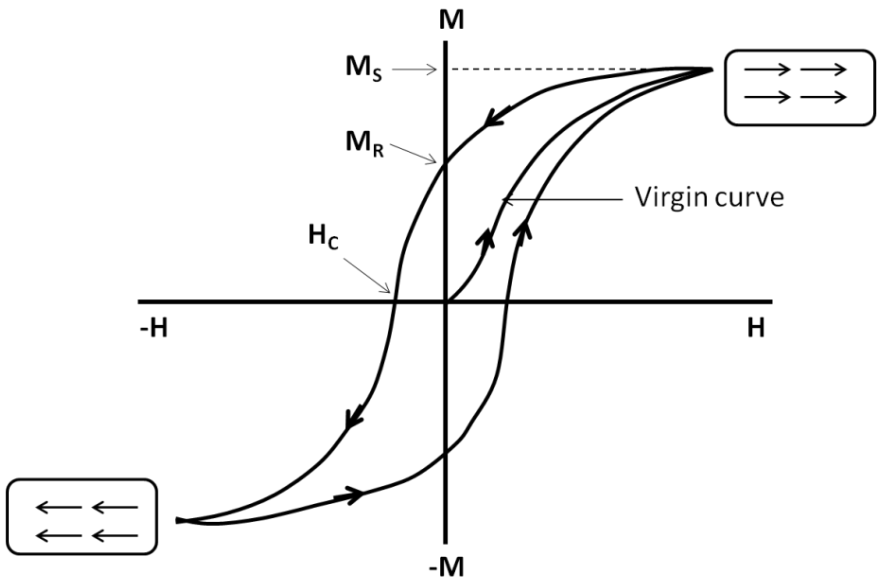

Figure 1.7 Schematic representation of magnetization vs. applied field of ferromagnetic material

1.5.4 Antiferromagnetism

In antiferromagnetic materials, the neighboring magnetic moments are equal but oriented opposite to each other. Similar to paramagnets, antiferromagnetic materials do not show magnetic interaction in the absence of an external field. However, upon application of an external field, these materials show a small positive magnetic susceptibility that increases linearly with increasing field and temperature. Antiferromagnetic materials become paramagnetic above a certain temperature, the Néel temperature (T_N). Above T_N, the magnetic susceptibility decreases with increasing temperature, just like a paramagnet. Typical magnetic properties of an antiferromagnetic material are depicted in Figure 1.8.

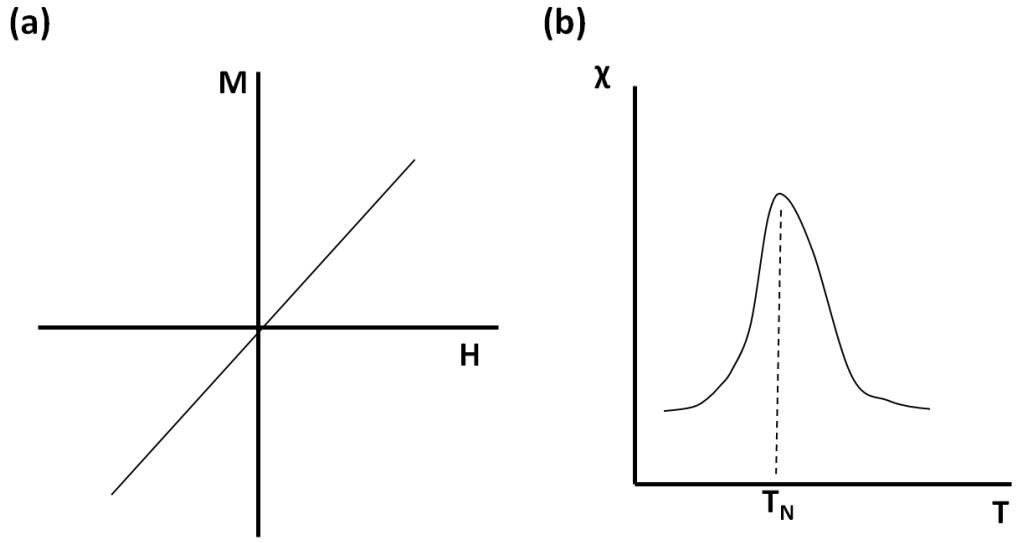

Figure 1.8 Typical (a) magnetization vs applied field and (b) magnetic susceptibility vs temperature plots for an antiferromagnetic material

1.5.5 Ferrimagnetism

In ferrimagnetic materials, the neighboring magnetic moments are oriented opposite, similar to antiferromagnets. However, the magnetic moments have different magnitudes resulting in a net positive magnetic susceptibility. Ferrimagnets exhibit the characteristic behavior of

ferromagnetic materials (Curie temperature, hysteresis, spontaneous magnetization) but the net moment is reduced. Magnetite (Fe_3O_4) is a well known example of a ferrimagnetic material in which half of the octahedral sites are occupied by Fe^{2+}. Remaining octahedral sites and the tetrahedral sites are occupied by Fe^{3+} and their spins are oriented in opposing directions.

1.6. Ferromagnetism and ferrimagnetism in nanomaterials

As the size of ferromagnetic materials is reduced down to the nano scale, they exhibit size-dependant properties. Thus, composition or phase-dependant properties in a bulk material can become size or shape-dependant on the nano scale.[67] The unusual properties exhibited by nano scale materials makes them suitable for applications in data storage, and in biomedical applications such as hyperthermia-based cancer treatment and magnetic resonance imaging (acting as contrast agents).[68]

In ferro and ferrimagnetic materials, upon cooling below a critical temperature, the magnetization spontaneously divides into magnetic domains, small regions in which magnetization is in a uniform direction (Figure 1.9). The transitions between different magnetic domains, domain walls, separate the magnetic domains and they represents a gradual reorientation of individual moments across a finite distance, generally around 100-150 atoms. In bulk magnetic materials, domain wall migration occurs in response to an applied magnetic field and this is the mechanism by which the overall magnetization reverses when the applied field is reversed.

Upon reduction of the size of a magnetic material to the nanoscale and reaching a size comparable to that of the intrinsic magnetic domain, the material behaves similar to a single magnetic domain as the formation of a domain wall is not thermodynamically favorable. Under the influence of temperature, the magnetization of reasonably small nanoparticles can randomly

flip. The reorientation process occurs through the coherent rotation of all the spins in the domain. This is a higher energy process than domain wall migration, hence, the coercivity is increased Figure 1.9). Further reduction of size leads to spin fluctuations in response to thermal energy, thus, the material becomes superparamagnetic. In superparamagnetic materials, hysteresis is no longer experienced and the material behaves similar to a paramagnet (zero M_R) in the absence of an external field. However, they show high M_S, similar to ferromagnetic materials.

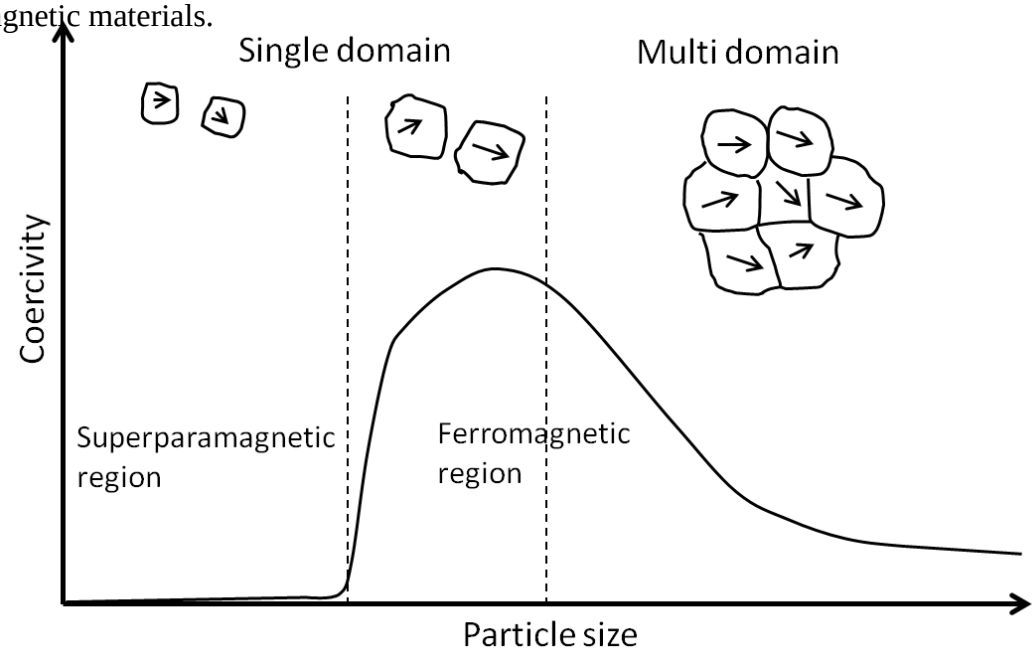

Figure 1.9 Schematic representation of coercivity vs particle size for a ferromagnetic material (adapted from Jun Young-Wook[67])

Magnetization vs. temperature graph representing field-cooled (FC) and zero-field cooled (ZFC) of a typical ferromagnetic nano material is shown in Figure 1.10. The temperature at which a ferromagnetic material transform in to a superparamagnetic material is called the blocking temperature (T_B) and this can be acquired from the ZFC curve. During the ZFC measurements, the sample is cooled in the absence of an external field, thus the moments are locked in their random orientations at lower temperatures. Upon heating, sufficient thermal

energy is provided to overcome the energy barrier and the moments begin to align in one direction. When the temperature reaches the blocking temperature, an increase of the magnetization is observed. Theoretically, the mentioned increase in magnetization is abrupt and continuous. However, for a sample of nanoparticles with a size distribution, a broad maximum can be expected as T_B is a sensitive function of particle size. As the temperature is increased further, the thermal energy causes the random orientations to dominate, thus a decrease of magnetization is observed. Under FC conditions, upon cooling, the moments are locked along the direction of external magnetic field, thus saturation is observed at lower temperatures. The FC curve shows a gradual decrease with increasing temperature and the FC and ZFC curves coincide at higher temperatures. When samples have low polydispersity, the T_B is identical to the temperature where the ZFC and FC curves meet.

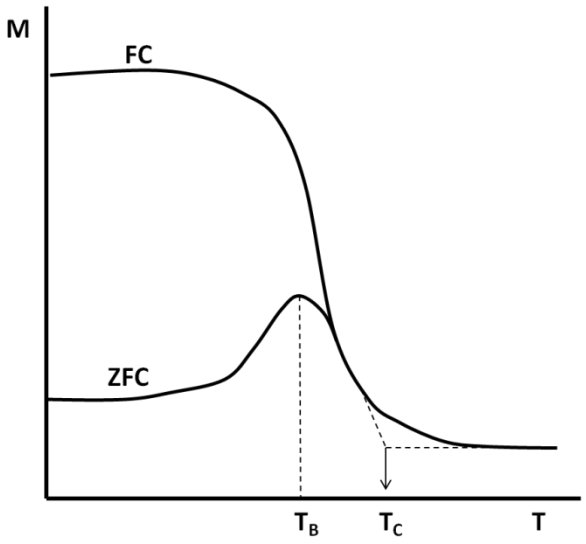

Figure 1.10 FC and ZFC curve for a ferromagnetic nano material

1.7. The magnetocaloric effect (MCE) and magnetic refrigeration

The magnetocaloric effect is an intrinsic property of all magnetic materials where a reversible isothermal magnetic entropy change (ΔS_M) or an adiabatic temperature change (ΔT_{ad}) change occurs in response to changes in an applied magnetic field. Since its discovery in 1881 by

Warburg, MCE has been employed in attaining ultra-low temperatures (≤1 K).[69,70] Typically, large values for MCE are observed when it is associated with a first order phase transition (FOPT) as an abrupt change in entropy is observed at the FOPT. The MCE associated with FOPT arise from the combination of changes in the magnetic and the lattice system, whereas second order phase transitions (SOPT) have only magnetic contributions, making the changes of MCE associated with SOPT smaller.[71] The magnetic refrigeration, an alternative to vapor cycle refrigeration, is based on MCE and has the advantage of achieving temperatures unreachable with gas compression cooling systems. Magnetic refrigeration cycle can be explained by coupling of magnetic system with lattice (Figure 1.11).

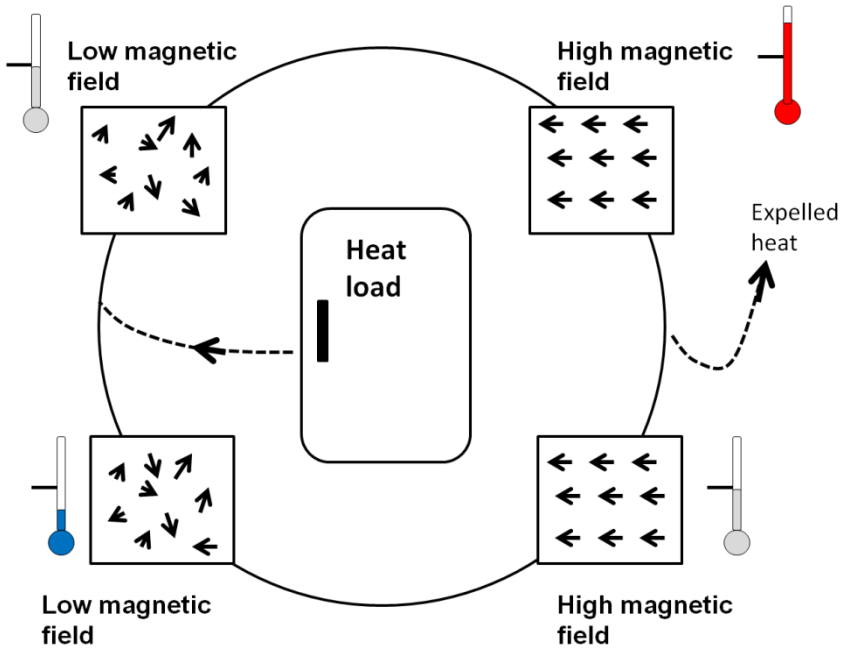

Figure 1.11 Schematic representation of a magnetic refrigeration cycle

Upon application of an external magnetic field, the magnetic moments of the magnetocaloric material (MCM) align parallel to the field, decreasing the entropy associated with the magnetic system. Under adiabatic conditions, the entropy of the lattice increases in order to compensate the decreased magnetic entropy. As the entropy of the lattice increases, heat

is generated through the vibration of the lattice. A heat transfer fluid is introduced to remove the heat and cool down the MCM. Upon demagnetization under adiabatic conditions, the magnetic moments randomize, increasing the magnetic entropy. Thus, the lattice entropy decreases, causing MCM to absorb heat from the surrounding. In the majority of the MCM materials reported, the FOPT is accompanied by considerable magnetic and/or thermal hysteresis, resulting in an energy loss in each cycle.[13, 72] Additionally, most of the reported MCM exhibit large MCE only upon application of high magnetic fields (≥ 2 T). Thus, research continues seeking MCM with large a MCE under low magnetic fields (≤ 2 T) and negligible hysteresis.

1.8. Magnetic and structural properties of MnAs

Among transition metal arsenides, MnAs in its bulk phase has received much attention due to its potential application in clean energy and data storage devices.[20, 73] In the field of magnetic refrigeration, bulk MnAs has been extensively studied due to its large MCE. As described in Section 1.7, magnetic refrigeration is based on the MCE, large energy changes that occur accompanying some ferromagnetic transitions.[20,73] Traditional magnetic refrigeration materials are based on Gd, and therefore cost-prohibitive, resulting in an exploration of more earth-abundant and inexpensive materials.[74, 75] Compounds containing manganese are a good alternative, as it is a transition metal of low cost and high abundance. MnAs has become a promising material for room temperature magnetic refrigeration applications due to the large magnetic entropy change, ΔS_M = -30 J kg^{-1} K^{-1} (field change, ΔH = 5 T) associated with the first-order phase transition at 315 K.[12, 76]

MnAs adopts two crystal structures: the hexagonal NiAs-type (α-type) and the orthorhombic MnP-type (β-type). α-MnAs is ferromagnetic while β-MnAs is paramagnetic. As shown in Figure 1.12, upon warming, bulk MnAs undergoes a FOPT at 315 K from a high-spin

ferromagnetic to a low-spin paramagnetic state with a structural transition from the hexagonal α phase (NiAs-type) to the orthorhombic β phase (MnP-type). A second-order phase transition takes place around 400 K, where the β phase transforms to the α phase while remaining paramagnetic.[51, 77]

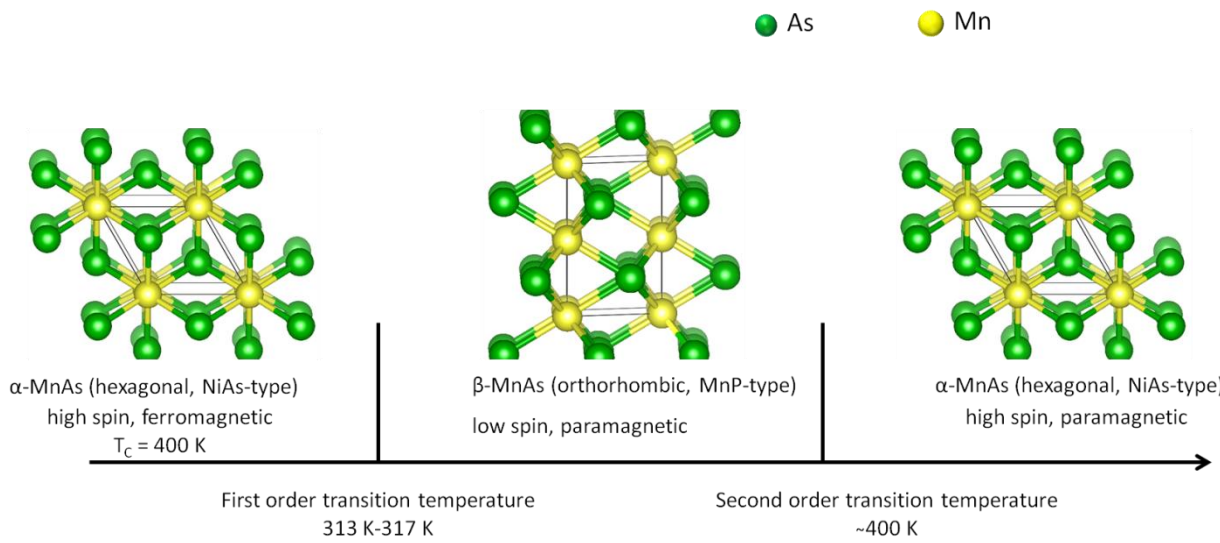

Figure 1.12 Magneto-structural phase transition in bulk MnAs (adapted from reference [78])

The first-order phase transition temperature has been found to be a sensitive function of Mn-Mn and Mn-As bond distances. Goodenough and co-workers demonstrated that increasing external pressure could lower the phase transition temperature, whereas reduced pressure could increase the transition temperature. The changes in transition temperature are due to the lattice compression or expansion due to external pressure.[79] The critical bond distances can also be affected by internal chemical pressure (i.e. doping), thus tuning the phase transition temperature is feasible.[80] Tuning of phase transition temperature expands the temperature range at which maximum MCE can be attained. Studies on bulk MnAs[77] have shown strong correlation between structure and magnetism as structural transition in MnAs can be driven by an applied magnetic field.[12] It is this magnetostructural coupling that yields the large MCE at FOPT.

Most reports on MnAs nanostructures are of disks or films, with few on actual nanoparticles, and all are on MnAs nanostructures epitaxially grown on InAs or GaAs substrates. Ploog and co-workers studied magnetic relaxation of α MnAs nanodisks of 100 nm diameter fabricated on a GaAs substrate by MBE. They report that the uniaxial magnetocrystalline anisotropy is large enough to stabilize the magnetization at room temperature. Thus, decay of magnetization is slow even at 27 ^{o}C, 10 ^{o}C below T_C.[81] Ramlan and co-workers reported fabrication of MnAs quantum dots on InAs nanowires by a chemical vapor deposition technique. They show that the self-assembled ferromagnetic quantum dots act as magnetic nanobits that could provide the basis for nanowire spin-valves.[82]

MnAs has been extensively studied as a potential candidate for magnetic refrigeration due to near room temperature T_C in addition to a large magnetocaloric effect. However, MnAs suffers from thermal hysteresis (*ca.* 10 K) that precludes efficient cycling, and the sharpness of the transition limits the temperature range for operation.[76] Nanostructuring can reduce the thermal hysteresis and doping is an effective method to tune phase transition temperature. Sun and co-workers have observed that doping Cr 0.6%-1% resulting in a giant magneto-caloric effect near room temperature and reduction of phase transition temperature to 265 K. In addition they report reduction of the thermal hysteresis.[83] In another study, the first-order phase transition was observed to be retained with up to 3% doping of P for As, shifting the transition temperature from 315 down to 280 K, but producing a temperature hysteresis of up to 30 K.[84] A reduction of the temperature hysteresis of polycrystalline MnAs has been reported and the strain and/or size were considered as the leading factors in tuning the intrinsic properties.[31] However, the inability to independently control size and strain combined with the polydispersity of the samples restricts evaluation of how those factors function in controlling the phase transition temperature and

temperature hysteresis. In the case of nanostructures grown on substrates, MnAs experiences external pressure from the substrate due to lattice strain, hence, probing intrinsic properties is challenging.

1.9. Discrete MnAs nanoparticles

Solution-phase routes have the potential to achieve size and composition control and yield narrowly polydisperse samples. Our group, for the first time, synthesized MnAs as discrete nanoparticles using SPAP by reacting dimanganesedecacarbonyl with triphenylarsine oxide in coordinating solvents at temperatures ranging from 523-603 K. Depending on the final temperature and the temperature at which precursors are introduced, either the α or β phase can be isolated at room temperature. Type-A MnAs nanoparticles (adopting the α structure at room temperature) has been synthesized by a slow heating method where the final reaction temperature is 523 K and type-B MnAs nanoparticle (adopting β structure at room temperature) has been prepared by a rapid injection method where final reaction temperature is 603 K.[14]

Similar to bulk MnAs, type-A MnAs nanoparticles were found to exhibit a magnetostructural phase transition at 312 K.[78] Bulk MnAs is paramagnetic at and above 315 K when it adopts the β structure. Type-B MnAs nanoparticles were found to be doped with phosphorus and as a consequence, the unit cell volume has compressed and the phase transition temperature has shifted below room temperature. Thus, the β-structure is observed at room temperature. A distinct reduction of T_C and magnetization has been observed as the particle size of type-B MnAs nanoparticles decreases. Notably, both A and B-type MnAs show significant reduction of thermal hysteresis compared to bulk MnAs,[63] suggesting that nanostructuring may reduce the thermal hysteresis while doping preserves the ability to tune the transition temperature. However, this synthetic method does not enable independent variation of size and

dopant concentration, thus the relative roles of these parameters on the magnetostructural phase transition remain unknown.

1.10. Thesis Statement

Arsenides are an important group of materials due to their composition and phase dependent properties such as magnetism (MnAs,[79] $Mn_{(1-x)}Fe_xAs$[85]), semiconductivity (InAs,[12] GaAs[86]) and superconductivity (LiFeAs, NaFeAs,[87] $BaFe_2As_2$[88]). Among arsenide phases, MnAs has been extensively studied because of its interesting magnetic properties and potential applications in data storage/processing and magnetic refrigeration.[13] While MnAs is a promising candidate for magnetic refrigeration, its cycling efficiency is adversely affected by high thermal hysteresis, potentially mitigated by nano-structuring.[76] As mentioned in Section 1.8, the temperature of the FOPT depends on the bond distances between Mn-Mn and Mn-As, and can be tuned by internal chemical pressure. Doping is an effective method to impose internal chemical pressure. Nanostructuring combined with cation and anion doping of MnAs can be used to tune the degree of hysteresis and phase transition temperature, thereby enabling the properties to be refined for magnetic refrigeration applications.

The binary MnAs system has received substantial attention based on its magnetic properties. However, ternary and quaternary phases can offer improved, perhaps unforeseen, properties as the complexity of the material increases. Nanoscale materials of these MnAs derivatives can provide decreased bit size in data storage and increased cycling rate in magnetic refrigeration. Nanostructuring of MnAs derivatives has been shown to shift the phase-transition temperature and impact hysteresis, but these studies were performed either on polydisperse samples or nanoparticles fabricated on a substrate imposing epitaxial strain. In order to understand the

consequence of size reduction on properties, synthetic methods that enable independent control of size/strain and composition on the nanoscale are needed.

Overall, this dissertation research is focused on understanding the growth mechanism and mechanism of P incorporation in MnAs nanoparticles and probing the effect of particle size and doping on magnetic and structural properties of MnAs nanoparticles. The dissertation study has three main objectives.

(1) The first objective of this dissertation is focused on quantitatively assessing the solution-phase MnAs nanoparticle formation mechanism and incorporation of P. This is achieved by monitoring the reaction by withdrawing aliquots at different reaction intervals. Transmission electron microscopy (TEM) is employed to monitor evolution of the morphology of the nanoparticles with respect to reaction time, whereas inductively coupled plasma-mass spectrometry is used to evaluate consumption of "monomers" with respect to the reaction time and the incorporation of P. Overall, this study establishes a reproducible synthetic method enabling fine control of size and composition for type-B MnAs nanoparticles, with a high degree of size uniformity. The results of this objective are discussed in Chapter 3.

(2) It has been previously reported that the temperature hysteresis in pure MnAs can be reduced in nanostructures prepared by ball-milling, with particle size and/or strain functioning as the major factor governing intrinsic properties.[31, 89] However, meaningful assessment of intrinsic properties such as phase transition temperature and thermal hysteresis is challenging with the polydispersity of the samples and the inability to independently control size and strain. Likewise, the previously reported SPAP method for synthesis of discrete MnAs nanoparticles[14] does not enable independent variation of size

and dopant concentration, thus the relative roles of these parameters on the magnetostructural phase transition are unknown. Accordingly, the second objective of this dissertation is to extend the knowledge obtained from the detailed synthetic mechanism and adventitious P doping in objective 1, to independently control nanoparticle size and P incorporation. Nanoparticles incorporating different P amounts with similar particle sizes (*ca.* 8 nm) are synthesized to probe the effect of doping on the magnetic and structural transitions. In order to probe the effect of size for constant P concentrations, nanoparticles of two different sizes (*ca.* 5 and 8 nm) with similar % P are prepared. Temperature dependant powder X-ray diffraction (PXRD) and temperature dependant magnetization data are acquired to probe the effect of particle size and dopant concentration on structural and magnetic transitions. The consequence of particle size and %P on magnetostructural properties are described in Chapter 4.

(3) As an alternate approach to P-doping, changing the internal chemical pressure of MnAs by doping with Fe is also expected to allow tuning of the transition temperature and hysteresis and leading to materials suitable for use in magnetic refrigeration. $Mn_{1-x}Fe_xAs$ and $Mn_{2-x}Fe_xAs$ are promising materials for magnetic refrigeration that have been studied in bulk.[85] However, the properties of the nano counterparts remain un-probed. The third objective of this dissertation research is to investigate the conditions for Fe doping in discrete MnAs nanoparticles and to elucidate the mechanism of Mn displacement in MnAs by Fe. The lowest time/temperature at which ion exchange can occur is assessed. The consequences of Fe doping on magnetic and structural transitions are probed by temperature dependant PXRD and magnetization studies. The findings of this study are described in Chapter 5.

CHAPTER 2 EXPERIMENTAL METHODS

This chapter discusses the materials and synthetic procedures, and the concepts and the working principles of the instruments employed for characterization of MnAs nanoparticles. The doped MnAs nanoparticles described in this dissertation study have been synthesized under inert conditions employing inert atmosphere glove boxes and Schlenk lines. The synthesized materials were characterized using the instruments in the Lumigen Instrument Center, and instrumentation available in the labs of collaborators. The characterization techniques include transmission electron microscopy (TEM), powder X-ray diffraction (PXRD), energy dispersive spectroscopy (EDS), AC magnetometry, and inductively coupled plasma-mass spectrometry (ICP-MS).

2.1. Materials

Dimanganesedecacarbonyl (98%), iron carbonyl (99%), iron(III) acetylacetonate (97%), triphenylarsine oxide (97%), 1-octadecene (90%, tech grade), trioctylphosphine oxide (90%, tech grade) and trioctylphosphine (97%) were purchased from Sigma Aldrich Inc. TOPO was purified by distillation and recrystallization as described by Buhro and co-workers.[90] All other chemicals were used as received.

2.2. Synthesis of doped, discrete MnAs nanoparticle

Synthetic procedures for doped MnAs nanoparticles are described in detail in Chapters 3-5 along with their purification method. The precursors and solvents were handled under inert conditions in an inert-atmosphere glove box and on a Schlenk line.

2.2.1 Inert atmosphere glove box and Schlenk line technique

The inert atmosphere glove box is an instrument that provides an oxygen and moisture free environment for safe handling and storage of moisture and air sensitive materials. It includes three main parts: main chamber, antechamber and gloves. The main chamber is used for

handling/storage of materials and performing reactions and it is always under positive pressure to prevent air leaks from outside. The pressure inside the main chamber is controlled by a photohelic pressure gauge. The antechamber is connected to the side of the main chamber and it is equipped with vacuum and inert gas purge valves. The materials are moved in and out from the box through the antechamber, which prevents contamination of the main chamber with air during the transfer of materials. The gloves are attached to the main chamber. The continuous circulation of argon gas through a catalyst (usually copper) removes oxygen and molecular sieves eliminate moisture, thus the inert atmosphere inside the glove box is continuously maintained. The catalyst is periodically regenerated to remove oxygen, which is in the form of CuO. Regeneration of the catalyst is performed by heating the catalyst in a mixture of N_2 and H_2 gas. The reducing environment provided by H_2 converts CuO into water and copper. The water adsorbed by molecular sieves is removed by a heating and evacuation procedure. The inert atmosphere glove box used in this dissertation is Vacuum Atmosphere VAC-HE493 and it is equipped with two antechambers and a refrigerator.

In parallel to the inert atmosphere glove box, the Schlenk line is used for performing reactions under inert conditions. The Schlenk line is a glass set-up with two manifolds: one for gas and one for vacuum. It also contains several ports for attaching additional features. In order to prevent backflow of air, an oil bubbler is attached to each port. A cold trap, usually liquid nitrogen, is placed between the vacuum line and the pump to prevent contamination of the pump with volatile solvents and reactive byproducts. Once the sealed Schlenk flask containing the chemicals is attached to the Schlenk line, the flask can be subjected to vacuum and inert gas (usually argon) purging. The excess pressure developed inside the Schlenk flask is released through the bubbler. In this dissertation research, the air and/or moisture sensitive chemicals

were sealed in a Schlenk flask inside the glove box before attaching to the Schlenk line to perform the actual reaction.

2.3. Power X-ray diffraction (PXRD)

Powder X-ray diffraction is an analytical technique used for identification of the crystallographic phase of crystalline materials. When the wavelength of the incident radiation and the shortest inter-atomic distance of the crystal are in the same range, diffraction takes place. The diffraction pattern of a material is similar to a "fingerprint" as it is unique for the material.[91] As shown in Figure 2.1, the X-rays are generated inside the X-ray tube by the collision of high energy electrons on a metal anode, usually Cu or Ni.

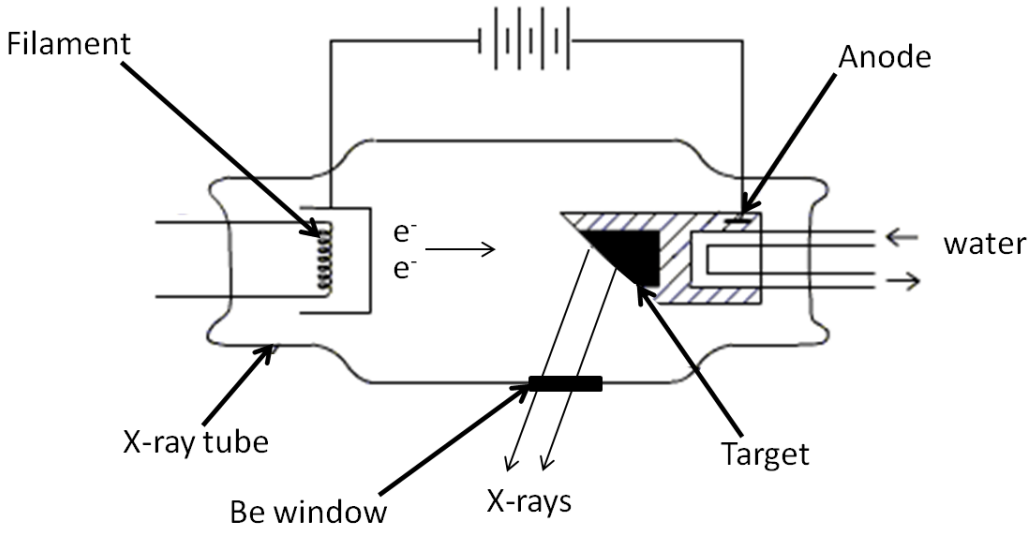

Figure 2.1 Schematic representation of an X-ray tube (adapted from Parkin[92])

The electrons are generated from a heated tungsten filament inside the X-ray tube. A large potential difference (40 kV for a Cu anode) is maintained between the cathode and the anode. The X-rays generated exit through a Be window, as Be has a small atomic number and absorbs a minimum amount of X-rays. The X-ray tube is maintained under vacuum to prevent

oxidation of the filament. Collision of high energy electrons on the anode generates heat, thus, the anode must be continually cooled through a chilled water circulation system. The X-ray spectra resulting upon collision of high energy electrons consist of two components: white radiation and monochromatic radiation (Figure 2.2).[93] Upon collision of the electron with the anode, some energy is lost, and a portion of the lost energy transforms into electromagnetic (white) radiation.

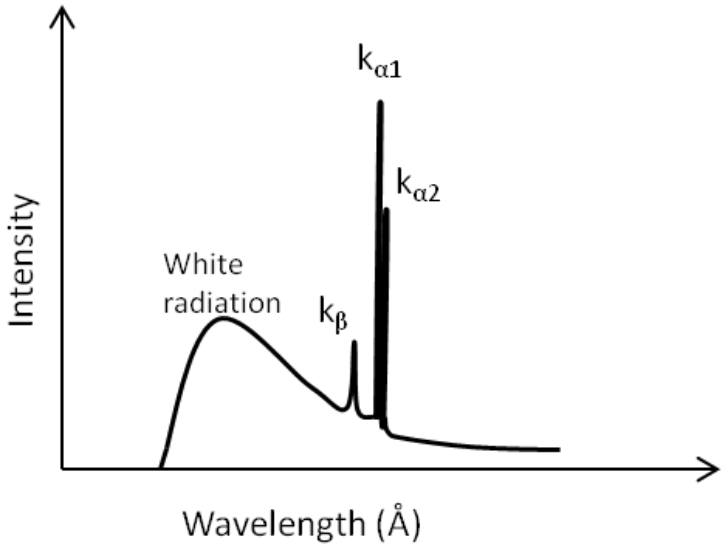

Figure 2.2 X-ray emission spectrum of Cu (adapted from Lesley[93])

The process of generation of X-rays shown in Figure 2.3. The accelerated electrons have adequate energy to ionize some of the Cu 1s electrons in the K shell. As a result, a vacancy is created and an electron from a 2p or 3p orbital falls into the vacant orbital. The energy released during the process generates X-rays. As shown in Figure 2.2, the X-ray spectrum is composed of white radiation, which is a broad hump, and monochromatic radiation with intense signals. The electron transition from the 2p orbital to the 1s is called K_{α} and its wavelength is 1.5418 Å for Cu. A transition from 3p to 1s generates K_{β} with a wavelength 1.3922 Å. The Cu K_{α} transition is

used in most experiments as it is the most intense peak due to the increased frequency of occurrence relative to K_β. However, K_α is a doublet with slightly different energies due to two possible spin states of the 2p electrons.

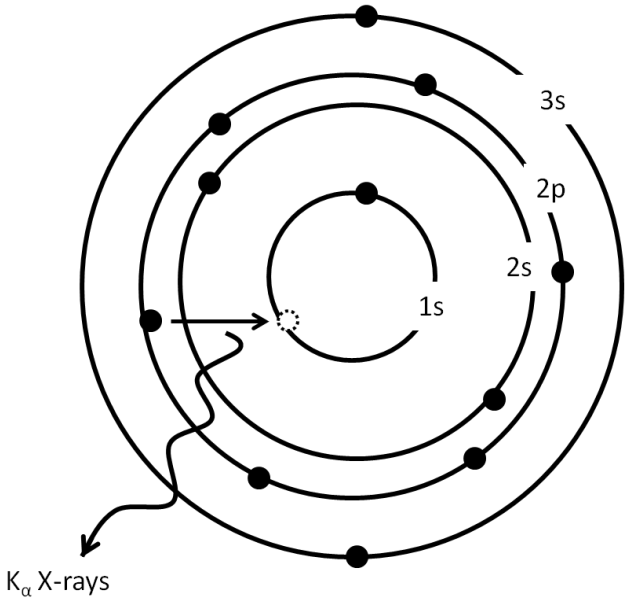

Figure 2.3 Schematic representation of generation of Cu Kα X-rays

The principles of diffraction can be explained by Braggs' law. In order to apply Braggs' law, it is assumed that the crystals are composed of semitransparent layers of atoms.[91] Upon hitting the atomic layers, a portion of the X-rays are considered to diffract as a mirror reflection of the incident beam, thus, the angle of incidence and reflection are the same. The rest of the X-rays are transmitted and diffracted by succeeding layers of atoms. Braggs' law can be derived by using the schematic representation shown in Figure 2.4.

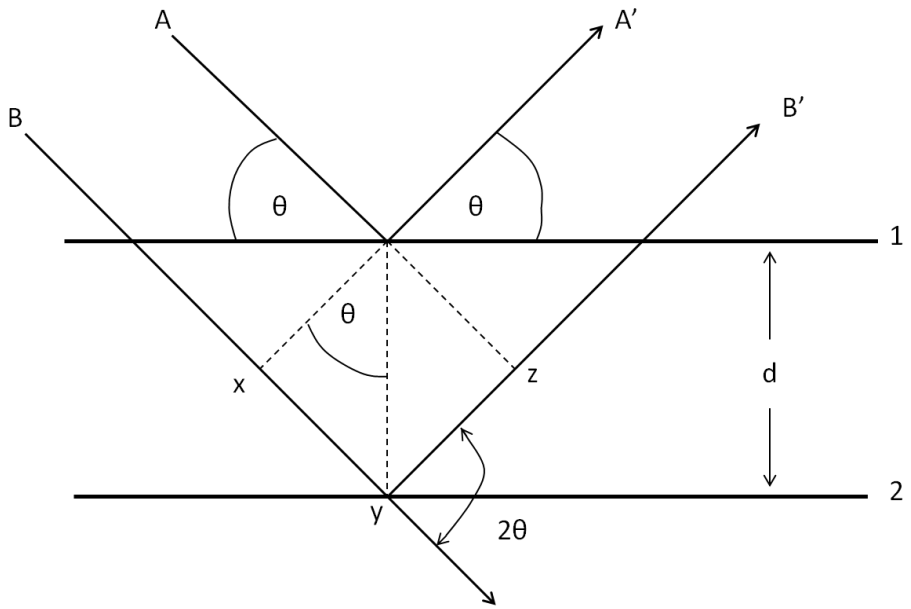

Figure 2.4 Schematic representation of X-ray diffraction from atomic planes (adapted from Cullity[91])

The X-ray beams, A and B reflect from the atomic planes 1 and 2, respectively. The beam BB' travels an additional distance compared to beam AA' and this extra distance is xyz. The incident angle is called the Bragg angle, θ. The d-spacing, d, is the perpendicular distance between the two adjacent atomic planes. In order to result in constructive interference, the beams A' and B' have to be in phase, thus the extra distance traveled (xyz) must be an integer of wavelength.[92] The relationship between the path difference, Bragg angle and the d-spacing can be given by

$$xy = yz = d \sin\theta \qquad \textbf{2.1}$$

Therefore,

$$xyz = 2d \sin\theta \qquad \textbf{2.2}$$

However,

$$xyz = n\lambda \quad \textbf{2.3}$$

Where n is an integer and λ is the X-ray wavelength

Therefore, Braggs' law can be given by

$$2d \sin\theta = n\lambda \quad \textbf{2.4}$$

Upon satisfying Braggs' law, the reflected beams interfere constructively resulting in peaks in the PXRD pattern. The size and shape of the unit cell determines the peak position while the peak intensity is determined by the electron density and the specific arrangement of atoms in space. Disruptive interference takes place when reflected beams are out of phase with incident beams, thus, the intensities cancel out.

The peaks in the PXRD pattern of a nanomaterial are usually broader compared to their crystalline bulk counterpart. Nanocrystals contain a fewer number of planes compared to the bulk material, hence, the beams undergo partial interference (are not completely cancelled out) and this results in broader peaks. In the bulk material, there are more planes than in a nanocrystal, thus, the reflected beams that do not satisfy Braggs' law are completely cancelled. Peak broadening of a nanocrystal is inversely proportional to the size of the nanocrystal and easily discernible for thickness. Hence, with the use of full width at half maximum of the peak (FWHM), the size of the nanoctystal can be calculated using Scherrer equation.[94]

$$D = 0.9\lambda / \beta \cos\theta \quad \textbf{2.5}$$

where, D is the average size of the nanocrystal; β is FWHM (in radians); θ is the Bragg angle and λ is the wavelength.

In this dissertation research, room temperature powder X-ray diffraction data were acquired in the range $2\theta = 20^{o}$-70^{o} on a Bruker phaser II model diffractometer equipped with a

Cu anode. Samples were placed on a zero-background plate for measurement. The diffractograms were collected at 40 kV. The temperature-dependant structural phase transition of doped MnAs nanoparticles was probed with a Bruker D8 Advance A 25 diffractometer. The sample was mounted on a TTK-450 variable temperature stage and data were acquired upon cooling and heating at 10-30 K intervals in the range $2\theta = 20^{o}$-70^{o}. The sample was allowed to equilibrate 20 minutes at each temperature before starting the scan. The lowest and highest temperatures were determined based on the nature of the sample and limits of the instrument (lowest possible temperature = 93 K). The crystallographic phase was identified by comparing the collected patterns to the Powder Diffraction File (PDF) database (release 2000) from the International Center for Diffraction Data (ICDD). Relative quantities of phases were calculated with DIFFRAC.TOPAS software.

2.4. Electron microscopy

Electron microscopy is an analytical technique that utilizes an electron beam for imaging. Since the wavelength of an electron is extremely short compared to visible light, electron microscopes provide higher magnification than optical microscopes, thus, analysis of ultra-small materials is possible. Compared to optical microscopes, electron microscopes facilitate analysis of elemental composition and crystallographic information in addition to morphology and particle size determination. Imaging and associated techniques are achieved by passing a beam of accelerated electrons through an ultra-thin specimen. Interaction of the electron beam with the specimen generates a variety of radiations that can be used for different applications. Figure 2.5 depicts the radiation type and corresponding applications.

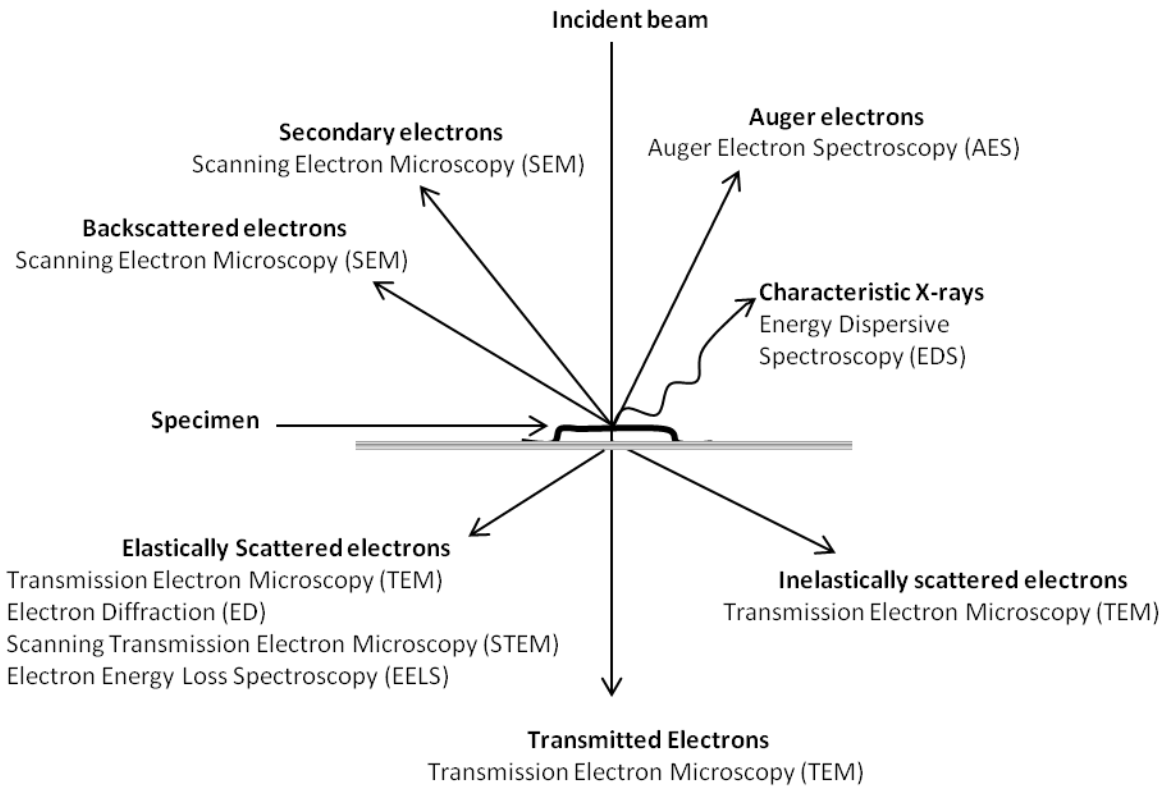

Figure 2.5 Processes occurring in a specimen after high energy electron bombardment

The electron microscopes are used in two basic modes; transmission and reflection mode. Transmission electron microscopy (TEM) uses unscattered electrons transmitted through the specimen. Scanning electron microscopy (SEM) uses the secondary electrons and backscattered electrons emitted from the specimen.[95] TEM, STEM and SEM instruments use the characteristic X-rays generated during electron bombardment for element composition analysis by energy dispersive spectroscopy (EDS). In this dissertation study, TEM was employed for investigation of morphology, particle size and size distribution while EDS and STEM were employed to acquire information on elemental composition and elemental distribution.

2.4.1 Transmission Electron Microscopy (TEM)

The transmission electron microscope is a versatile instrument for the acquisition of information on size and morphology of nanoparticles over a wide range of magnification. Due to the small de Broglie wavelength of electrons, TEM facilitates imaging at a notably high magnification compared to an optical microscope.[96] In addition to size and morphology analysis, TEM enables analysis of elemental composition and crystal structure. This imaging technique involves transmitting a beam of accelerated electrons through a thin specimen, where the electrons interact with the specimen. Figure 2.6 shows a schematic diagram of a TEM.

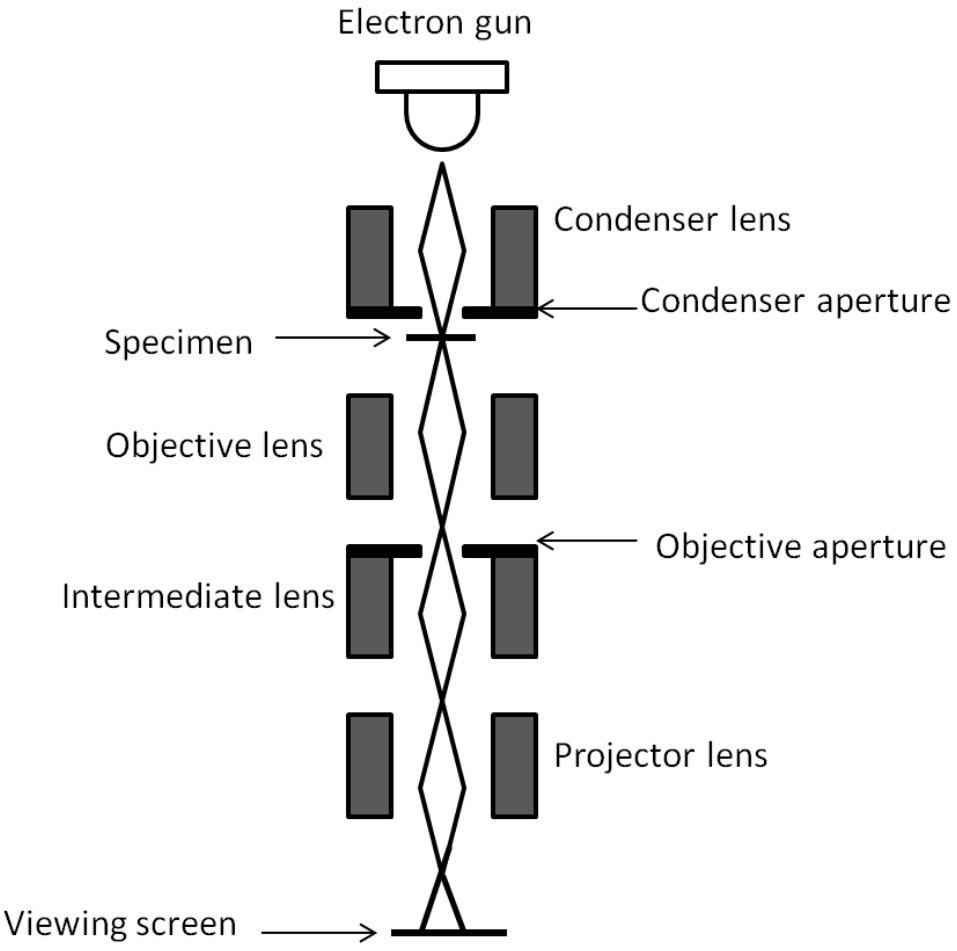

Figure 2.6 Schematic representation of a conventional TEM (adapted from Goodhew[97])

The high energy electron beam used in the TEM is generated by an electron gun; either a thermionic or a field emission gun. Thermionic guns contain either a tungsten (W) filament or lanthanum hexaboride (LaB_6) filament, which is heated to generate electrons. Field emission guns use a strong electronic field (~10^9 Vm^{-1}) on tungsten strips to produce electrons.[96] The thermionic sources have the disadvantage of gradual evaporation or oxidation of the filament and the electrons are less monochromatic. TEM instruments with field emission sources provide better resolution compared to the instruments with thermionic sources, as the radiation is more monochromatic, and are more durable since operation is performed at a lower temperature. The generated electrons are accelerated towards an anode maintained at a higher potential. Most TEM instruments operate at a high accelerating voltage (100-300 kV), which tunes the wave length of electrons. The relationship between the accelerating voltage (V) and the resulting wavelength (λ) is

$$\lambda = h / [2eVm_e + (e^2 V^2) / c^2]^{½} \qquad \textbf{2.6}$$

where h is Planck's constant, m_e is the mass of an electron, e is the charge of electron and c is the velocity of light. However, relativistic effects must be considered when calculating the wavelength of the electron, as the velocity of electrons approach half of that of the speed of light when the accelerating voltage is increased beyond 100 kV.[98] A condenser system composed of electromagnetic lenses focus the high energy electron beam on the specimen. The specimen is prepared as an ultra-thin film on a supporting grid and it is mounted on a side-entry double-tilt holder before inserting into the specimen chamber. The electrons that interacted with the specimen pass through the objective lenses to generate the first intermediate image and the diffraction pattern. The objective aperture can be employed in two basic modes; image mode and

diffraction mode. In the image mode, the direct beam is allowed to pass through the objective aperture and bright field images are generated (Figure 2.7 (a)). The diameter of the objective aperture governs the resolution of the final image. In the diffraction mode, scattered electrons are allowed to pass through while directly transmitted electrons are blocked, resulting in dark field images (Figure 2.7 (b)). The intermediate image produced by the objective lens is magnified by intermediate and projector lenses and the final image is projected on a fluorescent screen, which is captured by the camera system.

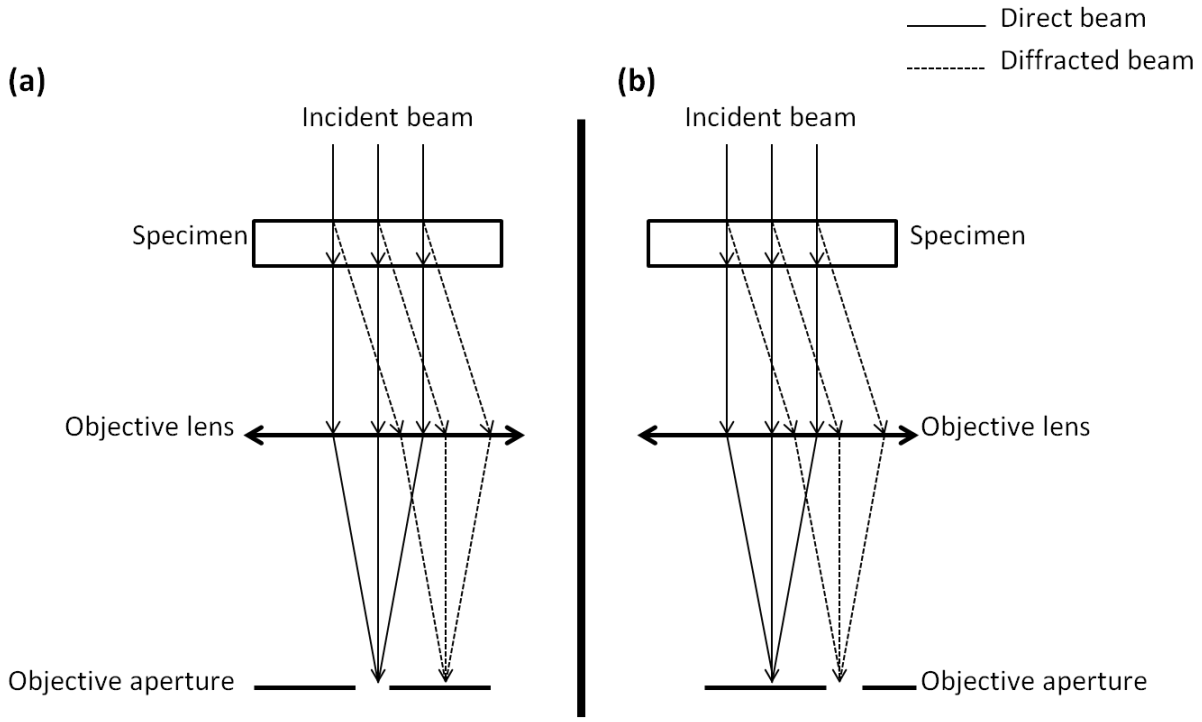

Figure 2.7 Ray diagrams showing modes of objective aperture. (a) bright field imaging mode (b) dark field imaging mode

In this dissertation study, a JEOL 2010 TEM was used in the bright field imaging mode at an accelerating voltage of 200kV. The specimen was prepared by dispersing a small amount of the sample in chloroform and placing a drop of the suspension on a copper grid coated with

carbon. Particle size distribution was calculated using TEM images with that exhibited separated particles and image size calculation software.

2.4.2 Energy Dispersive Spectroscopy (EDS)

Energy dispersive spectroscopy is an additional analytical technique facilitated by electron microscopes. As mentioned in Section 2.4, interaction of high energy electrons with matter results in a range of radiation types, and coupling appropriate detectors facilitates the capture of their radiation, enabling more information to be obtained. As shown in Figure 2.3, characteristic X-rays are emitted when high energy electrons collide with the material. Atoms of each element in the material produce their characteristic X-rays. In EDS, the emitted characteristic X-rays are used for qualitative and quantitative analysis of the elemental composition. Figure 2.8 depicts the transitions producing X-ray lines. The intensity of the signals is proportional to the quantity of the elements, thus, the elemental composition can be quantitatively assessed. The EDS detector crystals are either high purity germanium or silicon doped lithium.[97] Analysis of lighter elements with EDS is challenging as they produce low energy X-rays that are absorbed within the sample and the Be window of the detector. Variation of the chemical composition of the material can be analyzed with EDS in one-dimensional or two-dimensional scans. A one-dimensional scan over an area of interest results in a line scan across the selected area, while a two-dimensional scan provides an element map. In this dissertation research, an EDS detector (EDAX inc.) coupled to JEOL 2010 TEM was used for preliminary analysis of elemental composition.

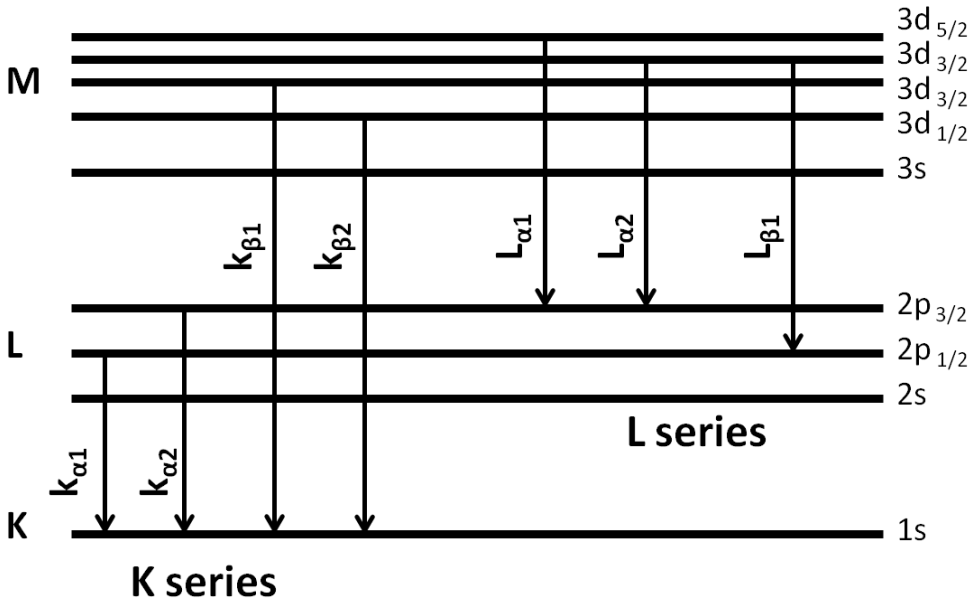

Figure 2.8 X-ray transitions that generate lines in an EDS spectrum

2.4.3 Scanning Transmission Electron Microscopy (STEM)

Scanning transmission electron microscopy is versatile tool which is a combination of SEM and TEM. In TEM, the area of interest is illuminated for imaging. However, in STEM, the electron beam scans the selected area. Figure 2.9 shows a simplified schematic diagram of an electron microscope dedicated for STEM analysis.

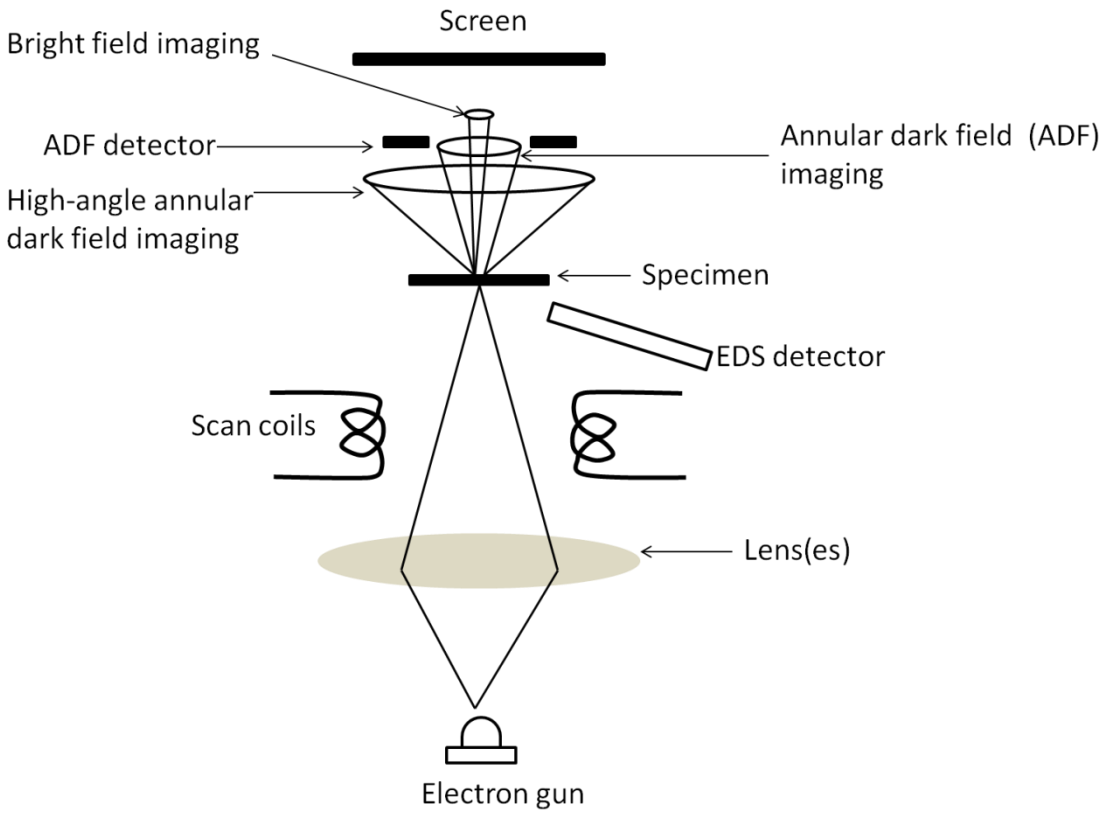

Figure 2.9 Schematic of a dedicated STEM (adapted from Goodhew[97])

Compared to TEM, the STEM instrument does not contain intermediate and projector lenses, hence, more space is available for different types of detectors. The electron beam is produced by a field emission gun and the bright field detector collects the undiffracted electrons to generate the bright field images. The annular dark field detector (ADF) captures the diffracted electrons to produce dark field images. The high-angle annular dark field (HAADF) detector collects the electrons scattered with higher angles. HAADF-STEM provides contrast imaging as the intensity of the electrons scattered to higher angles increases with increasing atomic number; thus, chemical identification of columns of atoms of is possible.

In this dissertation, HAADF images, elemental line profiles and elemental maps were acquired using an FEI Titan 80-300 high angle annular dark field-scanning transmission electron microscope (HAADF-STEM) with ChemiSTEM technology operated at 200 kV. The imaging,

elemental line scanning and mapping was performed by Yang Liu at the microscopy facility at North Carolina State University.

2.5. Inductively Coupled Plasma Mass Spectrometry (ICP-MS)

ICP-MS is an analytical technique with superior detection capabilities used for elemental analysis of bulk samples. ICP-MS has several advantages over other elemental analysis techniques such as distinguishing isotopes, a minimal matrix effect and higher detection limits. However, the components in the gases used and the impurities that arise in specimen preparation can greatly affect the accuracy and precision of the outcome. In the ICP-MS instrument, the high temperature ICP source is coupled with a mass spectrometer. The atoms of each element in the material are converted to ions by ICP. The ions are then separated by the mass spectrometer. Figure 2.10 depicts a schematic representation of an ICP torch.

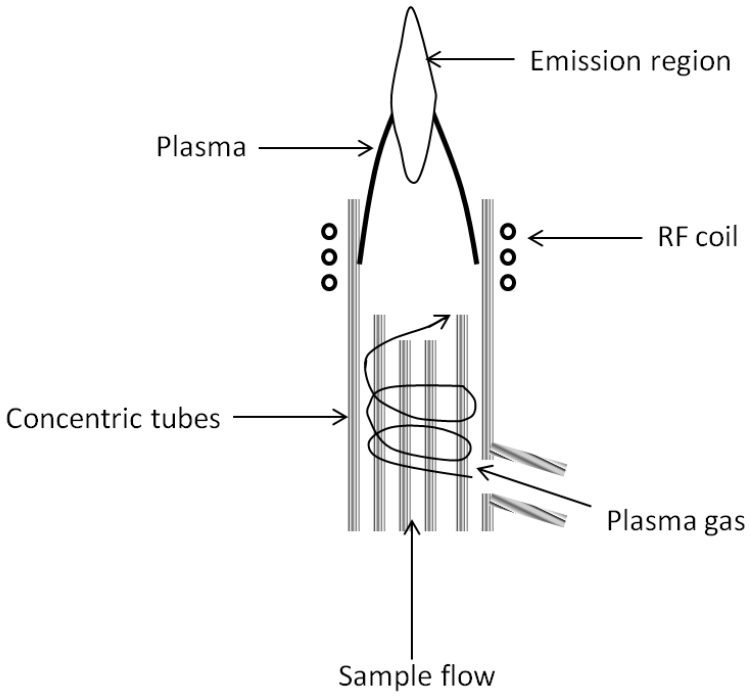

Figure 2.10 Schematic representation of ICP torch (adapted from Montaser[99])

The ICP torch consists of concentric tubes through which Ar gas flows. The tip of the concentric tube is wrapped with a radio-frequency (RF) coil. Oscillating electric and magnetic fields are generated at the tip of the tube as power is supplied to the RF coil. Upon providing an electric spark, the electrons are stripped from argon atoms resulting in ionization of argon. The argon ions interact with the oscillating fields to generate more ions and collision with other argon atoms produces an argon discharge plasma that produces a temperature of 6000-10,000 K. The samples and the standard solutions are introduced to the plasma in the form of an aerosol. Inside the plasma, the solvents immediately vaporize and the elements are converted to gaseous atoms before ionization takes place. The ionized species travel through interface cones to the mass spectrometer. The interface cones assist in directing the center portion of the ion beam in to the mass spectrometer.

Positively charged electrostatic lenses focus the ion beam in to the entrance slit of the mass spectrometer. Inside the mass spectrometer, the ions are separated according to their mass-to charge ratio (m/z). The most commonly used mass filter in mass spectrometers is the quadrupole mass filter (Figure 2.11). Application of alternating AC and DC voltages to opposite pairs of the rods results in an electrostatic filter that permits ions of single m/z ratio to pass through the rods at a given moment. This technique provides ICP-MS the ability to filter isotopes as the isotopes of the ions have different masses.

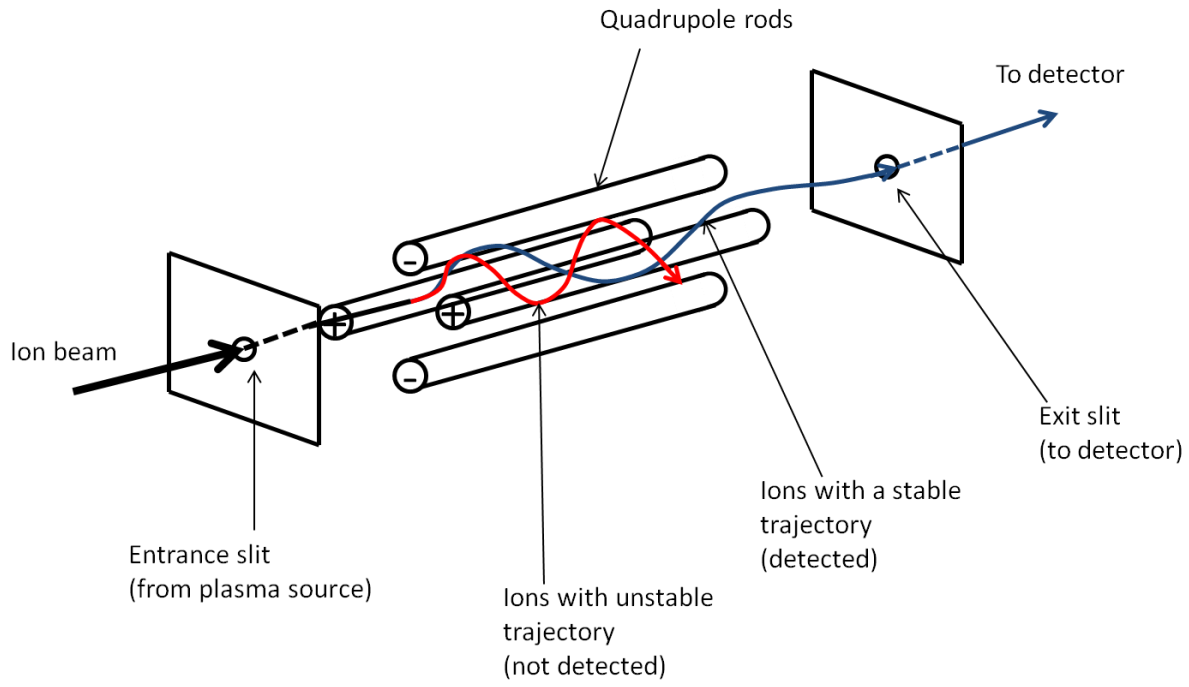

Figure 2.11 Schematic of quadrupole mass filter (adapted from Montaser[99])

The ions separated my their m/z ratio are then captured by the detector, which translates the number of ions striking into an electrical signal that is measured and compared to the number of atoms of each element in the sample by using calibration standards. The most commonly used detectors are of the discrete dynode type, as they have a wider linear range, thus possessing the ability to analyze a wide range of concentrations (sub parts per trillion-high parts per million).

In this dissertation research, an Agilent 7700 series ICP-MS instrument was used to determine the elemental composition of the doped MnAs nanoparticles. Solid powders of MnAs nanoparticles were dissolved in a minimum amount of concentrated nitric acid and then diluted as needed. A 2% HNO_3 solution was used as blank.

2.6. Magnetometry

Magnetic measurements are acquired by one of two basic methods: AC magnetic measurements and DC magnetic measurements. In AC magnetic measurements, time-dependent AC magnetic moments are formed in the sample as a response to a small AC driven magnetic field applied to the sample, while DC magnetic measurements determine the equilibrium value of the magnetization for the sample. AC measurements are capable of providing information on magnetization dynamics that are not accessible from DC magnetic measurements as the moment of the sample is constant during the DC measurement time.

The Superconducting Quantum Interference Device (SQUID) is the most effective and sensitive technique for measuring subtle magnetic properties. The SQUID has the sensitivity to measure magnetic fields as low as 5 aT (1 aT = 10^{-18} T). Josephson junction, a loop of superconducting material separated by thin insulating regions, is the main component of SQUID. The Josephson effect results in a weak superconductivity in the Josephson junction with respect to the rest of the superconductor loop.[100] The current flowing through the junction is much less than the current of the superconducting loop, thus a phase variation is generated. Upon application of a continuous voltage, the phase difference in the loop creates an alternating current that is highly sensitive to magnetic flux, thus, the Josephson effect provides a means to acquire magnetic measurements with high accuracy.

Figure 2.12 shows a cross section of a SQUID system along with a schematic representation of a superconductor loop showing the Josephson junctions. The input coils and SQUID are located inside a superconducting niobium shield that operates in a cryogenic environment created by liquid He (4.2 K), while the SQUID electronics systems are held at room temperature. In SQUID systems, the superconducting pick up coils that are sensitive to the

magnetic flux of the specimen are inductively coupled to the SQUID. A voltage across the superconducting loop is generated as a response to the changes in magnetic flux detected by the SQUID system, thus, the voltage reflects the magnetic moments in the specimen.[100]

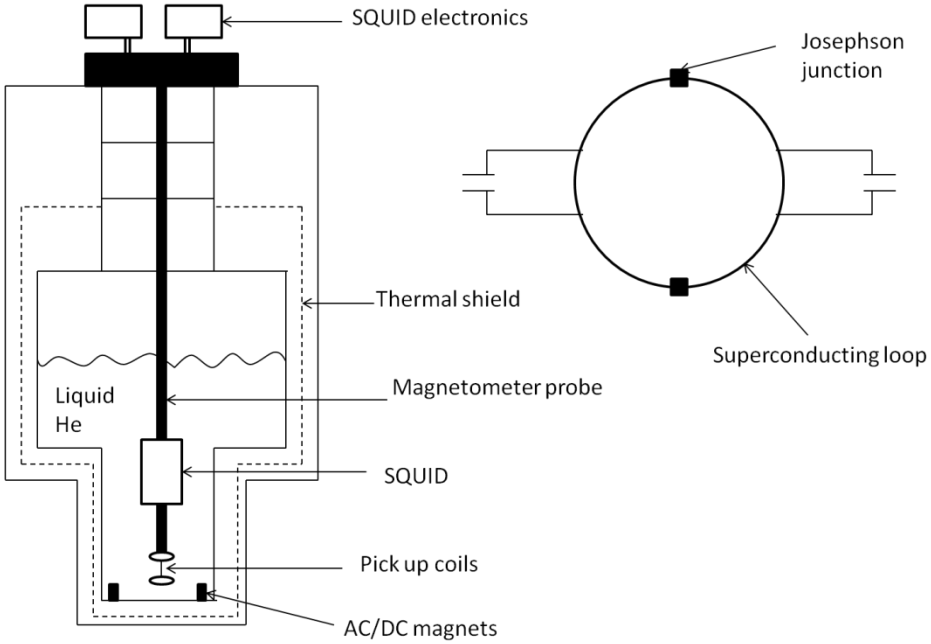

Figure 2.12 Schematic diagram of a DC SQUID magnetometer and superconducting coil with Josephson junctions. Adapted from reference [100]

In this dissertation research, the DC magnetic measurements were acquired using a Quantum Design MPMS-5S SQUID magnetometer and AC measurements were collected on a Quantum Design model 6000 Physical Property Measurement System (PPMS). A powder sample is placed inside a gel capsule and cotton wool specified for magnetic measurements was packed in order to keep the sample powder stationary. The gel capsule is fixed in a plastic straw before loading in to the magnetometer. The magnetic transition temperatures were identified by measuring DC-magnetization signals upon cooling and warming the sample under a magnetic field of 100 Oe. The temperature range includes the transition temperature estimated by temperature dependant PXRD. The field-cooled (FC) measurements were collected upon

warming the sample which was previously cooled under 100 Oe field. The Zero-field cooled measurements were collected upon warming the sample which has been cooled in the absence of an external magnetic field. The magnetic data were collected by Ehab Abdelhamid in Professor Boris Nadgorny's research group, Department of Physics and Astronomy, Wayne State University

CHAPTER 3 SOLUTION-PHASE GROWTH MECHANISM OF PHOSPHORUS-DOPED MnAs NANOPARTICLES: SIZE, POLYDISPERSITY AND DOPANT CONTROL ON THE NANOSCALE

3.1 Introduction

MnAs exhibits a large magnetocaloric effect associated with the first-order phase transition at 315 K, making it a promising phase for near-room-temperature magnetic refrigeration technologies. Optimization of the properties to expand the temperature range of operation (by adjusting the phase transition temperature) and reduce hysteresis losses can be achieved by doping and nanostructuring, respectively. However, MnAs suffers from thermal hysteresis (ca. 10 K) that precludes efficient cycling, and the sharpness of the transition limits the temperature range for operation.[76] Anion doping has been effective in tuning the phase transition temperature in bulk MnAs. The first-order phase transition was observed to retained with up to 3% doping of P for As, shifting the transition temperature from 315 down to 280 K, but producing a temperature hysteresis of up to 30 K.[84] Nanostructures prepared by ball-milling of pure MnAs have shown reduced temperature hysteresis, with particle size and/or strain implicated as the governing factor.[101] Most of the reports on MnAs nanostructures were focused on films[102,103] or disks[35,104] and the number of reports found on the synthetic of nanocrystals[77] or nanodots are limited. In all of these reported cases, syntheses methods were limited to growth of MnAs nanostructures by chemical vapor deposition (CVD) or physical methods such as molecular beam epitaxy (MBE). However, the polydispersity and the inability to independently control size and strain prevent assessment of how these factors influence the intrinsic properties of MnAs nanostructures, including the phase transition temperature and temperature hysteresis.

Solution-phase routes have the potential to achieve size and composition control and yield narrowly polydisperse samples. However, the ability to control size and composition can be

challenging if little is quantitatively known about the crystallization process of a given system. During the previously reported synthesis, when the precursors and reaction temperature are kept the same, the reaction time determines the particle size and final doping of P in the MnAs nanocrystals. As the reaction time increases, the particle size increases and concentration of P-dopant decreases. This may be explained by changes in the incorporation rate of P over time (e.g. enhanced reactivity with nuclei vs. larger particles) and/or loss mechanisms such as Ostwald ripening, intraparticle ripening or self-purification.[105, 106] However, this synthetic method suffers from extensive polydispersity and lack of control in dopant incorporation, making independent control of size and dopant concentration challenging, thus the relative roles of these parameters on the magnetostructural phase transition are difficult to assess.

In this Chapter, The evolution of MnAs nanoparticles in solution-phase synthesis and incorporation of P has been quantitatively assessed. The synthesis of discrete MnAs nanoparticles with unprecedented size uniformities, the process by which P is incorporated and means to enable independent control of particle size and dopant concentration will be discussed.

3.1. Experimental Section

3.1.1 Synthesis of MnAs nanoparticles

All the chemicals used in the syntheses described in this chapter are listed in Chapter 2 (Section 2.1). A total of 0.5 mmol of dimanganesedecacarbonyl, and 8 mL of 1-octadecene are mixed in one Schlenk flask and 4 g of TOPO and 1 mmol of triphenylarsine oxide are combined in a separate Schlenk flask under inert conditions. Both Schlenk flasks are attached to a Schlenk line followed by argon flushing and evacuation cycles over a period of 15 min. Before injection, the manganese carbonyl mixture is slightly warmed with a heat gun until the powder precursors are dissolved. The mixture is then injected under inert conditions into a 573 K solution consisting

of TOPO and triphenylarsine oxide. After injection of Mn precursor, the temperature was set to 603 K for the growth phase. The nanoparticles were isolated by rapid cooling of the reaction mixture in chloroform, followed by centrifugation, washing with hexane twice, and drying under vacuum.

3.1.2 Monitoring the growth of MnAs nanoparticles

Approximately 0.2 mL of the reaction mixture was withdrawn from the flask at certain reaction time intervals after introduction of Mn precursor. These aliquots were dispersed in 3 mL of pre-weighed chloroform. The mass of the aliquots was then determined by subtracting the mass of the chloroform from the total mass of the chloroform and the reaction aliquots. The precipitate was isolated by centrifugation, washing with hexane twice, and drying under vacuum.

3.1.3 Characterization methods

Particle size and morphology were analyzed using micrographs imaged by TEM. The crystallite size and structure were determined by using Debye-Scherer formula and comparison of PXRD patterns to phases in the Powder Diffraction File (PDF) database (release 2000), respectively. ICP-MS and EDS were employed to determine the elemental composition. The instruments employed for characterization are described in details in Chapter 2.

3.2. Results and Discussion

3.2.1 Synthesis of MnAs nanoparticles

For the synthesis of P-doped MnAs nanoparticles adopting the β-MnAs structure type at room temperature, the previously reported synthetic method was modified by slightly reducing surfactant/solvent quantities to minimize formation of carbon and phosphorus-rich amorphous aggregates (byproducts) that proved difficult to remove during isolation. Specifically, for 1 mmol Mn and As atomic concentration, the TOPO was reduced from 5g to 4g and 1-octadecene from

10 mL to 8 mL. Additionally, the temperature at which the precursor injection was performed was decreased from 603 K to 573 K to control nucleation speed, with the aim of narrowing the polydispersity. With the introduction of the Mn precursor (in 1-octadecene) to the hot TOPO solution containing the As precursor, the temperature drops about 50 degrees. The heating temperature is then set to 603 K, and it takes about 15 minutes to stabilize at that temperature.

3.2.2 Monitoring the growth of MnAs nanoparticles

Approximately 0.2 mL aliquots of the reaction mixture were taken from the reaction flask at specific reaction time intervals post-injection and quenched in 3 mL of chloroform. Formation of MnAs nanoparticles is indicated by development of color and the precipitation of a solid (either spontaneously or upon centrifugation, Figure 3.1). At one minute after injection there is no isolable product and the reaction mixture is transparent. By 2 minutes after injection, particle formation has initiated; the reaction mixture gradually turns black between 2 and 30 minutes. At ≥ 30 minutes after injection, the nanoparticles spontaneously precipitate out from the reaction mixture without centrifugation.

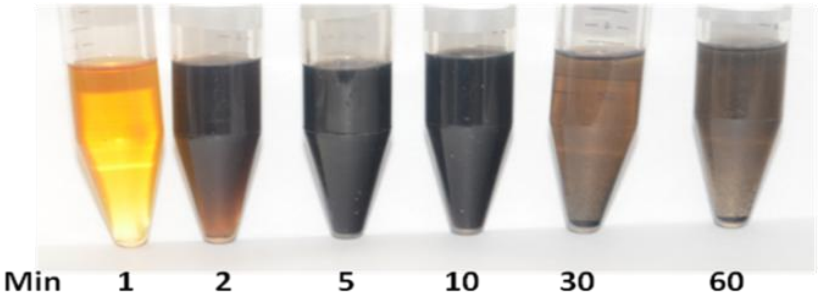

Figure 3.1 Aliquots of the MnAs reaction mixture quenched in chloroform

3.2.3 Phase and morphological characterization

The morphology and size distribution of MnAs nanoparticles from each aliquot were investigated using transmission electron microscopy. Representative TEM images of MnAs nanoparticles from each aliquot are shown in Figure 3.2 along with HR image (inset) and size

distribution histogram. The TEM micrograph indicates that MnAs nanoparticles exhibit a high degree of crystallinity, as evidenced by the presence of lattice fringes in the high contrast core of the nanoparticles. The particles have a low contrast shell, as routinely seen for all MnAs nanoparticles synthesized in our lab. Previous IR studies combined with chemical analysis are indicative of formation of amorphous manganese arsenate/ite due to surface oxidation, although phase segregation of arsenic oxides and manganese oxides cannot be ruled out.[14] The low contrast shell is present in all nanoparticles imaged, and it is not clear if this arises from *in situ* oxidation or sample exposure to air during TEM specimen preparation.[63]

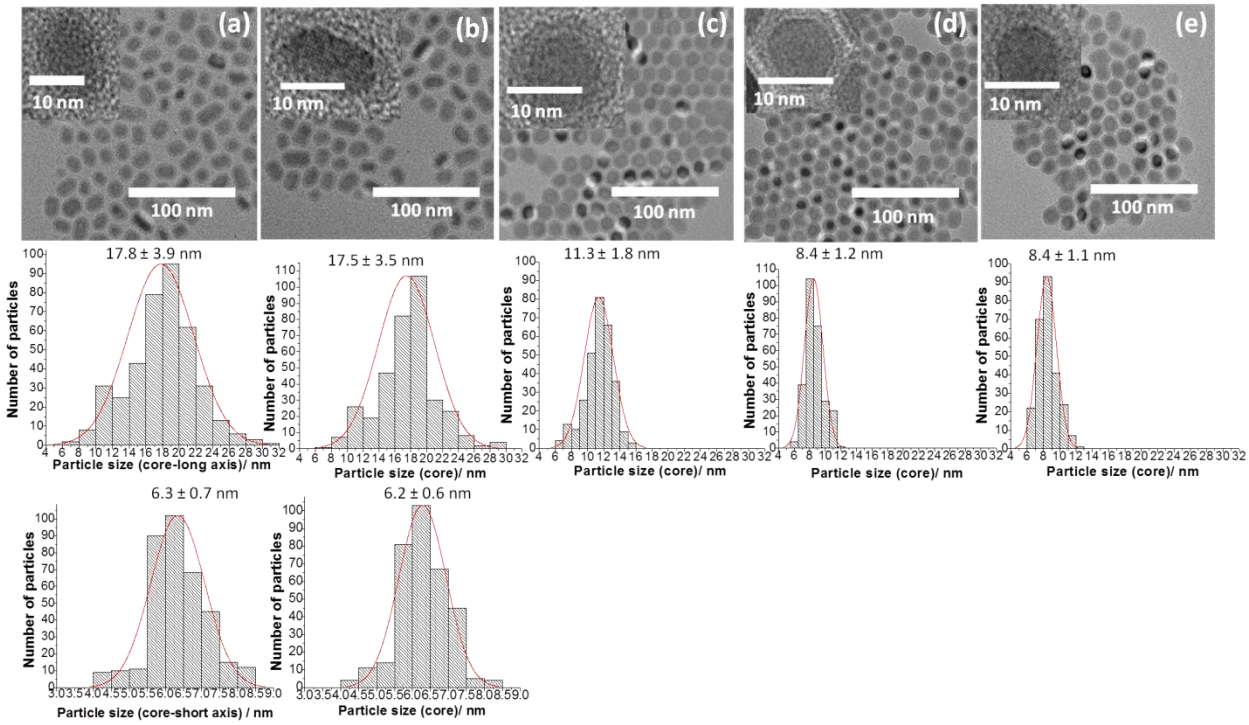

Figure 3.2. TEM images and core size distribution histogram of nanoparticles isolated (a) 2 min, (b) 5 min, (c) 10 min (d) 30 min and (e) 60 minutes after introduction of Mn precursor.

The temporal shape evolution of MnAs nanoparticles occurs in two noticeable stages as observed from TEM. The prolate spheroid shaped nanoparticles formed soon after the injection are faceted with an average size of ca. 17 nm, measured along the longest dimension (Figure 3.2

(a), (b)) and ca. 6 nm along the short axes. The second stage occurs by 10 minutes after the injection, resulting in smaller (ca. 11 nm) spherical nanoparticles. As the temperature stabilizes (after 15 minutes) the nanoparticles shrink in size (ca. 8 nm) while retaining the spherical morphology and core-shell structure. Extending the heating times beyond this point did not affect the size or morphology. At early stages in the reaction, the samples are more polydisperse, as reflected in the standard deviation for the size analysis (Table 3.1), but the polydispersity narrows considerably by the second stage of the reaction, consistent with size focusing.[107]

Room temperature PXRD pattern of nanoparticles in each aliquot is shown in Figure 3.3. Regardless of the morphology or size, nanoparticles in each aliquot show the β-MnAs structure from room temperature PXRD. The statistical core particle size calculated from TEM micrographs agrees well with the crystallite sizes calculated by the application of the Scherrer formula to PXRD patterns based on the full width at half-maximum (FWHM) of the peak at $2\theta = 32.16°$ [(111) reflection]. The shape evolution may be arising from either the temperature change associated with the introduction of the precursor, the high monomer concentration present at early reaction time, or combined effect of both.

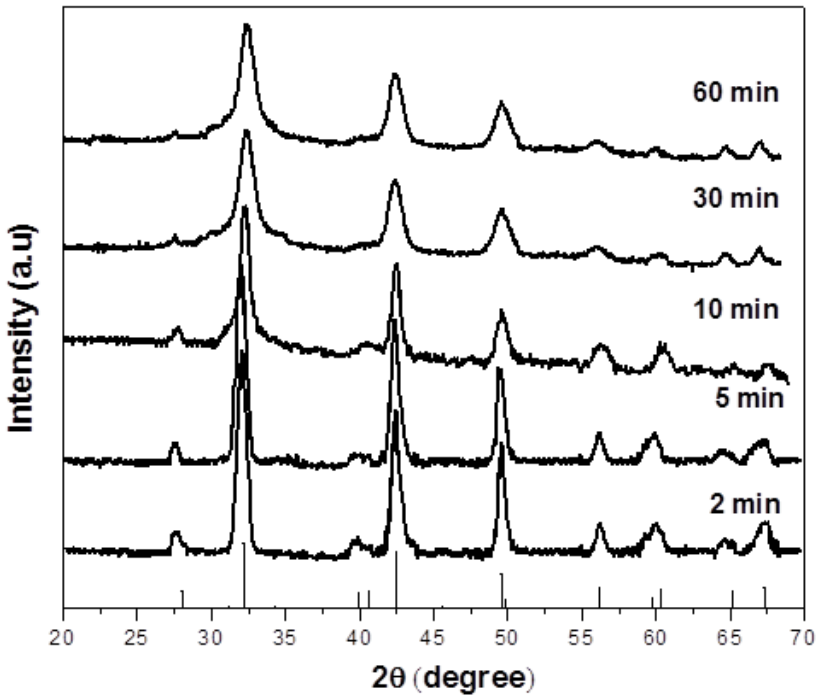

Figure 3.3. PXRD of nanoparticles in aliquots withdrawn at different time intervals (reference pattern for β –MnAs PDF#71-0923).

3.2.4 Elemental composition and growth profile analysis of MnAs nanoparticles

Figure 3.4 shows the elemental line profiles of individual nanoparticles isolated at different reaction times. For Mn and As, the signals are very intense in both the crystalline core and the amorphous shell of the nanoparticles, and these two components rise and fall together, regardless of reaction time (Figure 3.4). The fact that the shell has the same metal composition as the core is consistent with formation of amorphous arsenate/ite species, as previously reported.[14] With respect to P incorporation, the trace amount of P in the shell and in the core is seen consistently upon analysis of several independent samples of MnAs nanoparticles. The compositional homogeneity noted here is in contrast to FeAs nanoparticle synthesis reported by Desai et al.[53] where nanoparticles isolated at early stages of particle growth exhibited As concentrated near the edge of the particle whereas the core was Fe-rich, giving rise to a homogeneous particle as the reaction proceeds. FeAs nanoparticle synthesis likely occurs via

initial formation of Fe nanoparticles, which are relatively easy to form under mildly reducing conditions, that subsequently react with As to form FeAs. However, Mn nanoparticle formation requires a highly reducing environment (e.g., use of n-butyl Li) not present in this reaction; accordingly, formation of MnAs likely occurs by direct reaction of Mn and As precursors. Thus, isolated particles are homogeneous in Mn and As regardless of reaction time.

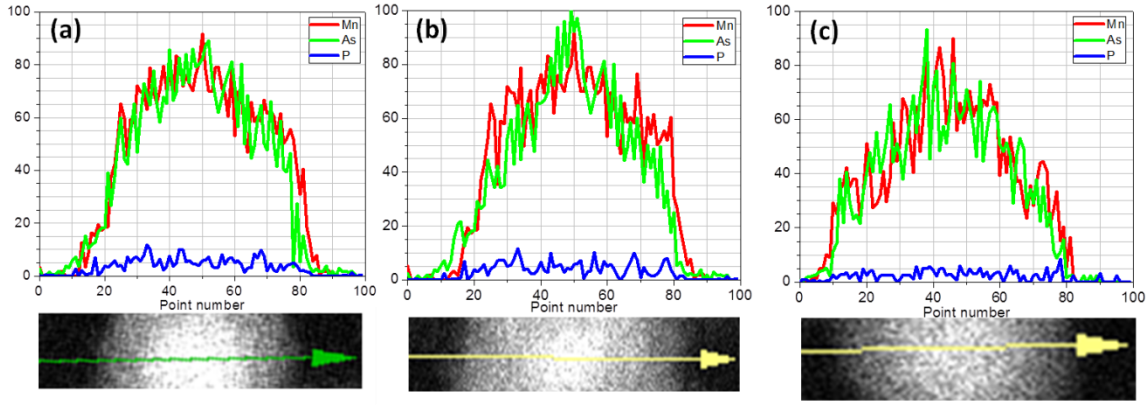

Figure 3.4. Line profile elemental analysis for a single MnAs nanoparticle (image at bottom) isolated at (a) 2 min (b) 10 min and (c) 60 minute of reaction time.

The nanoparticles resulting from the first stage of the reaction contain 4-7% phosphorus, as assessed by ICP-MS. At the second stage of particle growth, nanoparticles contain up to 5% P, with P decreasing with continued heating time (Figure 3.5). These data suggest that incorporation may be limited to the early stages of the reaction and loss dominates at later times until equilibrium is achieved, resembling a self-purification process. In contrast to the previously reported synthetic method, longer reaction times do not result in a change in particle size after 10 minutes, but the %P continues to decrease up to 60 minutes, at which time the concentration levels off at ca 1.5%.

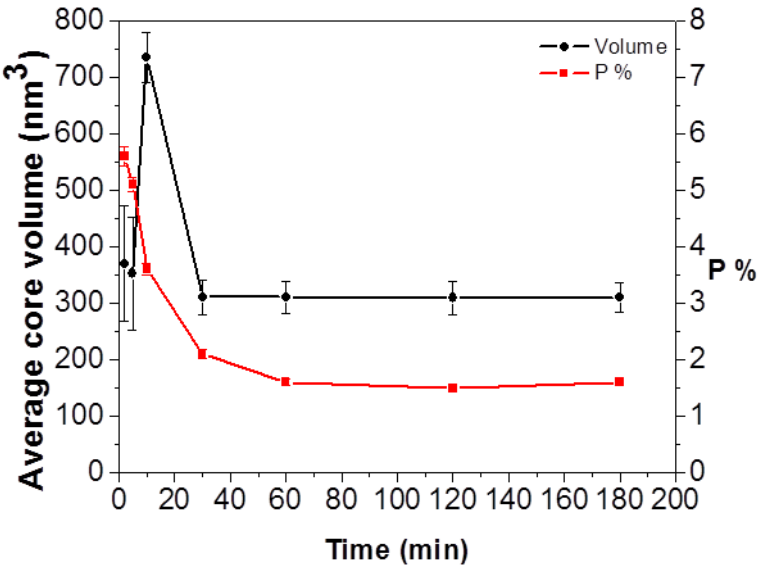

Figure 3.5. Correlation between reaction time, particle volume and P incorporation.

Table 3.1. Crystallite and particle sizes, core volume and P% of MnAs nanoparticles at different reaction times ([a]Based on PXRD data. [b]Based on TEM data. [c]Based on ICP-MS data)

Reaction time (min)	Crystallite size (nm)[a]	Particle core size (nm)[b]		Core volume (nm^3)[b]	P% [c]
		Long axis	Short axis		
2	19.7 (±1.1)	17.8 (±3.9)	6.3 (±0.7)	370.1 (±109)	5.6 (±0.2)
5	19.2 (±0.9)	17.5 (±3.5)	6.2 (±0.6)	352.4 (±101)	5.1 (±0.1)
10	12.1 (±0.7)	11.3 (±1.8)	11.3 (±1.8)	735.6 (±45)	3.6 (±0.1)
30	9.3 (±0.8)	8.4 (±1.2)	8.4 (±1.2)	310.3 (±31)	2.1 (±0.1)
60	8.9 (±0.5)	8.4 (±1.2)	8.4 (±1.1)	310.3 (±28)	1.6 (±0.1)

The determination of monomer concentration for a crystalline system is important for understanding the kinetics of particle growth and the development of a reproducible method for synthesis of nearly monodisperse nanoparticles. In the current system, direct determination of monomer concentration is difficult as the nanoparticle formation takes place at a high temperature. In this study, this information is indirectly acquired by using the method developed

by Peng et al.[108] In this method, the monomer concentration is calculated by determining the number of atoms in the form of nanoparticles. The mass of the aliquots was determined by subtracting the mass of the chloroform from the total mass of the chloroform and the reaction aliquots. The temporal variation of the monomers in the reaction mixture by mass was indirectly probed by isolating the precipitate from the chloroform aliquot by centrifugation. The precipitate was washed several times with hexane and ICP-MS was performed to determine elemental composition. Thus, the monomer concentration (as weight %) in the growth solution at a given moment is calculated by excluding the Mn or As in the form of nanoparticles from the total amount of Mn or As atoms added into the flask.

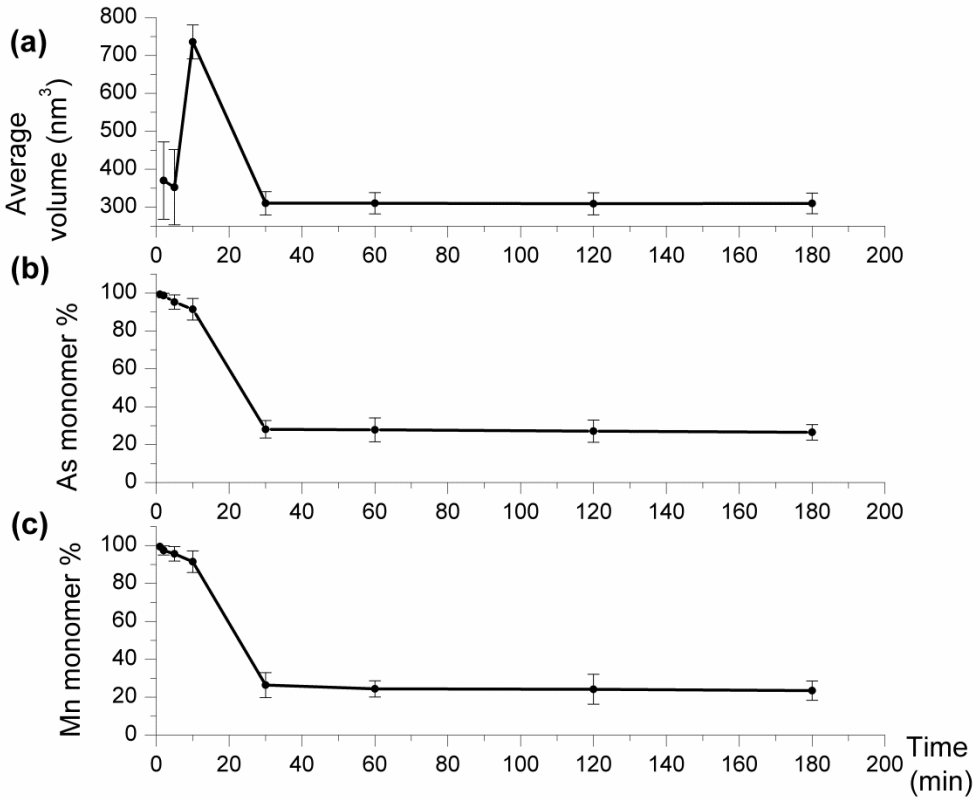

Figure 3.6. (a) Average core volume of the MnAs nanoparticles, temporal (b) As monomer (c) Mn monomer percentages in the reaction mixture over time.

The Mn and As monomer percentage one minute after injection is 100% (Figure 3.6), confirming the observation of a clear yellow-orange solution in Figure 3.1. This color is characteristic of $Mn_2(CO)_{10}$ dissolved in $CHCl_3$. This is consistent with the expectation that there is no isolable product one minute after Mn precursor injection. At short times post-injection (2-5 minutes), the Mn and As monomer percentages remain high (>95%) and anisotropic (prolate) spherical particles form with a volume of ca 350 nm^3. As the monomer continues to react, the particles become spherical and the volume maximizes (ca 740 nm^3) at 10 min as the second stage of the particle growth begins, with the monomer concentration remaining quite high (90%). Between 10 and 30 minutes, the monomer concentration falls rapidly to 20%, correlating with a decrease in particle volume to ca 300 nm^3, at which point both the monomer concentration and size remains constant for longer times. It is not clear if this residual 20% monomer percentage represents an equilibrium or formation of a non-reactive (soluble) by-product, but the absence of color in the clear supernatant at 30 min reaction time and beyond suggests that the $Mn_2(CO)_{10}$ is completely consumed. Kinetically persistent intermediates that are slow to transform may arise from reaction-limited processes; if sufficiently small, these may not be isolated by our protocol. In such a case, the determined "monomer concentration" in Figure 3.6 may actually reflect cluster intermediates (or a mixture of such intermediates and true monomers). The presence of a constant and significant "monomer" concentration, if not an unreactive byproduct, would reflect an equilibrium between dissolution and growth at this temperature (i.e., this is the critical size for the employed monomer concentration).[107] Deviation from classic nucleation theory to reaction limited processes and the formation of kinetically persistent intermediates is characteristic of highly covalent systems, such as InP, and it is not surprising to see similar phenomena in MnAs.[109, 110] However, given the highly oxophilic character of Mn, the stability of manganese

oxides to reduction, and the fact that isolable Mn oxides form as byproducts under similar reaction conditions (attributed to adventitious oxidation), the apparent residual monomer concentration most likely reflects a non-reactive oxidized byproduct.

Intriguingly, growth profile analysis enables to uncover the main reason for the lack of reproducibility and the extensive polydispersity in the previously reported synthesis method. It is evident that there are differences between products isolated as quenched aliquots and the previous synthesis in which solutions were allowed to air cool before isolation. In order to assess the role of quenching on sample quality and reproducibility, an aliquot was withdrawn from the reaction mixture at 603 K into chloroform, 60 minutes after Mn precursor injection. Right after withdrawal of this aliquot, heating was discontinued and the reaction mixture was allowed to cool down. The second and third aliquots were withdrawn when the temperature of the reaction mixture reached 353 K and room temperature, respectively.

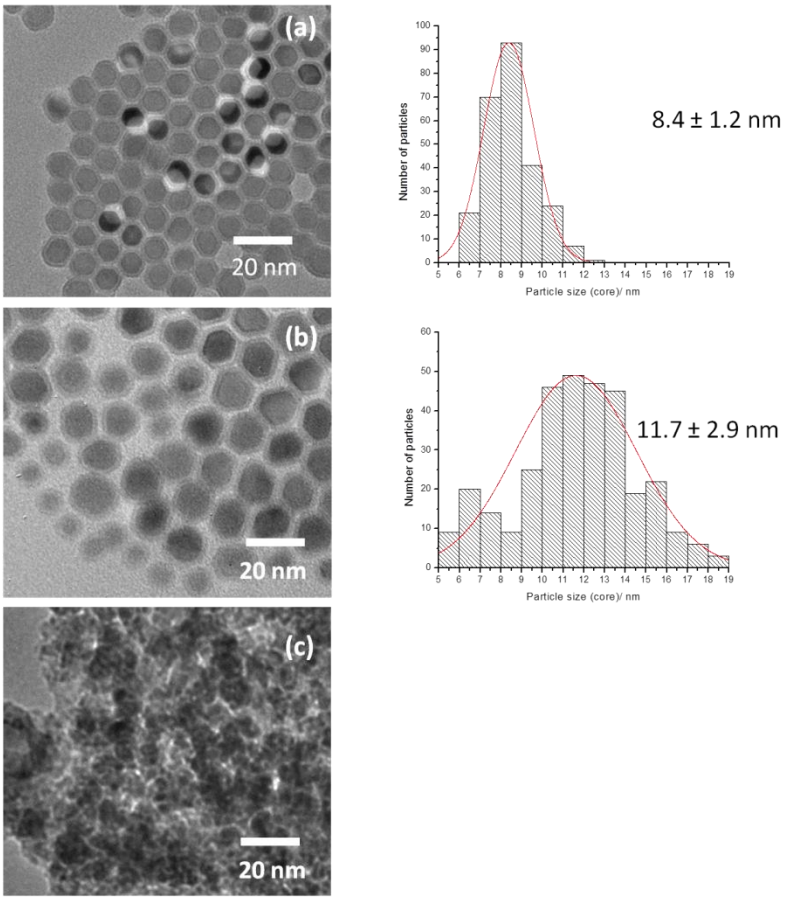

Figure 3.7. TEM images and core size distribution histograms of particles isolated at (a) 603 K and (b) 353 K; TEM image of particles isolated at (c) room temperature.

TEM images of purified aliquots (Figure 3.7) reveal that nanoparticles isolated at high temperature (603 K) are uniform in terms of size and morphology. Nanoparticles isolated at 353 K upon cooling of the reaction mixture are larger and polydisperse, and the solid isolated from the third aliquot (room temperature) shows considerable aggregation. Excessive aggregation prevented meaningful size determination in the room temperature sample, hence, no histogram is shown. The 353 K data are suggestive of Ostwald ripening (in which larger particles grow at the expense of smaller ones). The temperature has an impact on diffusion kinetics, and slow cooling to room temperature disturbs the monomer concentration gradient between the stagnant solution and the bulk solution. [111] Due to the strong size-dependant solubility on the nanoscale, depletion

of monomers results in defocusing of size distribution making smaller nanoparticles shrink and larger particles grow. This observation indicates the necessity of high temperature isolation of nanoparticles for obtaining high quality samples. However, rapid cooling of the reaction flask at 603 K by immersing the flask in cold water bath results in increased polydispersity and the average particle size increase to ca. 24 nm (Figure 3.8), indicating the necessity of quenching the reaction mixture in a solvent in contrast to rapidly cooling the reaction flask.

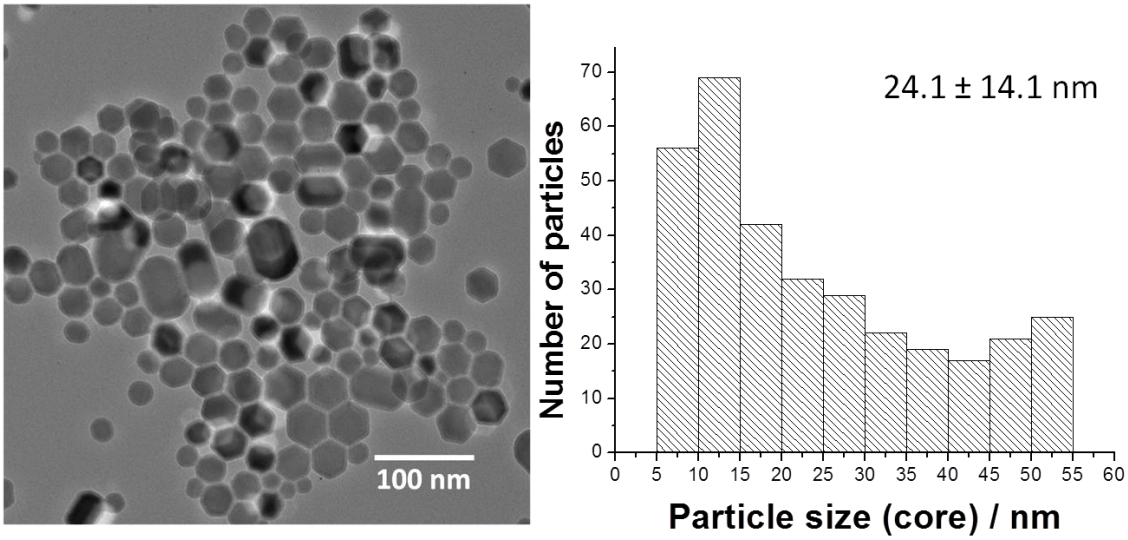

Figure 3.8. TEM images and core size distribution histograms of particles isolated by rapid cooling of reaction flask at 603 K

3.3. Conclusions

The evolution of solution-phase MnAs nanoparticle formation and incorporation of P has been quantitatively assessed. The dimensions of the nanoparticles change simultaneously with the monomer concentration change and the particles become morphologically uniform when the temperature stabilizes and ca 20% monomer (or unreactive byproduct) remains. The temperature at which the nanoparticles were isolated controls the particle size and polydispersity; high temperature isolation of nanoparticles is required to achieve narrow polydispersity and ultimately

leads to highly reproducible product. Adventitious phosphorus incorporation from the solvent TOPO occurs during nucleation, and P is subsequently lost, likely due to self-purification, attaining an equilibrium concentration of ca 1.5% P. Overall, this study demonstrates a reproducible synthetic method enabling fine control of size and composition for a highly covalent system, MnAs, with a high degree of size uniformity.

CHAPTER 4 INDEPENDENT CONTROL OF SIZE AND PHOSPHORUS CONCENTRATION OF DISCRETE TYPE-B MnAs NANOPARTICLES: SIZE AND %P DEPENDENT MAGNETOSTRUCTURAL PROPERTIES

4.1. Introduction

Anion doping is an effective method to overcome the large thermal hysteresis of MnAs and tune the magnetocaloric properties for refrigeration applications near room temperature, but there is a lack of knowledge of how particle size and the extent of doping affect magnetic properties.[31, 83, 101] Nanostructures (200 nm-μm particle size) of $MnAs_{1-x}P_x$ (x = 0.006 and 0.01) prepared by mechanical alloying followed by annealing, show a reduction of thermal hysteresis without impacting the magnetic entropy change. Due to the poly-crystalline nature of the samples, it is not clear if the observed reduction of thermal hysteresis is due to size or strain effects.[101] This precludes the interpretation of size effect in $MnAs_{1-x}P_x$ nanomaterials. Our group has recently discovered the presence of P in type-B MnAs, made by rapid nucleation, resulting in a suppressed first order transition and adoption of the β-MnAs structure at room temperature. P incorporation is attributed to reaction of solvent, trioctylphosphine oxide (TOPO).[63]

During the original synthesis, as the precursors and reaction temperature are kept the same, the reaction time determined the particle size and final doping concentration of P in the MnAs nanocrystals. As the reaction time increases, the particle size increases and P incorporation decreases. Accordingly, this method does not enable independent variation of size and dopant concentration, thus the relative roles of these parameters on the magnetostructural phase transition are difficult to assess. In Chapter 3, a reproducible synthetic method enabling fine control of size and composition with a high degree of size uniformity was described. In the present work, independent control of nanoparticle size and P incorporation is determined in order

to understand the roles of size and chemical pressure on the magnetostructural phase transition. This is achieved by exploiting the new synthetic method described in Chapter 3

4.2. Experimental section

All the chemicals used in the syntheses described in this chapter are listed in Chapter 2 (Section 2.1). The instruments and the methods used for characterization of as-prepared nanoparticles are also discussed in Chapter 2.

4.2.1 Synthesis of 8 nm size MnAs Nanoparticles with different P concentrations

The experimental procedure for synthesis and purification of MnAs nanoparticles of 8 nm size with different %P is same as the procedure described in Section 3.1.1. In brief, nanoparticles were synthesized by a hot injection method followed by high temperature quenching of the reaction mixture at different reaction times (30 minutes and 10 hours). In this synthesis, a total of 0.5 mmol of manganese carbonyl dissolved in 8 mL of 1-octadecene is injected into a mixture of 4 g of TOPO and 1 mmol of triphenylarsine oxide maintained at 573 K.

4.2.2 Synthesis of 5 nm size MnAs Nanoparticles with different P concentrations

The procedure described in Section 3.1.1 was slightly modified to synthesize MnAs nanoparticles with a 5 nm crystallite diameter. One variety of 5 nm MnAs nanoparticles was synthesized by using 16 mL of 1-ODE while maintaining the other reaction conditions the same. The nanoparticles were isolated after 10 hours of reaction time by the rapid cooling technique and purified as described in Section 3.1.1. The other variety of 5 nm MnAs nanoparticles was prepared by using 1 mmol of TOP in place of TOPO while maintaining other reaction conditions the same. The nanoparticles were isolated after 2 hours of reaction time by the rapid cooling method and purified as previously described.

4.3. Characterization

Particle size, morphology and size distribution were analyzed using micrographs imaged by TEM. The crystallite size and structure were determined by using the Scherrer formula and comparison of PXRD patterns to phases in the Powder Diffraction File (PDF) database (release 2000), respectively. ICP-MS and EDS were employed to determine the elemental composition. The temperature-dependant structural changes were probed with temperature-dependant PXRD. Magnetic measurements were collected using MPMS and PPMS instruments in collaboration with Prof. Nadgorny and co-workers.

4.4. Results and discussion

As previously discussed in Section 1.3.2.2, SPAP offers the advantage of tuning the elemental composition and particle size of nanomaterials. Thus, this method was used synthesize type-B MnAs nanoparticles in which the concentration of P dopant and particle size are independently controlled. Table 4.1 summarizes the variables in the synthesis and the resulting nanoparticle size and %P. During the synthesis of ~ 8 nm nanoparticles, isolation at two reaction times resulted in two different P amount while maintaining the same particle size. The shorter reaction time (30 min) resulted in 2.1% P incorporation and the longer reaction time (10 h) resulted in lesser P (0.9%) incorporation. The P-uptake was evaluated by EDS in the TEM and ICP-MS on bulk sample and both are in good agreement. However, the data listed in the Table 4.1 are based on ICP-MS data as it provides an average value with a higher degree of precision.

Table 4.1 Synthetic parameters for independent control of particle size and %P of type-B MnAs nanoparticles.

	Variable		
Particle core size (nm)	Reaction time (hrs)	Coordinating solvents/amount	%P
8.4 (±1.2)	0.5	TOPO 4 g/1-ODE 8mL	2.1 (±0.3)
8.4 (±1.1)	10	TOPO 4 g/ 1-ODE 8 mL	0.9 (±0.1)
5.1 (±0.3)	10	TOPO 4 g/1-ODE 16 mL	0.8 (±0.1)
4.9 (±0.4)	2	TOP/1-ODE 8mL	1.9 (±0.2)

In order to synthesize ca. 5 nm size MnAs nanoparticles with ~ 0.8%P, the amount of 1-ODE used was doubled and the reaction time was extended to 10 hours. We hypothesize that the excess amount of 1-octadecene contributes to dilution of the reaction mixture; thus, the monomer addition is slowed and particle growth is occurring under controlled conditions. The long reaction time enables ripening to occur, reducing the concentration of P in the particle as described in Chapter 3.

Adventitious doping of P from a relatively unreactive source (TOPO) suggests that intentional P doping should be facile. In order increase the concentration of P in doped nanoparticles, the original synthetic process was followed, but 1 mmol of trioctylphosphine (TOP), a more reactive P source, was used in place of TOPO. Replacement of TOPO with TOP results in nanoparticles of *ca.* 5 nm with ~1.9 % P incorporation. The tight binding ability of TOP controls the particle growth, results in slightly smaller nanoparticles.[112]

The TEM images and the size distribution histograms of the as prepared nanoparticles (ca. 8 and 5 nm) are shown in Figure 4.1. The particles consist of a high contrast spherical core and a low contrast amorphous shell. A high degree of crystallinity is indicated by the presence of lattice fringes in the high contrast core of the nanoparticles. However, the amorphous shell of the ca. 5 nm nanoparticles is slightly thicker than that of the ca. 8 nm particles. Based on prior studies, the amorphous shell is attributed to surface oxidation.[14] Accordingly, the larger surface-to-volume ratio of smaller nanoparticles provides a larger surface area for oxidation, resulting a slightly thicker shell. The size distribution histograms show a high degree of sample uniformity with respect to size and polydispersity.

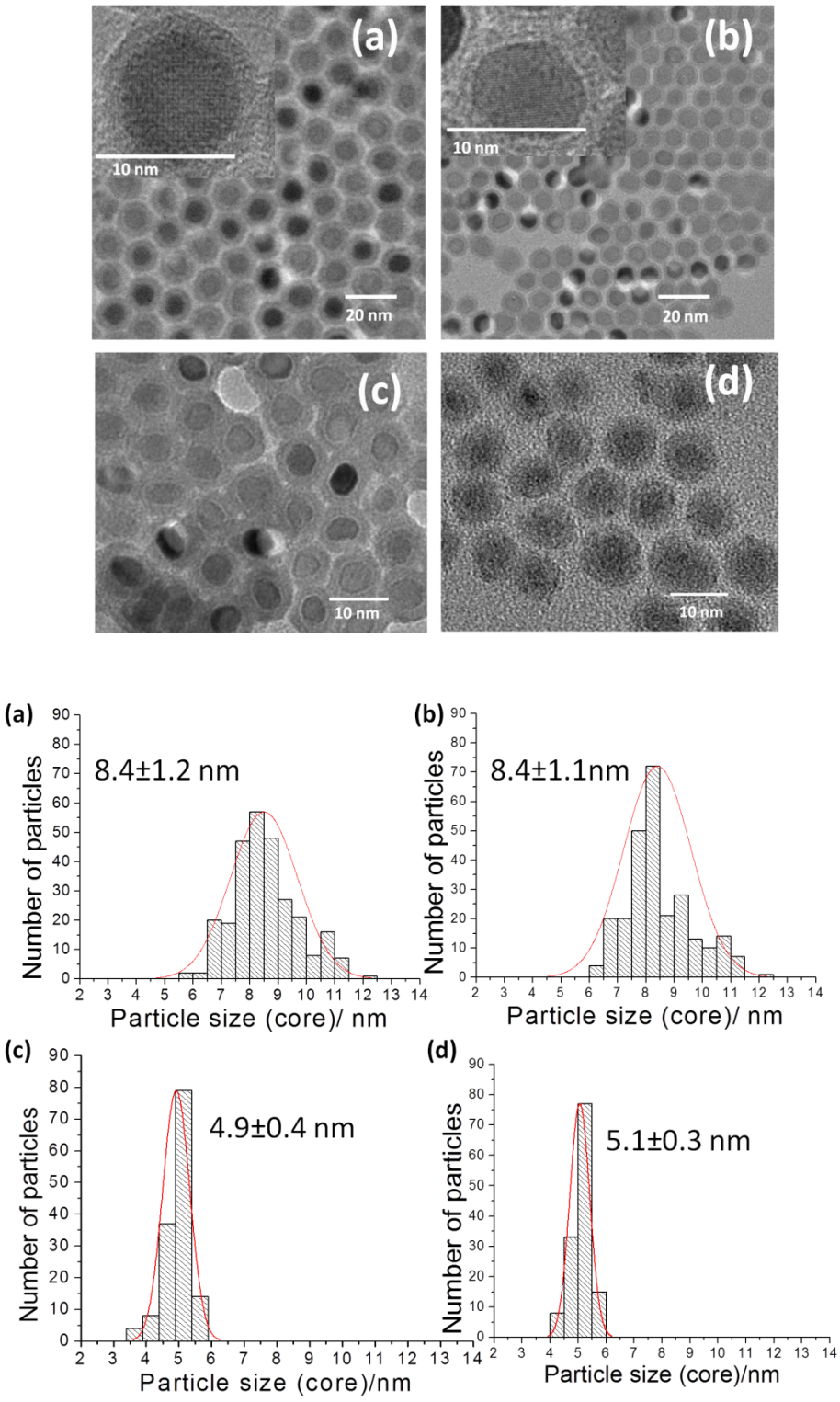

Figure 4.1 TEM images and size distribution histograms of type-B MnAs nanoparticles with (a) ~8 nm and 2.1%P (b) ~8 nm and 0.9%P (c) ~5 nm and 1.9%P and (d) ~5 nm and 0.8%P

Room temperature PXRD patterns for all the samples were acquired in the range of 2θ =20°-70°. Regardless of the changes in synthetic parameters, all the samples show a PXRD pattern that can be indexed to β-MnAs (Figure 4.2). The average crystallite sizes calculated for each sample by the application of the Scherrer formula to PXRD patterns agrees well with the average core size obtained by size distribution histograms, which indicates the size uniformity within each sample.

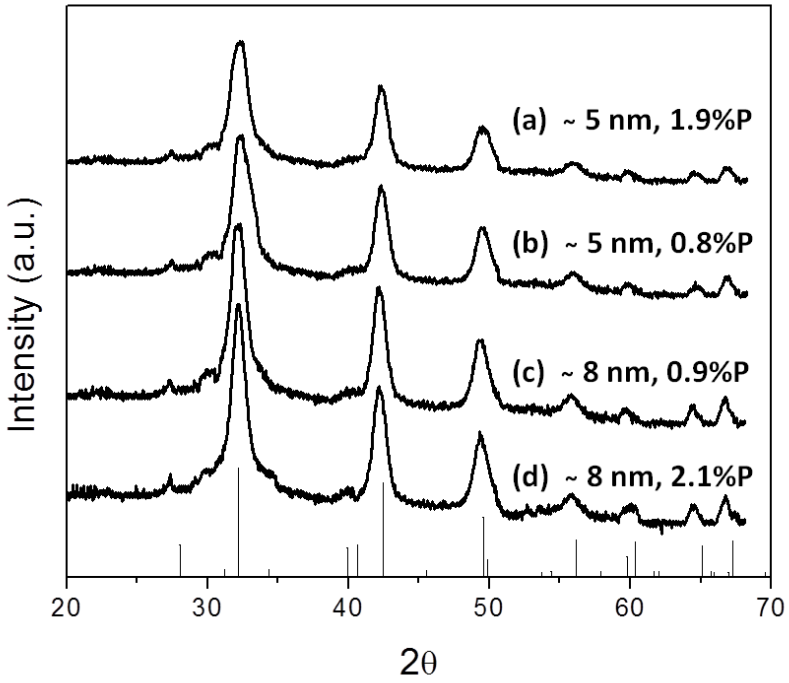

Figure 4.2 Room temperature PXRD for type-B MnAs nanoparticles (a) ~5 nm and 1.9%P (b) ~5nm and 0.8%P (c) ~8 nm and 0.9%P and (d) ~8 nm and 2.1%P

In order to probe the effect of size and doping on the phase transition temperature, the temperature dependant PXRD of all of the samples were collected the range of $2\theta = 48\text{-}51^{o}$. The diffraction patterns were collected first upon cooling, followed by warming. The lowest and highest temperatures and the temperature intervals were determined based on the nature of the

sample and limits of the instrument. The structural transformations form β to α on cooling and back to β on warming were quantitatively determined after each scan and the lowest and highest temperature for each sample was determined based in the relative quantities of phases observed at each temperature. The lowest temperature achievable with the instrument employed was 93 K, thus, in the event a sample does not show complete structural conversion from β to α on cooling by the lowest limit of the instrument, 93 K was considered as the lowest temperature for that particular sample. Figure 4.3 shows a series of XRD scans of the as-prepared type-B MnAs nanoparticles. Table 4.2 summarizes the information extracted from Figure 4.3.

The data in Figure 4.3 show that the transformation of type-B MnAs nanoparticles from β to α structure on cooling is reversible upon warming. In the scans, the (110) reflection of α-MnAs and the (013) reflection of β-MnAs can be easily identified. At room temperature, samples representing data in Figure 4.3 (a) to (c) adopt exclusively β-MnAs structure (Appendix A) and they initiate the structural phase transition at different temperatures upon cooling below room temperature. The onset of β to α structural phase transition was determined using the computed relative quantities of each phase where >1% α–structure is observed. Similarly, onset of α to β structural transition was identified when >1% β–structure is observed. The temperature intervals scans were collected indicate the onset range instead of the true onset temperature.

The sample representing Figure 4.3 (a) initiates the structural phase transition in 213-183 K temperature range and the appearance of (110) reflection of α-MnAs upon cooling indicates the initiation of structural transition. By 183 K, this sample shows 4.7% α-structure. However, it does not show complete structural transformation by 93 K, the lowest temperature accessible with the instrument employed. At 93 K, this sample retains 50.6% of β-phase (Appendix). Upon warming, 4.8% α-structure is observed at 183 K indicating a negligible hysteresis upon

warming. However, this sample show a reduction of lattice parameters, resulting a 0.9% volume reduction compared to bulk.[113]

It is evident that the sample represented by Figure 4.3 (b) initiates the β to α structural transition just below room temperature (298-283 K) with 8.2% α-structure by 283K (Appendix). This sample shows complete structural transformation by 213 K, and upon warming, α to β initiates by 263 K. Approximately 15% α-structure is observed at 283 K upon warming (Appendix), indicating a structural hysteresis. Compared to the sample represented by Figure 4.3 (a), this sample has slightly less P concentration and show a 0.8% volume reduction compared to bulk. However, the sample completely transform to β-structure by 298 K upon warming.

The ca. 5 nm sample with 1.9%P (Figure 4.3 (c)) initiates the transition from β to α in the 243-223 K range with 16.5% α-structure at 223 K (Appendix), and shows a complete structural conversion to α-phase in by183 K. Upon warming, α to β structural transition initiates by 203 K. Upon warming, 62.9% α-structure is observed at 223 K indicating reflecting a structural hysteresis. Approximately 0.9% volume reduction is observed for this sample.

In contrast to all the other samples discussed above, nanoparticles with ca. 5 nm with 0.8% P (Figure 4.3 (d)) show 3.7% of α-phase at 298 K (Appendix). The presence of α-structure at room temperature can be attributed to formation of MnAs nanoparticles adopting α-structure during the synthesis. Upon cooling, 5.9% α-phase is observed by 283 K (Appendix). This sample shows a complete structural conversion to α-structure by 213 K, and complete conversion from α to β-structure upon warming by 318 K, reflecting a 10 K hysteresis and approximately 1.0% volume reduction.

Table 4.2 Onset temperature (K) for β to α transition, β to α completion temperature (K) and relative % α-phase at β to α onset for as prepared type-B MnAs nanoparticles

Crystallite size (nm)	%P	β to α onset temperature (K)	β to α completion temperature (K)	Relative % α at onset temperature
8.4(±1.2)	2.1(±0.3)	183	< 93	4.7
8.4(±1.1)	0.9 (±0.1)	283	223-213	8.2
4.9(±0.4)	1.9(±0.1)	223	193-183	16.5
5.1(±0.3)	0.8(±0.2)	283	223-213	15.8

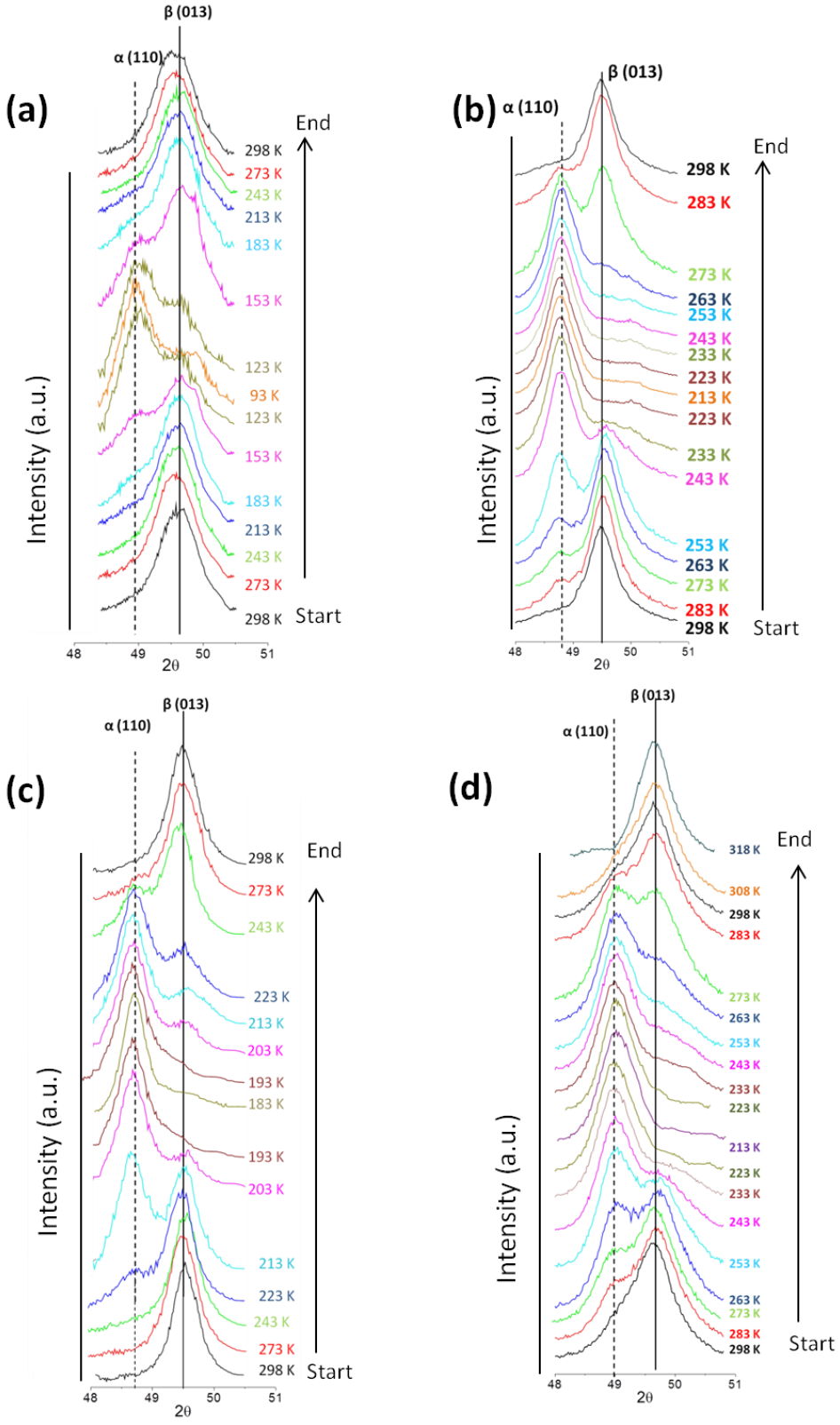

Figure 4.3 Temperature dependent PXRD for type B MnAs nanoparticles with (a) ~8 nm and 2.1%P (b) ~8 nm and 0.9%P (c) ~5 nm and 1.9%P and (d) ~5 nm and 0.8%P

The incomplete structural transformation of ~8 nm particles with 2.1%P by 93 K may be due to the presence of some nanoparticles with higher amount of P incorporated (> 3%) that resist structural transformation within the temperature range studied. Previous work on $MnAs_{1-x}P_x$ compounds report that the α-phase is stable only up to 3%P.[84] Thus, the presence of nanoparticles with >3%P is the likely reason for the behavior observed in the sample with ~8 nm nanoparticles with an average 2.1%P. We surmise that the short reaction time may be giving rise to inhomogeneous distribution of the P-dopant in the MnAs nanoparticles.

Zhang et al.[63] reported 1.033% shrinking of unit cell volume in type-B MnAs nanoparticles compared to bulk MnAs at 295 K due to lattice parameter compression. The samples investigated in this study show similar values for unit cell volume reduction. Substitution of P for As in type-B MnAs is considered to be responsible for unit cell compression resulting in a decrease in the phase transition temperature. In bulk MnAs, the degree of P incorporation has lowered the phase transition temperature from ~315 to 280 K when %P increased up to 3%.[84] Thus, the lowering of phase transition temperature can be attributed to P incorporation rather than the size effect. However, for > 3%P, α-structure is not stable below the temperature second order phase transition takes place (i.e. β-structure below 400 K).[114]

The computed relative quantities of β and α phases at each temperature shows a phase coexistence range in addition to the hysteresis. Zhang et al.[63] reported a large rang of phase coexistence for ca. 21 nm type-B MnAs nanoparticles that extend above room temperature with a significant hysteresis. However, the nanoparticles in this dissertation study are considerably smaller than that of Zhang et al. reported. This phase coexistence observation defies the Gibbs phase rule that states phases of the same chemical composition can coexist only at a single temperature.[115] The phase coexistence of nanoparticles in this dissertation research can be

attributed to heterogeneity of the nanoparticles in terms of %P, and possibly also due to variation of size, surface properties and defects. Thus the individual particles are likely to transform abruptly while the sample as a whole exhibit phase coexistence. A similar observation has been reported on MnAs disks epitaxially grown on GaAs (001), where a sample of ca. 80 nm diameter MnAs disks show a 45 K coexistence range.[35] However, individual disks remained single domain and undergo an abrupt transformation.

4.4.2 Effect of size and %P on the magnetic transition

The magnetic properties and the structure are highly correlated in bulk MnAs correlating to the α to β structural transition. Bulk MnAs is known to be paramagnetic above 315K. The β phase is also not stable above 373 K under ambient conditions as there is a β to α second order phase transition at this temperature. Assuming the existence of a strong correlation between structure and magnetic behavior, the molar magnetization of as-prepared type-B MnAs nanoparticles were acquired to probe the effect of size and dopant concentration on the magnetic phase transition. The magnetic data were first collected on cooling followed by heating, thus the magnetization curve on cooling represents the native behavior of as-prepared type-B MnAs nanoparticles. Figure 4.4 shows molar magnetization data and Table 4.3 summarizes the magnetic data.

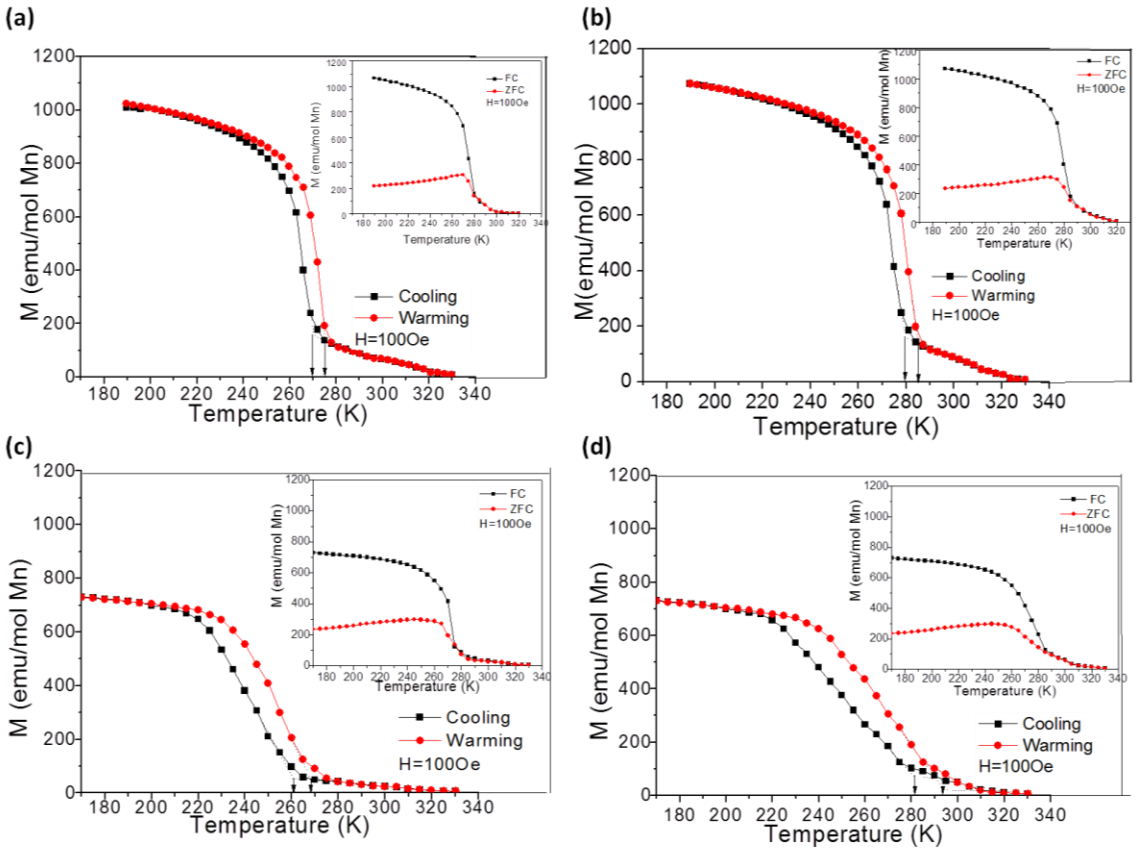

Figure 4.4 Temperature dependent molar magnetization measurements for type-B MnAs nanoparticles with (a) ~8 nm and 2.1%P (b) ~8 nm and 0.9%P (c) ~5 nm and 1.9%P and (d) ~5 nm and 0.8%P

The temperature dependant molar magnetization curves of all the samples show a small magnetic susceptibility at the warmest end of the scans demonstrating consistency with the low-spin paramagnetic state in the β-phase. As the samples are cooled down, all the samples show a distinct increase in magnetic susceptibility due to a ferromagnetic transition as previously reported,[14] and the Curie temperature, T_C, is below room temperature. The T_C and the saturating temperature, T_{Sat}, observed upon cooling do not show the same values upon warming, thus a hysteresis loop is created. The hysteresis (Table 4.3) may be due to the thermal loss resulting from magnetostructural transition. The temperature difference between T_C cooling and T_{Sat} cooling (or T_C warming and T_{Sat} warming) reflect the phase-coexistence temperature range. All

the samples show a large range (> 50 K) of phase-coexistence from temperature-dependant magnetic data. The phase-coexistence of nanoparticles is possibly due to heterogeneity of the nanoparticles in terms of P concentration, slight variation of sizes within one sample, surface properties and defects. Hence, the individual particles are likely to transform abruptly while the sample as a whole exhibit phase coexistence.

Table 4.3 Magnetic data of as prepared type-B MnAs nanoparticles

	~8 nm with 2.1%P	~8 nm with 0.9%P	~5 nm with 1.9%P	~5 nm with 0.8%P
T_C on cooling (K)	270	280	260	282
T_C on warming (K)	275	285	268	293
Hysteresis (K)	5	5	8	11
Phase-coexistence (K)	~50	~50	~75	~80
Blocking temperature (K)	270	270	245	245
Coercivity (Oe)	40	40	200	200

The slightly larger molar magnetization observed in ca. 8 nm nanoparticles compared to ca. 5 nm nanoparticles could be due to presence of lesser paramagnetic materials rather than an intrinsic size effect. The temperature dependant molar magnetization data are slightly shifted compared to their temperature dependant PXRD data (Table 4.4). It is evident that the magnetic data show the initiation of phase transition at a somewhat higher temperature than the temperature dependant PXRD data. This is likely due to the responsiveness of magnetometry techniques.

Table 4.4 T_C on cooling and warming. [a]Based on temperature dependant-PXRD data and [b]based on temperature-dependant magnetization data

	~8 nm with 2.1%P	~8 nm with 0.9%P	~5 nm with 1.9%P	~5 nm with 0.8%P
T_C on cooling (K) [a]	183	283	223	283
T_C on warming (K) [a]	< 93	263	203	263
T_C on cooling (K) [b]	270	280	260	282
T_C on warming (K) [b]	275	285	268	293

In order to probe the effect of particle size and %P on blocking temperature, T_B, the temperature-dependant molar magnetization measurements (Figure 4.4 insets) were collected upon warming without an external field for Zero-Field-Cooling (ZFC). During the ZFC measurements, the sample is cooled in the absence of an external field, thus the moments are locked in their random orientations at lower temperatures. Upon heating, sufficient thermal energy is provided to overcome the energy barrier and the moments begin to align in one direction. As temperature is increased further, a cusp representing the blocking temperature is observed, above which nanoparticles become superparamagnetic. Theoretically, the mentioned increase in magnetization is abrupt and continuous. However, for a sample of nanoparticles with a size distribution, a broad maximum can be expected as the individual particles have slightly different blocking temperatures with respect to their size and/or chemical composition. As the temperature is increased further, the thermal energy causes the random orientations to dominate, thus a decrease of magnetization is observed. In Field Cooling (FC), the sample is cooled under an external magnetic field of 100 Oe. Under FC conditions, upon cooling, the moments are locked along the direction of external magnetic field, thus the saturation is observed at lower temperatures. The FC curve shows a

gradual decrease with increasing temperature and the FC and ZFC curves coincide at higher temperatures.

The ZFC curves of ca. 8 nm nanoparticles show a slightly broader maximum compared to ca. 5 nm nanoparticles. This observation can be attributed to the particle size distribution as the size distribution histograms indicate slightly larger standard deviations for ca. 8 nm nanoparticles compared to ca. 5 nm nanoparticles. Nanoparticles with size and/or composition variation can have a distribution of energy barriers.[77] The blocking temperature of ca. 8 nm nanoparticles appear to be around 270 K while ca. 5 nm nanoparticles show it around 245 K. In general, the blocking temperature increases as the nanoparticle size increases because larger particles can withstand the thermal energy as the single magnetic domain is larger, thus, more energy is needed to overcome the energy barrier. In the present case, T_B is close to T_C, surprising for such small particles and an indication of large magnetic anisotropy.

The molar magnetization vs. applied magnetic field (H) data obtained at 300 K (Figure 4.5) show coercivity for all the samples above the apparent blocking temperature. However, the coercivity values observed for all the samples were below 250 Oe (Table 4.3). Smaller particles (ca. 5 nm) show a larger coercivity and it appears that %P does not significantly affect the coercivity. Steren and co-workers have observed an anomalous behavior of coercivity as a function of temperature for MnAs films with various thicknesses grown on GaAs substrate. The coercivity is reported to be almost constant up to 200 K (~200 Oe for 66 nm, 100 Oe for 100 nm, and 50 Oe for 200 nm films) and then increases at higher temperature. They surmise that this behavior may be observed due to phase coexistence.[116] However, in this study, the temperature dependence of coercivity was not probed. The coercive magnetic behavior observed at 300 K

could be due to a small fraction of unblocked nanoparticles at room temperature or the surface nature of the nanoparticles.

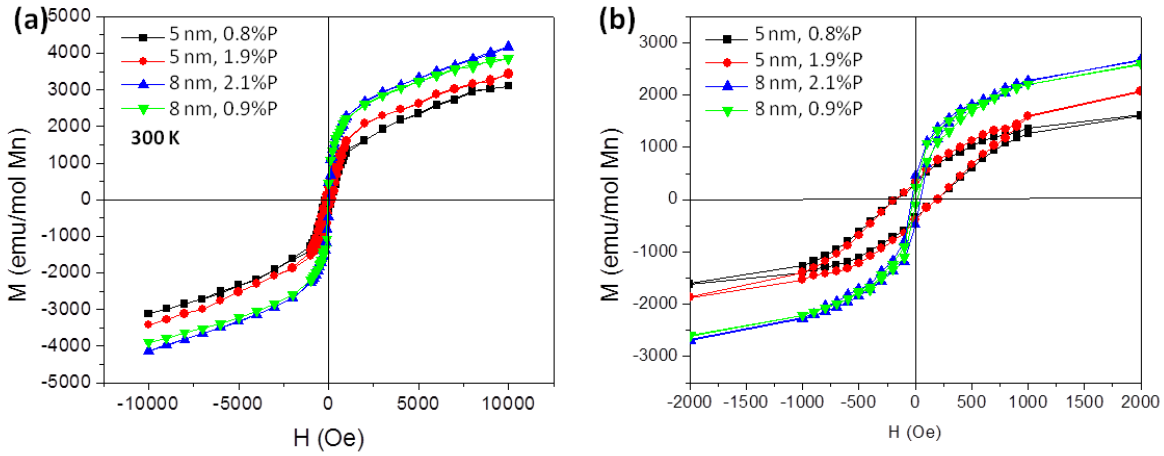

Figure 4.5 The compiled graphs of (a) field dependant molar magnetization and (b) expansion of hysteresis loop

4.5 Conclusions

In this part of the dissertation work, type-B MnAs nanoparticles adopting the β structure at room temperature have been synthesized by independently controlling size and %P. Nanoparticles of different P amounts with ca. 8 nm particle sizes were synthesized by a hot injection method followed by high temperature quenching of the reaction mixture at different reaction times. Smaller nanoparticles of ca. 5 nm with 0.8 % P were synthesized by increasing the 1- octadecene amount up to 16 mL and reaction time to 10 hours. TOP was used in place of TOPO with the expectation that it would enable the synthesis of heavily doped MnAs nanoparticles. However, TOP appears to have more of size controlling effect in addition to incorporating P, resulting in 5 nm particles with 1.9%P. This is surprising since MnP can be prepared under similar conditions using TOP as the P source. All of the samples exhibit ferromagnetic behavior and the magnetic and structural transitions appear to be related. All the

samples show an extensive temperature range of phase coexistence. The transformation of type-B MnAs nanoparticles from β to α on cooling is reversible upon warming, but occurs with significant hysteresis and an extensive region of phase coexistence. The hysteresis and phase-coexistence of nanoparticles is possibly due to heterogeneity of the nanoparticles in terms of P concentration, slight variation of sizes within one sample, surface properties and defects. The individual particles are likely to transform abruptly while the sample as a whole exhibit phase coexistence. The large coexistence range coupled to the thermal hysteresis results in temperature-dependent phase mixtures, making this material programmable.

CHAPTER 5 SYNTHESIS AND CHARACTERIZATION OF Fe-INCORPORATED DESCRETE TYPE-B MnAs NANOPARTICLES: EFFECT OF Fe-INCORPORATION ON MAGNETOSTRUCTURAL PROPERTIES

5.1. Introduction

As described in Section 1.8, manganese arsenide has a large magnetocaloric effect (MCE) associated with its first order phase transition. Anion doping with P creates internal chemical pressure, enabling tuning of the phase transition temperature in discrete MnAs nanoparticles as described in Chapter 3 and 4. Doping on the cation site is also expected to create internal chemical pressure enabling tuning of phase transition temperature. $Mn_{1-x}Fe_xAs$ phases are promising materials for magnetic refrigeration applications, based on studies in the bulk. $Mn_{1-x}Fe_xAs$ bulk compounds are reported to have colossal MCE at ambient pressure and the Fe content can be varied to tune the phase transition temperature.[117] In bulk, $Mn_{1-x}Fe_xAs$ materials were found to operate in the 285-310 K range, an important temperature range for room temperature applications, and a T_C decrease and a hysteresis increase with increasing Fe concentration has been reported.[117] Studies on Fe-incorporation in discrete MnAs nanostructures have not been reported, possibly due to challenges in fabricating transition metal arsenides as discrete nanostructures.

In nanomaterial synthesis, ion exchange has been a powerful tool to prepare new materials using existing phases as templates.[118] The short diffusion lengths and associated low activation energies for cation-exchange in nanomaterials has made cation exchange a go-to method for fabricating nanomaterials usually inaccessible by conventional synthetic methods. In the present work, conditions for Fe incorporation in MnAs are established and the consequence of incorporation on the magnetic and structural properties is probed.

5.2. Experimental section

All the chemicals used in the syntheses described in this chapter are listed in Chapter 2 (Section 2.1). The instruments and the methods used for characterization of as-prepared nanoparticles are also discussed in Chapter 2.

5.2.1 Synthesis of type-B MnAs nanoparticles

The experimental procedure for the synthesis and purification of type-B MnAs nanoparticles is the same as the procedure described in section 4.2.1. In brief, nanoparticles with 8 nm particle sizes were synthesized by a hot injection method followed by high temperature quenching of the reaction mixture at 603 K by cannulation into chloroform (maintained at 290 K) after 10 hours of reaction time. In this synthesis, a total of 0.5 mmol of manganese carbonyl dissolved in 8 mL of 1-octadecene is injected into a mixture of 4 g of TOPO and 1 mmol of triphenylarsine oxide in a Schlenk flask maintained at 573 K.

5.2.2 Incorporation of iron

The type-B MnAs nanoparticles synthesized as described in section 5.2.1 were re-dispersed in TOPO (2 g) in a Schlenk flask and heated at 373 K under vacuum for 15 minutes followed by purging with argon gas. Iron carbonyl (Mn:Fe 1:0.25) dissolved in 1 mL of 1-ODE was injected into the reaction mixture maintained at 373 K and the resulting nanoparticles were isolated after 15 minutes of reaction time by rapid cannulation into chloroform maintained at 290 K and purified as described in section 3.1.1.

5.2.3 Probing the mechanism of iron incorporation

Iron incorporation was carried out as described in Section 5.2.2, and approximately 0.2 mL aliquots were withdrawn from the reaction mixture at different reaction times. The first aliquot was withdrawn 15 minutes after iron incorporation and the second aliquot was isolated

after 90 minutes of reaction time. The nanoparticles were isolated into chloroform maintained at 290 K and purified as described in section 3.1.1.

5.2.4 Characterization

Particle size, morphology and size distribution were analyzed using micrographs imaged by TEM. The crystallite size and structure were determined by using the Scherrer formula and comparison of PXRD patterns to phases in the Powder Diffraction File (PDF) database (release 2000), respectively. ICP-MS and EDS were employed to determine the elemental composition. The temperature dependant structural changes were probed with temperature dependant PXRD. Magnetic measurements were collected using the PPMS instrument.

5.3. Results and discussion

5.3.1 Effect of iron-incorporation on morphology, composition and structure

In this part of the dissertation study, approximately 8 nm MnAs nanoparticles prepared as described in Section 4.2.1, were employed as a substrate for iron incorporation. Prior to Fe-doping, the elemental composition, structural and magnetic data of as prepared type-B MnAs nanoparticles were collected in order to compare the effect of Fe-incorporation on intrinsic properties. Table 5.1 summarizes the elemental composition obtained by ICP-MS for type-B MnAs nanoparticles before and after treatment with $Fe(CO)_5$.

Table 5.1 Comparison of elemental composition of type-B MnAs nanoparticles before and after treatment with Fe

	Mn%	As%	P%	Fe%
Untreated type-B MnAs nanoparticles	49.8 (±0.4)	49.4 (±0.6)	0.8 (±0.1)	0.0
Fe-treated type-B MnAs nanoparticle	47.4 (±0.2)	49.3 (±0.4)	0.7 (±0.2)	2.6 (±0.3)

Figure 5.1 (a) shows the TEM image of the initial type-B MnAs nanoparticles consisting of high contrast spherical core (MnAs, adventitiously P-doped) and a low contrast amorphous (Mn arsenate/arsenite) shell. The average crystallite size of the initial MnAs nanoparticles, calculated from PXRD data by Scherrer's equation, is 8.9 nm, which is in good agreement with the particle core size obtained by TEM (8.4 nm). The nanoparticles resulting from iron treatment (with $Fe(CO)_5$) appear to retain the same core shell structure and the particle size is unchanged.

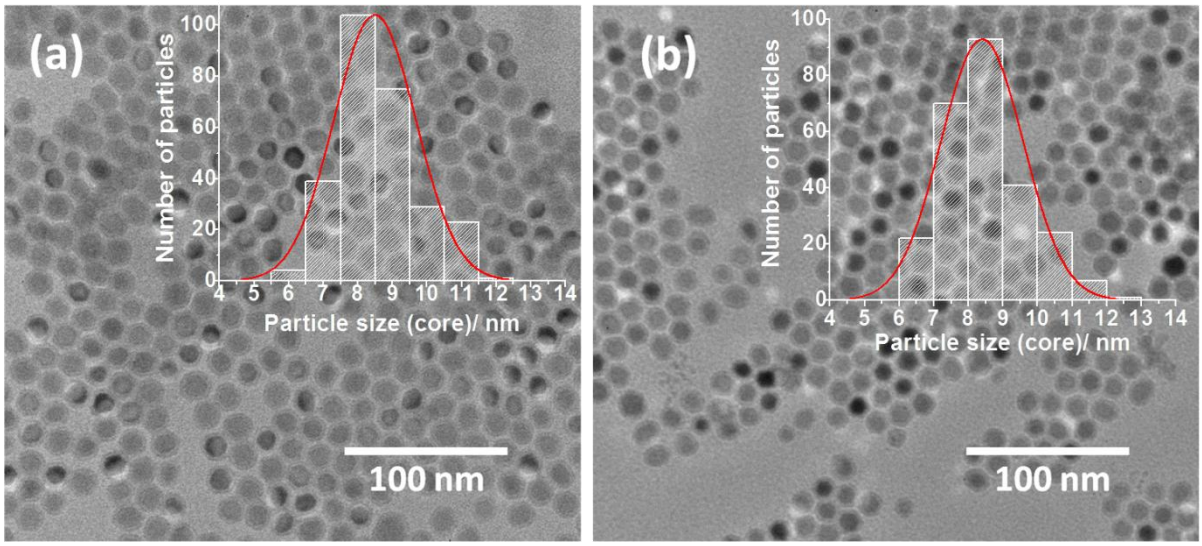

Figure 5.1 TEM images of (a) initial type-B MnAs nanoparticles and (b) 15 minutes iron-treated type-B MnAs nanoparticles. The insets show size distribution histogram.

The ICP-MS data suggests 2.6% Fe-incorporation after treatment with iron, while maintaining similar P concentrations. Intriguingly, Mn concentration has decreased after Fe-treatment, suggesting displacement of Mn. In order to evaluate the distribution of elements, an elemental map and elemental line profiles were obtained for the iron treated MnAs nanoparticles (Figure 5.2). The HAADF image clearly shows the core-shell structure of nanoparticles is intact after iron treatment. In the elemental map, Mn and As signals are very intense in both the crystalline core and the amorphous shell of the nanoparticles. The signals for P and Fe are faint relative to Mn and As, suggesting a lower concentration within the core and shell.

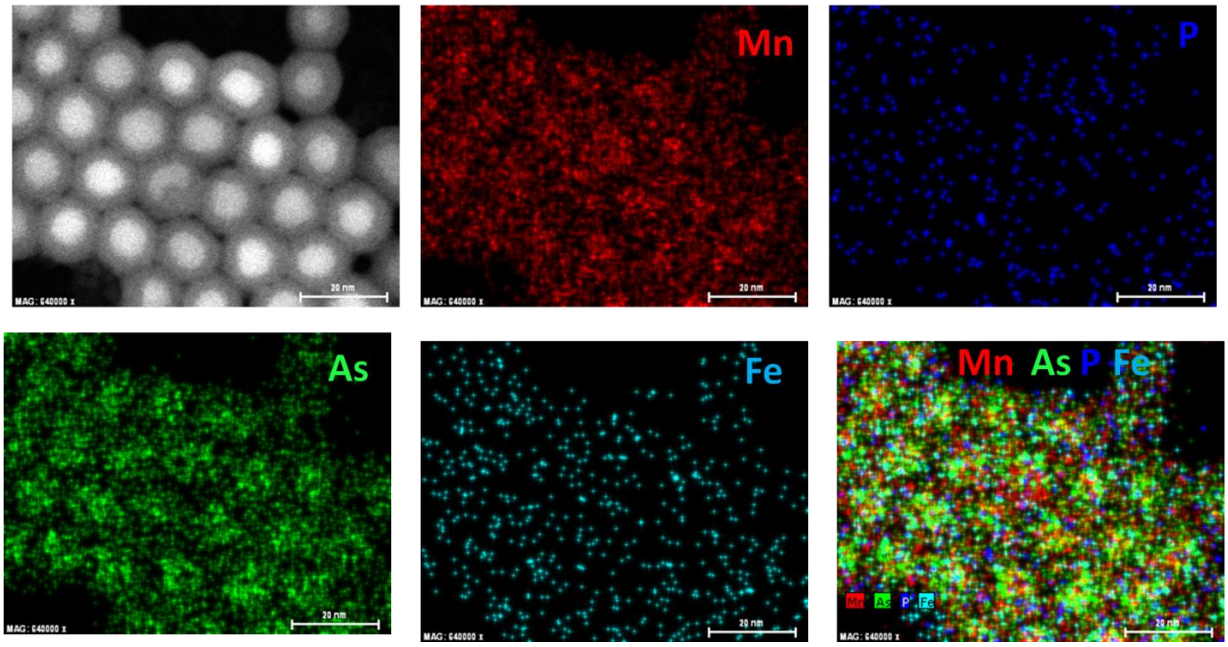

Figure 5.2 HAADF image and the elemental map of iron treated nanoparticles

In order to have a better understanding about the Fe-distribution, the elemental line profile analysis for several individual Fe treated MnAs nanoparticles has been performed and Figure 5.3 shows a representative elemental line scan for an Fe-treated nanoparticle along with that of an initial type-B MnAs nanoparticle. In the elemental line scan for the initial type-B MnAs nanoparticles, signals for Mn and As rise and fall together throughout core and shell and a trace amount of P is observed, whereas, in the iron incorporated nanoparticles, a trace amount of P and Fe is uniformly distributed throughout the core and the shell of the nanoparticle. Intriguingly, the distribution of Mn appears to be altered with the incorporation of iron. After Fe-treatment, there is more Mn in the shell compared to initial nanoparticles. The Mn displaced with Fe-treatment might result formation of a manganese oxide layer on the surface.

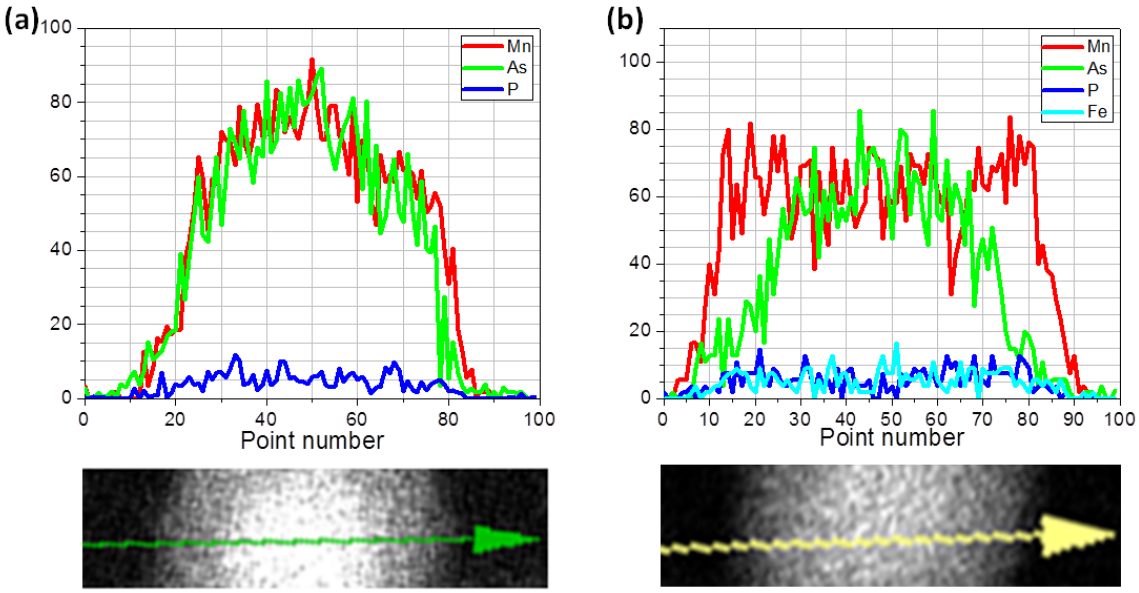

Figure 5.3 Elemental line scan of (a) initial type-B MnAs and (b) iron incorporated MnAs nanoparticle

Room temperature PXRD acquired in the range of 2θ = 20°-70° was used to collect structural and crystallite size information on initial and Fe-incorporated MnAs nanoparticles (Figure 5.4). Both the initial and Fe-incorporated MnAs nanoparticles are highly crystalline, as evidenced by the sharpness of the diffraction peaks, and MnAs can be indexed to the β-MnAs structure. However, the reflections for the Fe-treated MnAs nanoparticles are significantly shifted to higher 2θ (lower d-spacing), a surprising result considering the low (2.6%) Fe-incorporation. The average crystallite size of Fe-incorporated MnAs nanoparticles calculated by the Scherrer formula was found to be as same as initial MnAs nanoparticles (8.9 nm) suggesting that the crystallite size is unchanged upon Fe-incorporation.

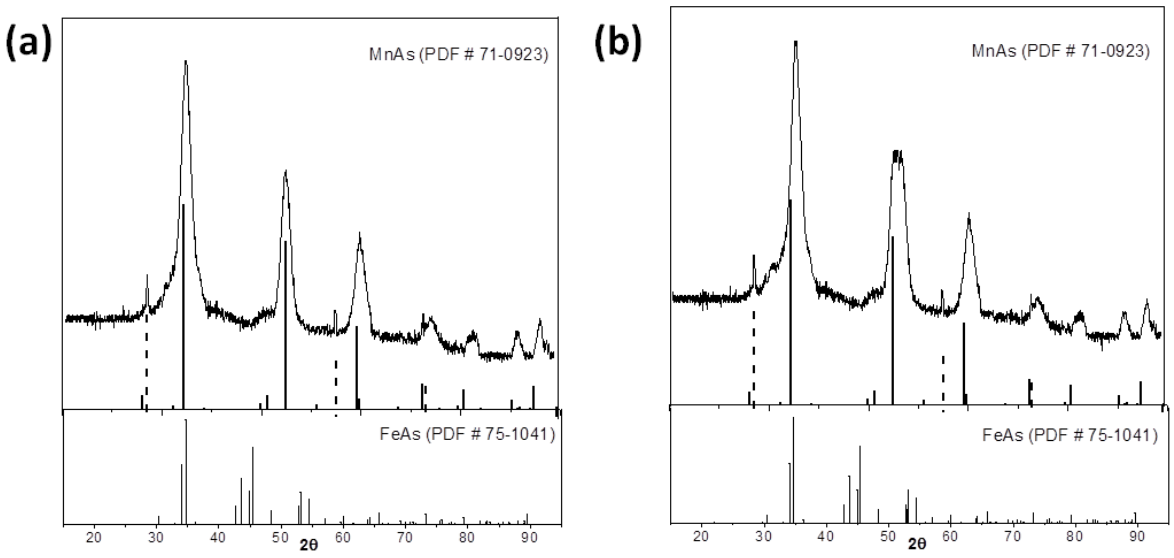

Figure 5.4 Room temperature PXRD pattern of (a) initial type-B MnAs and (b) iron doped MnAs nanoparticles. Solid lines are for MnAs (PDF# 71-0923) and dashed lines are for Si standard. (PDF#80-0018)

The lattice parameters of initial and Fe-treated MnAs nanoparticles were calculated by least square refinement relative to the internal silicon standard and are summarized in Table 5.2. It is evident that there is a 0.6% reduction of lattice parameters with respect to the untreated type-B MnAs nanoparticles, reflecting the shift observed in the PXRD pattern. Campos and coworkers studied the intrinsic properties of bulk iron-doped MnAs and reported a reduction of lattice parameters for the hexagonal NiAs-type structure (α-MnAs) and orthorhombic MnP-type structure (β-MnAs).[117]

Table 5.2 Lattice parameter and cell volume data of type-B MnAs nanoparticles before and after Fe-incorporation

Material	*a* (Å)	*b* (Å)	*c* (Å)	Volume (Å^3)
Initial type-B MnAs	5.7235(8)	3.6688(2)	6.3426(8)	133.18
Type-B MnAs after doping	5.7196(5)	3.6515(4)	6.3325(4)	132.26

5.3.2 Effect of iron incorporation on the structural transition in type-B MnAs nanoparticles

In order to probe the effect of iron incorporation on the structural transition, temperature dependant PXRD data were collected in the range $2\theta = 48^o$-51^o for type-B MnAs before and after iron incorporation. The data in Figure 5.5 show that the transformation of initial type-B MnAs and Fe-incorporated MnAs nanoparticles from β to α structure on cooling is reversible upon warming. The (110) reflection of α-MnAs and the (013) reflection of β-MnAs can be easily identified in the diffraction patterns of both samples. At room temperature, both the initial and the iron incorporated samples adopt exclusively the β-MnAs structure. The onset of the structural phase transition was determined using the computed relative quantities of each phase. Similar to the temperature dependant PXRD data shown in section 4.4.1, these data show a significant region of phase coexistence.

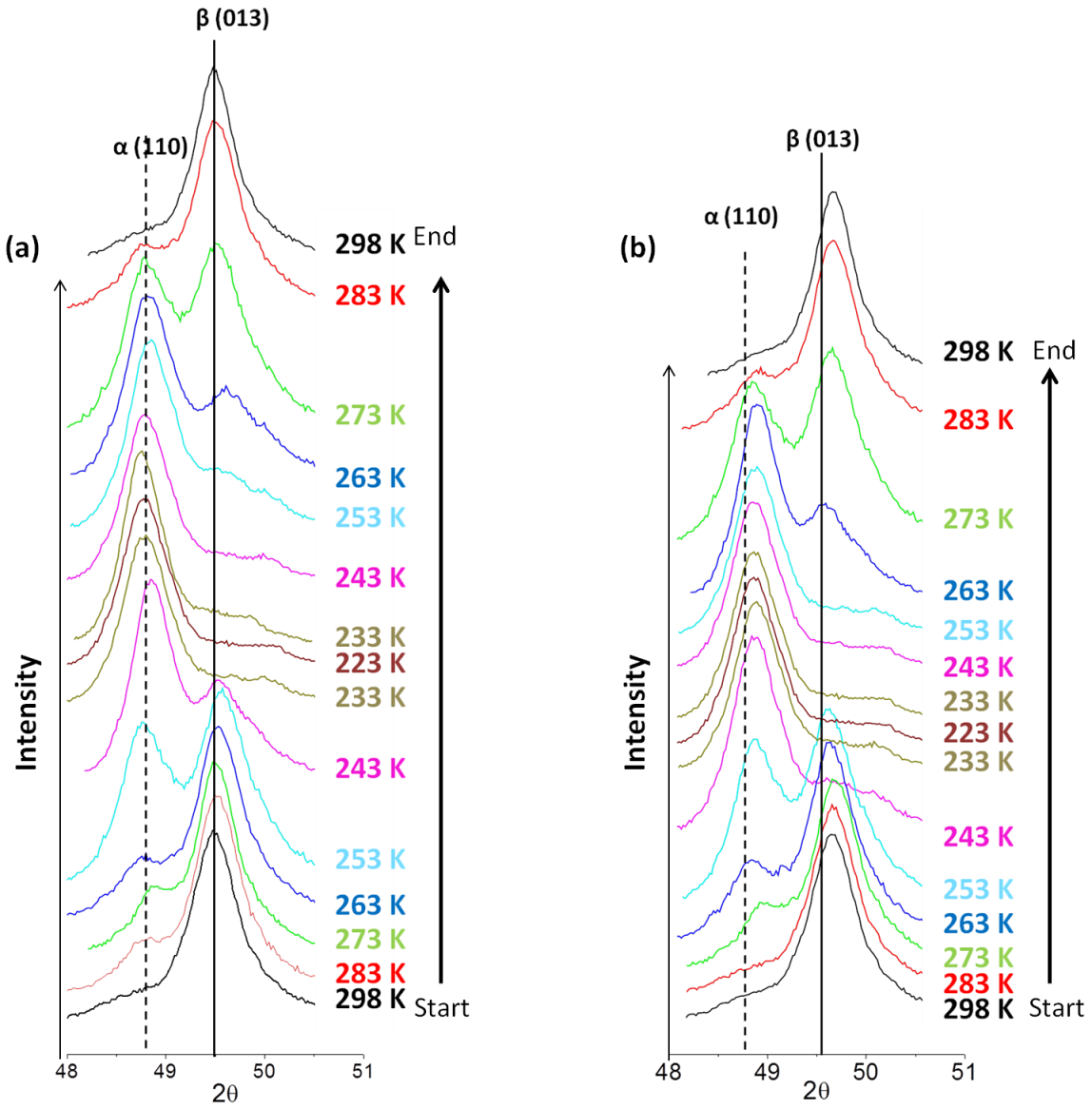

Figure 5.5 Temperature dependant PXRD of (a) initial MnAs and (b) Fe-incorporated MnAs nanoparticles

The structural transition from β to α in the untreated type-B MnAs sample initiates in the 298-283 K temperature range with 7.8% α-phase by 283 K (Appendix). The structural transition from β to α is complete by 223 K. Upon warming α-phase is observed by 283 K (Appendix) indicating a negligible structural hysteresis. After iron treatment, the transition was observed to occur in the 283-273 K temperature range with 6.9% α-phase at 273 K. Similar to initial MnAs

sample, Fe-treated sample also reach complete structural transition to the α-phase by 223 K. Upon warming, the Fe-treated sample show 30.7% α-phase at 273 K (Appendix), resulting approximately 10 K hysteresis. As P concentration of Fe-treaded sample is more or less similar to that of untreated type-B MnAs nanoparticles, the observed depression of onset of the β to α structural transition may be attributed to incorporation of iron. However, with respect to the short reaction time, it is difficult to rule out the possibility of inhomogeneity in surface properties and defects. The phase coexistence and hysteresis may be attributed to individual nanoparticles that are differently doped (either P or Fe) that undergo the structural transition at a temperature characteristic to them.

5.3.3 Effect of iron incorporation on the magnetic transition of type-B MnAs nanoparticles

The magnetic properties of initial and iron-treated type-B MnAs nanoparticles were acquired to probe the effect of doping on the magnetic phase transition and the correlation between structural and magnetic behavior. The magnetic data in Figure 5.6 (a) and (b) were first collected on cooling followed by heating. The temperature-dependant molar magnetization curves of both samples show a small magnetic susceptibility at the warmest end of the scans. As the samples are cooled down, all the samples show a distinct increase in magnetic susceptibility corresponding to a ferromagnetic transition with the Curie temperature, T_C, below room temperature. It is evident that the magnetic data reflects the structural transitions. The untreated type-B MnAs sample initiates a structural transition in the 298-283 K range on cooling and T_C is estimated to occur at 280 K on cooling. The iron incorporated sample shows the β to α structural transition at a slightly lower region, 283-273 K, and the magnetic transition occurs at 268 K on cooling. These data indicate a strong correlation between the structural and magnetic properties.

Similar to data shown in Section 4.4.2, hysteresis is observed upon warming in both samples. However, the iron doped sample show increased hysteresis, 17 K, compared to that in the untreated sample (5 K). Accordingly, the T_C on warming is the same for the two materials (285 K). Table 5.3 summarizes the magnetic data shown in Figure 5.6. Campos and co-workers synthesized a range of $Mn_{1-x}Fe_xAs$ (x = 0.003-0.0175) bulk materials and reported a drop of T_C (from ~295 to ~255 K on cooling), saturation magnetization (from ~10.8 to ~4.5 emu/kg) and an increase in thermal hysteresis (from ~15 to ~30 K) as x increases up to x = 0.0125.[117] They observed that $Mn_{1-x}Fe_xAs$ with x > 0.0125 shows an antiferromagnetic-like behavior. Similar to what Campos and coworkers reported, the iron incorporated samples under investigation show a lowering of Tc, saturation magnetization and an increase in hysteresis with introduction of iron. However, in the present study, the doped MnAs nanoparticles exhibit ferromagnetic behavior with x = 0.026 Fe. This may represent an inhomogeneous distribution of dopant, such that a portion of the sample has <1.25% Fe, with the consequent ferromagnetism dominating the antiferromagnetic contribution.

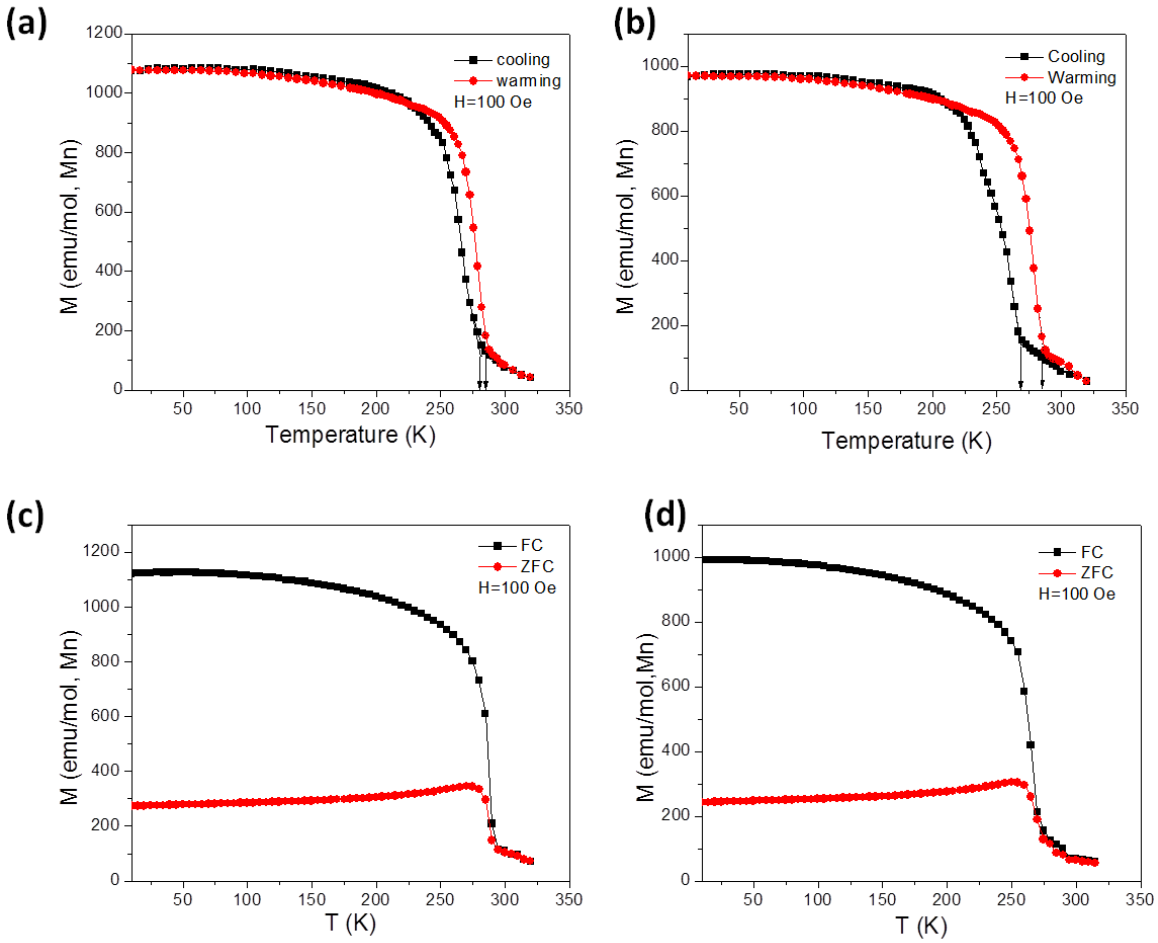

Figure 5.6 Temperature dependant molar magnetization data for (a) Initial and (b) Fe-treated type-B MnAs nanoparticles and ZFC-FC data for (c) initial and (d) Fe-treated type-B MnAs nanoparticles

The magnetic moment of both samples was calculated based on analysis of Mn content in the sample, assuming MnAs is the only contributor to the ferromagnetic moment. Thus, the slight decrease of magnetization (Table 5.2) in the iron treated sample may be attributed to slightly less Mn. As mentioned previously, the lattice parameter calculations show a 0.6% volume reduction in Fe-incorporated type-B MnAs nanoparticles, and the unit cell compression resulting from this internal chemical pressure may be the leading reason for the decreased T_C on cooling. The Zero-Field-Cooling (ZFC) and Field-Cooling (FC) data acquired under an external

magnetic field of 100 Oe indicate the blocking temperature is near T_C, 270 K for initial type-B MnAs and to 260 K in the Fe-treated sample. The high T_B for such small particle size is a reflection of the large uniaxial magnetic anisotropy inherent in MnAs.

The field dependant magnetization data (Figure 5.7) shows a small coercivity (150 Oe for untreated type-B MnAs and 275 Oe for Fe-treated type-BMnAs) for both samples at 300 K, above the blocking temperature, and it appears to increase after incorporation of iron. Coupling of a ferromagnetic component with an antiferromagnetic component in nanoparticles as core-shell structures may explain the presence of coercivity and its increase after Fe-incorporation (i.e. ferromagnetic MnAs with an antiferromagnetic arsenate/ite or oxide shell).[120] However, shifting of the hysteresis loop along the x-axis, which is common for core-shell ferro-antiferromagnetic particles, is not observed. Alternatively, the origin of this effect is not clear and may arise from a population of poorly doped or undoped particles with a higher T_C and corresponding blocking temperature.

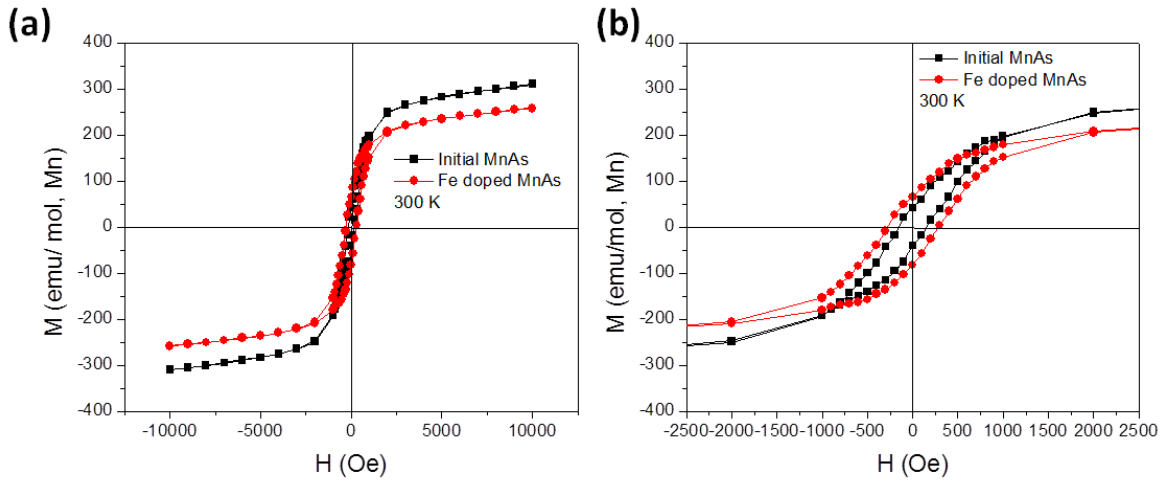

Figure 5.7 Graphs of (a) field dependant molar magnetization and (b) expansion of hysteresis loop for initial and Fe-treated MnAs nanoparticles

Table 5.3 Magnetic data of initial and Fe-incorporated type-B MnAs nanoparticles

	Initial type-B MnAs nanoparticles	Fe-treated type-B MnAsnanoparticles
T_C on cooling (K)	280	268
T_C on warming (K)	285	285
Magnetization at 50 K (emu/mol,Mn)	1080	970
Phase coexistence (K) on cooling	~50	~40
Blocking temperature (K)	270	260
Coercivity (Oe)	150	275

While iron treated type-B MnAs nanoparticles show changes in magneto-structural phase transition relative to the untreated system, it is not clear if iron doping alters the electronic structure of the material in addition to the volumetric effect on the unit cell. Campos and coworkers reported that the density of electronic states at the Fermi level is not altered in iron doped MnAs, suggesting that Fe does not play a significant role in the electronic structure in bulk $Mn_{1-x}Fe_xAs$. Thus, the effect of iron doping is expected to be largely due to the decreased volume of the unit cell.

5.3.4 Effect of time on Fe-incorporation

Approximately 0.2 mL aliquots were withdrawn from the reaction mixture at different reaction times. The first aliquot was withdrawn 15 minutes after the introduction of iron precursor, corresponding to the reaction time studied in the previous section, and the second aliquot after 90 minutes of reaction time. Nanoparticles isolated after 15 minutes of reaction time show the β-MnAs structure by room temperature PXRD and a core-shell morphology with a trace amount of Fe, similar to data shown in section 5.3.1. In contrast, the room temperature

PXRD pattern (Figure 5.8) of the aliquot isolated at 90 minutes of reaction time indicates the presence of a mixture of phases. The reflections can be indexed to FeAs and β-MnAs. The only possibility for FeAs formation is displacement of Mn from the cation lattice as additional As was not introduced in the doping process. The FeAs reflections were not observed in nanoparticles isolated at 15 minutes of reaction time indicating formation of FeAs phase with extended reaction time. In order to further evaluate the formation of the second phase, elemental line profiles and elemental maps of nanoparticles were acquired.

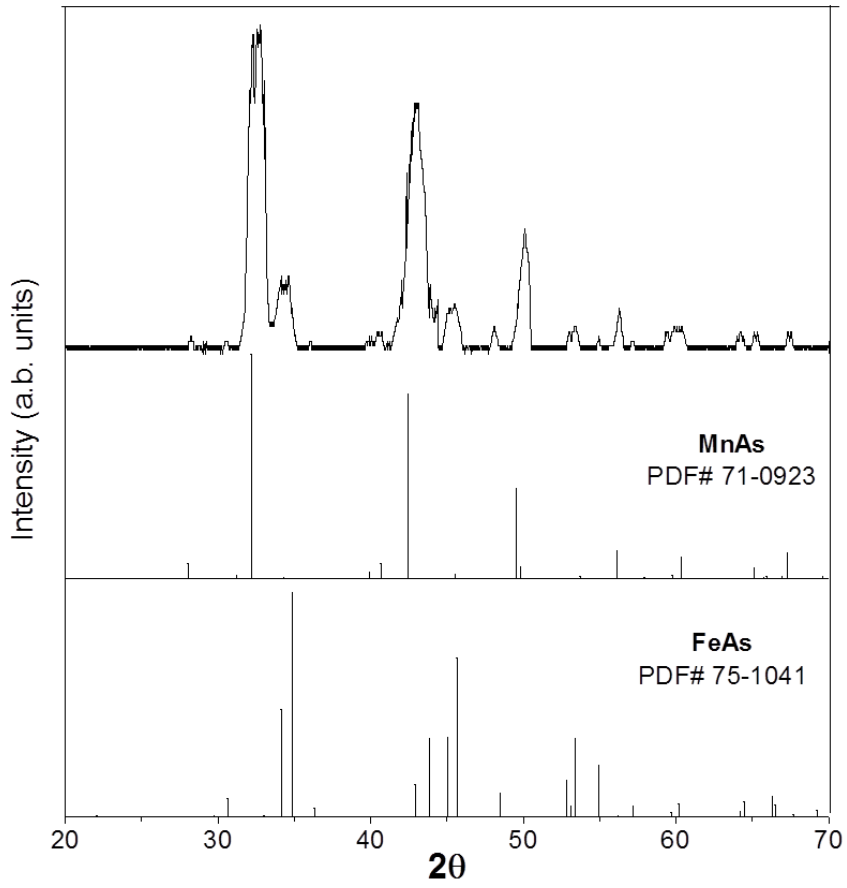

Figure 5.8 Room temperature PXRD pattern of the aliquot isolated at 90 minutes of reaction time with reference lines for MnAs and FeAs

The elemental line profile analysis of nanoparticles isolated after 90 minutes of reaction time reveals different distributions of Mn and Fe inside the core of the nanoparticles. Figure 5.9 shows a representative elemental line scan of a single core-shell nanoparticle. Iron appears to be concentrated in the core of the nanoparticle as the reaction time is increased to 90 minutes. The elemental line scans also indicates that the Mn signal intensity drops when the Fe intensity increases, suggesting displacement of Mn by Fe. Moreover, the Fe profile extends beyond that of the As, suggesting an ion oxide shell is likely forming. This may occur by Fe-exchange for Mn in the MnO_x shell formed as short reaction times (15 min) with $Fe(CO)_5$.[14]

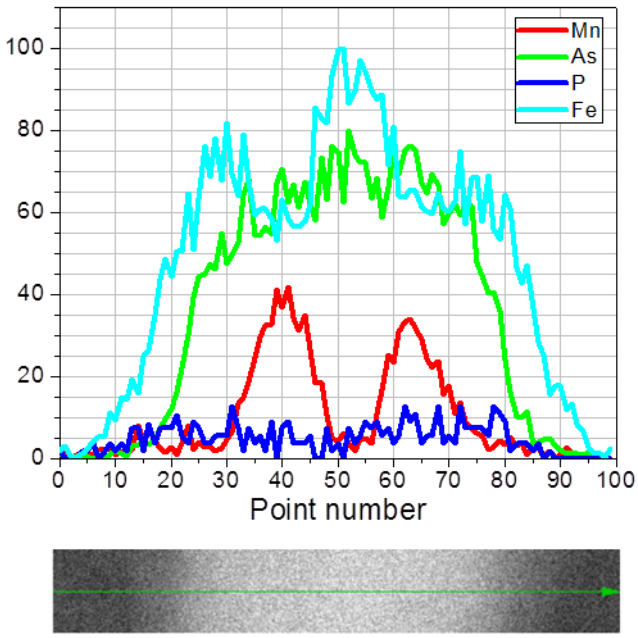

Figure 5.9 Elemental line scan of a single core-shell MnAs nanoparticle doped with iron

Figure 5.10 shows the HAADF image and elemental map of another representative Fe-doped nanoparticle. The element distribution in the elemental line profile is reflected in the element map of Fe-doped MnAs nanoparticles where lesser signals are observed for Mn in the center of core while signals for Fe appear more intense.

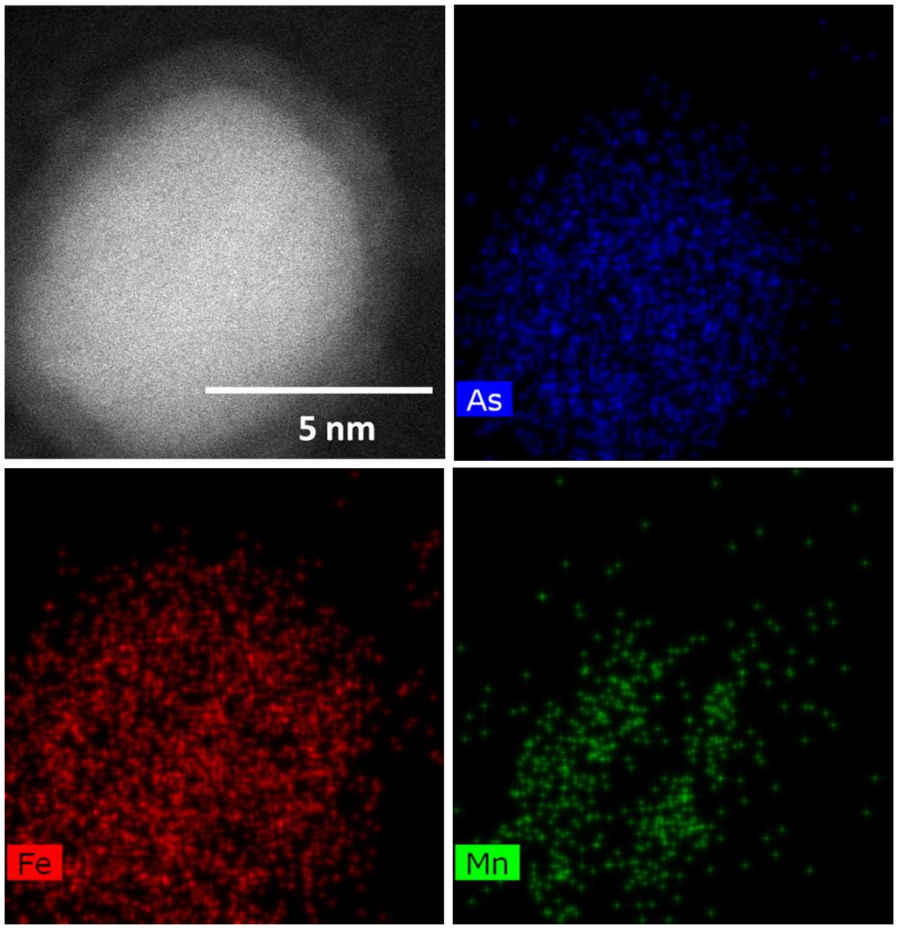

Figure 5.10 HAADF image and elemental map of iron doped core-shell structured nanoparticle

In addition to the core-shell structured nanoparticles, HAADF images show aggregated features that are Fe rich as observed by elemental line scanning (Figure 5.11) and elemental mapping (Figure 5.12). The aggregated features are Fe rich, Mn deficient and contain a moderate amount of As. Thus, it is possible to hypothesize that the aggregated features correspond to the FeAs peaks observed in the PXRD in Figure 5.8. The average elemental composition of the nanoparticles isolated at 90 minutes of reaction time shows Mn 43.7%, Fe 31.4%, As 24.0% and P 0.9% from ICP-MS analysis. These data indicate that more iron is incorporated into the solid phase as the reaction time is increased, displacing Mn and As.

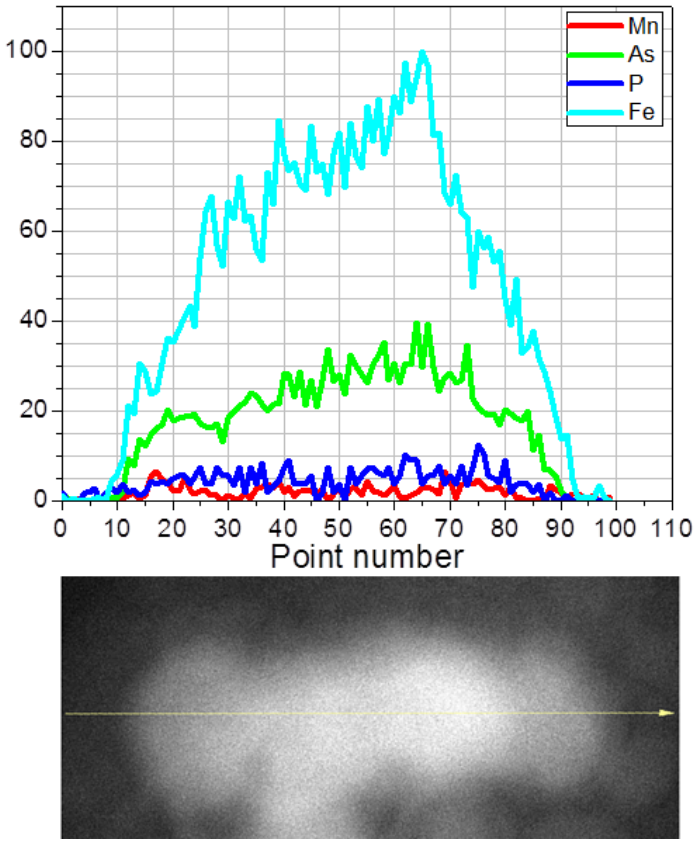

Figure 5.11 Elemental line scan of an aggregated feature isolated from an aliquot withdrawn after 90 minutes of reaction time

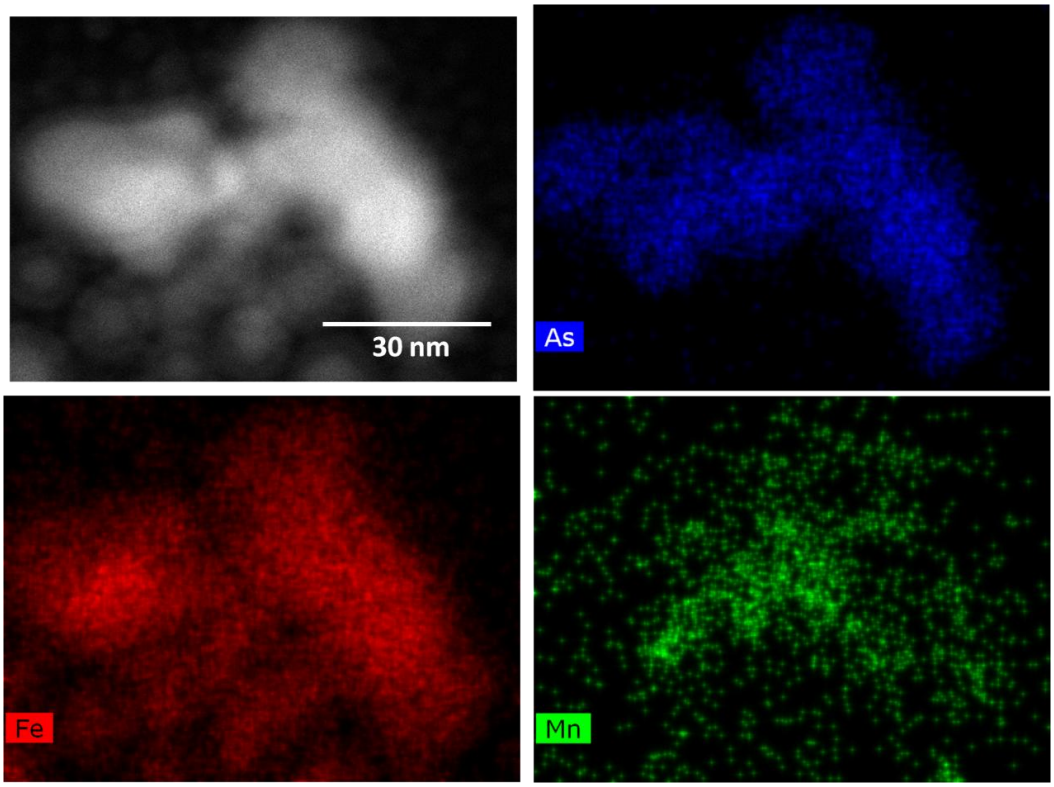

Figure 5.12 HAADF image and elemental map of an aggregated feature isolated from an aliquot withdrawn after 90 minutes of reaction time

The nanoparticles isolated from aliquot withdrawn after 90 minutes of reaction time indicate that complete displacement of Mn with Fe is feasible if synthetic parameters are properly exploited. In order to verify the complete displacement of Mn with Fe, the experimental procedure described in Section 5.2.2 was followed and iron incorporation was performed at 573 K. In contrast to previously mentioned iron doped samples, room temperature PXRD of MnAs incorporated with iron at higher temperatures (i.e. 573 K) show complete conversion into FeAs within 15 minutes of reaction time (Figure 5.13). As no additional arsenic was introduced, the formation of FeAs requires either dissolution of the initial MnAs nanoparticles, and subsequent nucleation and growth of FeAs, or an exchange process in which Mn is diplaced by Fe.

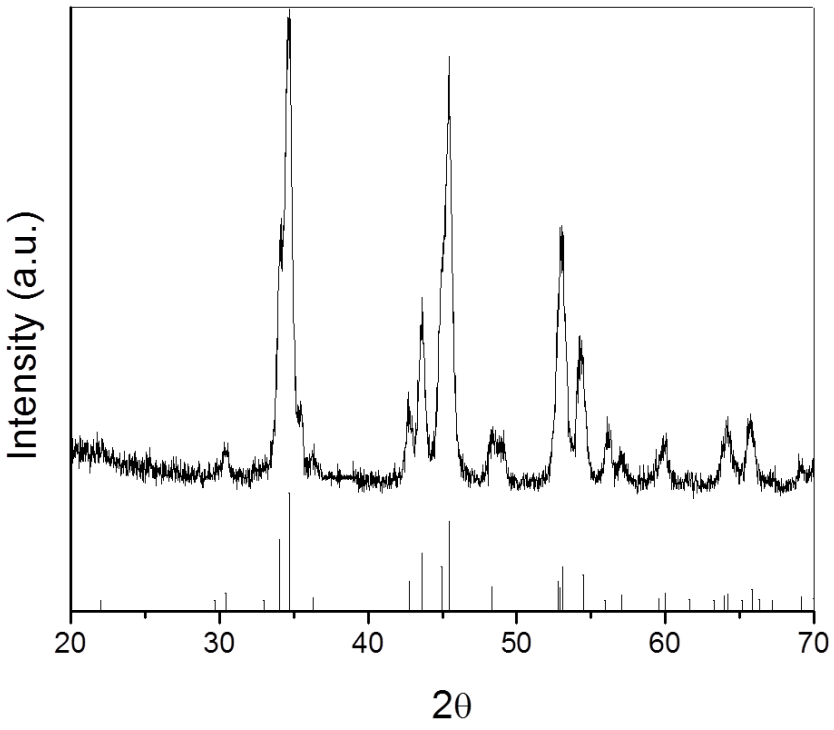

Figure 5.13 PXRD of a MnAs sample reacted with Fe and heated for 15 minutes at 573 K. Reference lines for FeAs (PDF # 75-1041)

Interestingly, direct synthesis of FeAs with the same iron precursor and coordinating solvents has been unsuccessful. Desai and co-workers reported a method for synthesis of superparamagnetic FeAs nanoparticles, where Fe precursor was injected to a mixture of As precursor and surfactants at 598 K to prepare superparamagnetic FeAs nanoparticles with an amorphous shell and crystalline FeAs core.[53] In contrast to the present work, the synthesis method reported by Desai *et al*. involves the use of triphenylarsine as the As precursor and hexadecylamine as a surfactant. In the present study, under the given reaction conditions, the final product isolated showed large aggregated features in addition to the core-shell structured nanoparticles. TEM images of MnAs samples incorporated with iron at high temperature show deformation of core and/or complete dissolution of core (Figure 5.14) suggesting FeAs formation essentially occurs at the expense of MnAs core as additional As is not introduced in doping

process. The hollow shells (Figure 5.14 (b) inset) may be attributed to residual oxides. In present work, high temperature iron incorporation is reminiscent of work reported by Beberwyck *et al.* where highly crystalline, nearly monodisperse GaAs and InAs by a 15 minute ion exchange process at 573 K.[121] However, in the present work, FeAs nanoparticles do not retain the same morphology or particle size, and the "empty" shells suggest a dissolution/re-precipitation and/or ripening process. The "empty" shells are unstable under the beam, thus prohibited elemental analysis by EDS.

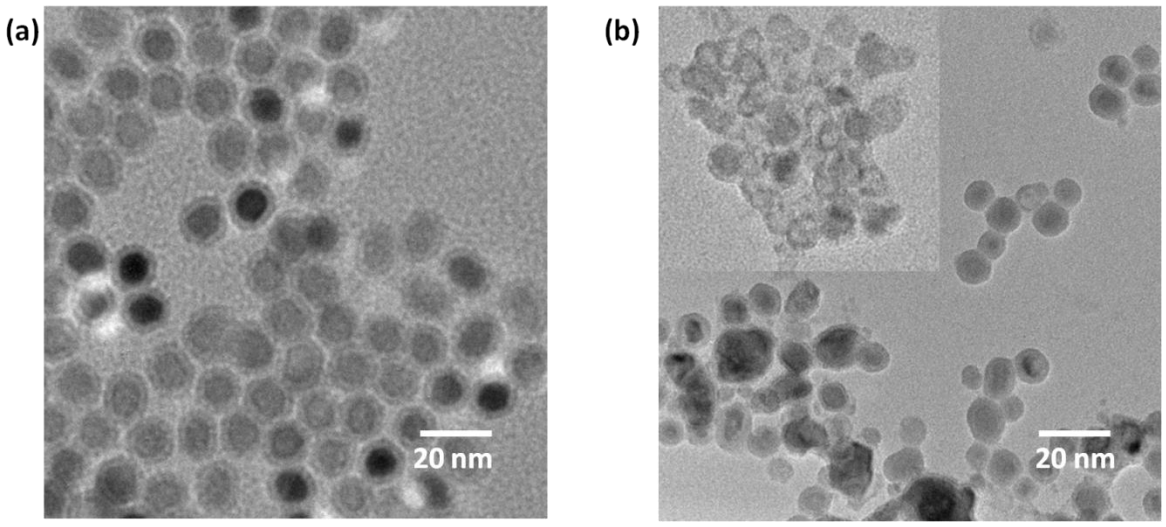

Figure 5.14 TEM images of type-B MnAs nanoparticles (a) before and (b) 15 minutes after Fe treatment at 573 K. The inset in (b) shows "empty" shells presumed to be an oxide remnant from etching of the arsenide core.

5.4. Conclusions

In this part of the dissertation work, type-B MnAs nanoparticles adopting the β-structure were treated with Fe (as $Fe(CO)_5$) and the extent of Fe-incorporation and consequences on structural and magnetic phase transitions are measured. The core-shell morphology, particle size and β-MnAs structure are retained upon incorporation of iron (ca. 2.6%) at a relatively lower temperature (373 K) with a short reaction time (15 minutes). The %P appears to remain

unchanged upon Fe-treatment. Iron incorporation into type-B MnAs nanoparticles appears to compress lattice parameters and lower the magneto-structural phase transition temperature upon cooling. The changes in intrinsic properties may be arising mainly due to the volumetric effect on the unit cell. However, electronic structure needs to be evaluated in order to investigate the effect of dopant incorporation. The elemental line profiles and maps indicate incorporation iron into the type-B MnAs nanoparticles. In order to further evaluate the elemental composition and distribution, atomic pair distribution function and X-ray photoelectron spectroscopy can be employed to understand 3D-information about the material and the surface nature, respectively. Extended reaction times appear to result in mixed phases (MnAs and FeAs), whereas high temperatures leads to complete conversion to FeAs. This study unveils a new path for synthesis of transition metal arsenide nanoparticles with increased compositional complexities by using accessible transition metal arsenide nanoparticles as a substrate.

CHAPTER 6 CONCLUSIONS AND PROSPECTUS

Due to the size, surface functionality and shape tunable properties, considerable attention has been drawn to research on nanomaterials. Transition metal pnictides are a large group of materials that have been studied in bulk. However, their nano counterparts are relatively unexplored, in part due to a lack of synthetic methods that enables independent control of size, morphology and composition. Arsenides are a fundamentally and technologically relevant group of materials that exhibit composition dependant properties including superconductivity, semi-conductivity and ferromagnetism. Despite the range of technological applications nanomaterials based on arsenides have to offer, the synthesis of arsenides as discrete nanoparticles remains relatively unexplored. Thus, the intrinsic size-dependant properties of arsenide nanomaterials are unknown.

Among transition metal arsenides, bulk MnAs has been extensively studied due to its potential application in magnetic refrigeration. While MnAs is a promising candidate for magnetic refrigeration, its cycling efficiency is adversely affected by high thermal hysteresis and the narrow temperature range over which MCE is maximized. Thus, studies on MnAs have focused on tuning the phase transition temperature and hysteresis. However, all the reported work on MnAs has been performed on bulk MnAs or nanostructures prepared on an epitaxial substrate. The Brock research group introduced a solution phase arrested precipitation (SPAP) method that allows synthesis of MnAs as discrete nanoparticles, providing an opportunity to study the intrinsic properties of MnAs on the nanoscale without epitaxial strain. SPAP has been found to be a versatile synthetic method for fabrication of transition metal pnictide nanoparticles as it allows fine tuning of morphology, composition and structure. Nanostructuring, combined with cation and anion doping, of MnAs can be used to tune the degree of hysteresis and phase

transition temperature, thereby enabling the properties to be refined for magnetic refrigeration applications.

Previous work performed on MnAs nanoparticles by the Brock group reported synthesis of type-A MnAs nanoparticles (adopting the α-structure at room temperature) by a slow heating method and type-B MnAs nanoparticles (adopting the β-structure at room temperature) by a rapid injection method. Type-A MnAs nanoparticles were reported to exhibit the magnetostructural phase transition at 312 K similar to bulk MnAs, but with a narrower hysteresis. Type-B MnAs nanoparticles were found to be doped with phosphorus, and as a consequence, the phase transition temperature shifts below room temperature. As the temperature of the first-order phase transition depends on the bond distances between Mn-Mn and Mn-As, it can be tuned by doping, which effectively creates an internal chemical pressure. However, the large size distribution and the inability to independently control size and dopants restricted the ability to probe the intrinsic properties as a function of particle size and dopants. This dissertation research is focused on understanding the growth mechanism of type-B MnAs nanoparticles, establishing synthetic methods to independently control size and dopant concentration (P and Fe doping), and probing the effect of particle size and doping on the magnetic and structural properties of MnAs nanoparticles.

This dissertation research successfully established a reproducible synthetic method enabling formation of type-B MnAs nanoparticles with fine control of size and composition. The SPAP method followed by rapid quenching of the reaction mixture allows isolation of type-B MnAs nanoparticles with a high degree of size uniformity. The evolution of solution-phase MnAs nanoparticle formation and incorporation of P has been quantitatively assessed. The dimensions of the nanoparticles were found to change with the monomer concentration change

and the particles become morphologically uniform as the temperature stabilizes. In type-B MnAs synthesis, high temperature isolation of nanoparticles is required to achieve narrow size distribution. Adventitious phosphorus incorporation from the solvent TOPO occurs during nucleation, and P is subsequently lost, likely due to self-purification. Thus, varying reaction time enables isolation of nanoparticles with different concentrations of P.

The second objective of this dissertation was to extend the knowledge obtained from the adventitious doping and mechanistic study to independently control MnAs nanoparticle size and P incorporation. Nanoparticles incorporating different P amounts with ca. 8 nm particle sizes were synthesized by SPAP followed by rapid quenching of the reaction mixture at different reaction times. Smaller nanoparticles of ca. 5 nm with 0.8 % P were synthesized by diluting the TOPO (P-source) with 1- octadecene and increasing the reaction time. Nanoparticles with ca. 5 nm core diameter and 1.9 %P were synthesized using TOP in place of less reactive TOPO. Regardless of size or %P, all the samples exhibit ferromagnetic behavior and the magnetic and structural transitions appear to be related. All the samples show hysteresis and an extensive temperature range of phase coexistence. The phase coexistence of nanoparticles can be attributed to heterogeneity of the nanoparticles in terms of %P, and possibly also due to variation of size, surface properties and defects. Thus the individual particles are likely to transform abruptly while the sample as a whole exhibit phase coexistence. The short reaction time may be giving rise to inhomogeneous distribution of the P-dopant in the MnAs nanoparticles.

As an alternate approach to P-doping on the anion lattice, this dissertation research also investigated doping with Fe on the cation lattice. $Mn_{1-x}Fe_xAs$ is reported to show a colossal magnetocaloric effect in the bulk. This dissertation established the conditions under which Fe can be incorporated to type-B MnAs while retaining the β-MnAs structure at room temperature.

The core-shell morphology and particle size can be retained upon incorporation of iron (by reaction of $(Fe(CO)_5$ and type-B MnAs nanoparticles) at a relatively low temperature (373 K) with a short reaction time (15 minutes). Iron incorporation appears to compress the lattice parameters and lower the magneto-structural phase transition temperature. Attempts to perform iron incorporation at longer times (90 minutes) or higher temperatures (573 K) result in FeAs formation, apparently by Mn excision, as a partial or exclusive final product, while direct synthesis of FeAs with same precursor and solvent system was unsuccessful. Accordingly, this study unveils a new synthetic path where inaccessible transition metal pnictides can be synthesized from accessible phases by exploiting ion-exchange routes.

During the type-B MnAs nanoparticle synthesis, approximately 20% Mn and As monomers remain in the solution, possibly as an unreactive by-product that is not isolated by our protocol, and the exact nature of this by-product remain unclear. Evaluation of the reaction mixture with fourier transform infrared spectroscopy and UV-visible spectroscopy after isolation of solids can facilitate to understand chemical nature of the remaining solution. The changes in intrinsic properties observed with doping on the cation and anion lattice may be arising mainly due to volumetric effect in unit cell. However, further studies are necessary to investigate the effect of doping and particle size on the electronic structure. This can be probed by evaluating the density of electronic states. The magnetic properties observed in doped MnAs (P or Fe) may also be in part due to inter-particle interactions. Thus, further studies involving systematic dilution with n-eicosane are necessary in order to probe the effect of inter-particle interactions. This dissertation study was limited to investigating the effect on magnetostructural properties upon Fe-doping on 8 nm sized nanoparticle. Further studies that enable independent control of size and %Fe are needed to understand the magnetic and structural behavior of Fe-doped MnAs.

Particularly, in the high Fe-concentration range where unexpected ferromagnetism is observed. In order to probe the effect of particle size, ca. 8 and 5 nm type-B MnAs nanoparticles can be used as substrates. Synthesis of type-B MnAs with high Fe-concentration range is possibly achievable by employing low temperatures (50-80 ^{o}C) and extended reaction times. Formation of FeAs upon high temperature reaction of $Fe(CO)_5$ with pre-made MnAs nanoparticles provides a synthetic route for future studies to investigate use of nanoparticles as templates for generating new discrete nanostructures that are difficult to prepare by direct synthesis (e.g. CoAs, NiAs).

APPENDIX RELATIVE QUANTITIES OF α-PHASE

Analysis title	% α
8 nm-2.1%P-Room Temperature-Start	0
8 nm-2.1%P-183 K Cooling	4.7 (±1.0)
8 nm-2.1%P-93 K	49.4 (±0.9)
8 nm-2.1%P-183 K Warming	4.7 (±1.1)
8 nm-0.9%P-Room Temperature-Start	0
8 nm-0.9%P-283 K-Cooling	8.2 (±0.1)
8 nm-0.9%P-283 K-Warming	15.0 (±1.5)
5 nm-1.9%P-Room Temperature-Start	0
5 nm-1.9%P-223 K-Cooling	16.5 (±0.8)
nm-1.9%P-223 K-Warming	62.9 (±1.7)
5 nm-0.9%P Room Temperature-Start	3.7 (±0.1)
5 nm-0.9%P 283 K-Cooling	5.9 (±0.9)
Initial MnAs-283 K cooling	13.8 (±0.9)
Initial MnAs-283 K warming	8.4 (±0.4)
Fe-treatedMnAs-273 K cooling	6.9 (±1.6)
Fe-treatedMnAs-273 K warming	30.7 (±0.7)

REFERENCES

1. M. L. Buil, M. A. Esteruelas, S. Niembro, M. Oliván, L. Orzechowski, C. Pelayo and A. Vallribera, *Organometallics*, 2010, **29**, 4375-4383.
2. P. A. Berseth, A. G. Harter, R. Zidan, A. Blomqvist, C. M. Araújo, R. H. Scheicher, R. Ahuja and P. Jena, *Nano Letters*, 2009, **9**, 1501-1505.
3. C. Guibert, V. Dupuis, V. Peyre and J. Fresnais, *The Journal of Physical Chemistry C*, 2015, **119**, 28148-28154.
4. R. Tietze, J. Zaloga, H. Unterweger, S. Lyer, R. P. Friedrich, C. Janko, M. Pöttler, S. Dürr and C. Alexiou, *Biochemical and Biophysical Research Communications*, 2015, **468**, 463-470.
5. K. L. Kelly, E. Coronado, L. L. Zhao and G. C. Schatz, *The Journal of Physical Chemistry B*, 2003, **107**, 668-677.
6. S. Prabhu and E. K. Poulose, *International Nano Letters*, 2012, **2**, 32.
7. F. Raimondi, G. G. Scherer, R. Kötz and A. Wokaun, *Angewandte Chemie International Edition*, 2005, **44**, 2190-2209.
8. F. Wang, R. Deng, J. Wang, Q. Wang, Y. Han, H. Zhu, X. Chen and X. Liu, *Nat Mater*, 2011, **10**, 968-973.
9. M. S. Mauter and M. Elimelech, *Environmental Science & Technology*, 2008, **42**, 5843-5859.
10. S. Carenco, D. Portehault, C. Boissière, N. Mézailles and C. Sanchez, *Chemical Reviews*, 2013, **113**, 7981-8065.
11. B. C. Sales, D. Mandrus and R. K. Williams, *Science*, 1996, **272**, 1325-1328.
12. J. Mira, F. Rivadulla, J. Rivas, A. Fondado, T. Guidi, R. Caciuffo, F. Carsughi, P. G. Radaelli and J. B Goodenough, *Phys. Rev. Lett.*, 2003, **90**, 097203.
13. O. Tegus, E. Bruck, K. H. J. Buschow and F. R. de Boer, *Nature*, 2002, **415**, 150-152.
14. K. Senevirathne, R. Tackett, P. R. Kharel, G. Lawes, K. Somaskandan and S. L. Brock, *ACS Nano*, 2009, **3**, 1129-1138.

15. S. Budak, C. C. Smith, B. Zheng, C. I. Muntele, R. L. Zimmerman and D. Ila, *MRS Proceedings*, 2006, **974**.

16. S. T. Oyama, *Journal of Catalysis*, 2003, **216**, 343-352.

17. M. S. Toprak, C. Stiewe, D. Platzek, S. Williams, L. Bertini, E. Müller, C. Gatti, Y. Zhang, M. Rowe and M. Muhammed, *Advanced Functional Materials*, 2004, **14**, 1189-1196.

18. H. Takahashi, K. Igawa, K. Arii, Y. Kamihara, M. Hirano and H. Hosono, *Nature*, 2008, **453**, 376-378.

19. M. Rotter, M. Tegel and D. Johrendt, *Physical Review Letters*, 2008, **101**, 107006.

20. S. Gama, A. A. Coelho, A. d. Campos, A. M. G. Carvalho, F. C. G. Gandra, P. J. v. Ranke and N. A. de Oliveira, *Phys. Rev. Lett.* , 2004, **93**, 237202.

21. D. Gammon, E. S. Snow, B. V. Shanabrook, D. S. Katzer and D. Park, *Science*, 1996, **273**, 87-90.

22. G. Reiss and A. Hutten, *Nat Mater*, 2005, **4**, 725-726.

23. Y.-M. Lin, K. C. Klavetter, P. R. Abel, N. C. Davy, J. L. Snider, A. Heller and C. B. Mullins, *Chemical communications*, 2012, **48**, 7268-7270.

24. M. Colilla, A. Baeza and M. Vallet-Regí, *The Sol-Gel Handbook-Synthesis, Characterization, and Applications: Synthesis, Characterization and Applications, 3-Volume Set*, 2015, 1309-1344.

25. E. Blanco, H. Shen and M. Ferrari, *Nature biotechnology*, 2015, **33**, 941-951.

26. M.-S. Kim, W.-J. Lee, K.-H. Cho, J.-P. Ahn and Y.-M. Sung, *ACS nano*, 2016, **10**, 7197-7207.

27. D. Mijatovic, J. C. T. Eijkel and A. van den Berg, *Lab on a Chip*, 2005, **5**, 492-500.

28. Y. Yang, S. Matsubara, L. Xiong, T. Hayakawa and M. Nogami, *The Journal of Physical Chemistry C*, 2007, **111**, 9095-9104.

29. C.-C. Chen, C.-Y. Chao and Z.-H. Lang, *Chemistry of materials*, 2000, **12**, 1516-1518.

30. N. B. Pawar, V. V. Kondalkar, V. B. Ghanwat, P. B. Patil and P. N. Bhosale, *Advanced Science Letters*, 2016, **22**, 915-920.

31. N. K. Sun, F. Liu, Y. B. Gao, Z. Q. Cai, B. S. Du, S. N. Xu and P. Z. Si, *Appl. Phys. Lett.*, 2012, **100**, 112407.

32. M. T. Swihart, *Current Opinion in Colloid & Interface Science*, 2003, **8**, 127-133.

33. A. K. Das, C. Pampuch, A. Ney, T. Hesjedal, L. Däweritz, R. Koch and K. H. Ploog, *Physical Review Letters*, 2003, **91**, 087203.

34. N. Koguchi and K. Ishige, *Japanese journal of applied physics*, 1993, **32**, 2052.

35. B. Jenichen, Y. Takagaki, K. Ploog, N. Darowski, R. Feyerherm and I. Zizak, *Applied physics letters*, 2006, **89**, 051915.

36. J. J. Lee, M. Y. Kim, Y. Cui, J. H. Song, A. J. Freeman and J. B. Ketterson, *Journal of Superconductivity*, 2005, **18**, 75-78.

37. A. Fontcuberta i Morral, C. Colombo, G. Abstreiter, J. Arbiol and J. R. Morante, *Applied Physics Letters*, 2008, **92**, 063112.

38. L. Seravalli, P. Frigeri, G. Trevisi and S. Franchi, *Applied Physics Letters*, 2008, **92**, 213104.

39. Y. Qian, *Advanced Materials*, 1999, **11**, 1101-1102.

40. Y. Xie, H. L. Su, X. F. Qian, X. M. Liu and Y. T. Qian, *Journal of Solid State Chemistry*, 2000, **149**, 88-91.

41. F. M. Davidson, A. D. Schricker, R. J. Wiacek and B. A. Korgel, *Advanced Materials*, 2004, **16**, 646-649.

42. X. Yi, L. Jun, Y. Ping, J. Xuchuan and Q. Yitai, *Chemistry Letters*, 2000, **29**, 114-115.

43. T. Onoki, *Porous Apatite Coating on Various Titanium Metallic Materials via Low Temperature Processing*, 2011.

44. A. Hatzor and P. S. Weiss, *Science*, 2001, **291**, 1019-1020.

45. A. E. Henkes, Y. Vasquez and R. E. Schaak, *Journal of the American Chemical Society*, 2007, **129**, 1896-1897.

46. C. Burda, X. Chen, R. Narayanan and M. A. El-Sayed, *Chemical Reviews*, 2005, **105**, 1025-1102.

47. S. C. Perera, G. Tsoi, L. E. Wenger and S. L. Brock, *Journal of the American Chemical Society*, 2003, **125**, 13960-13961.

48. E. Muthuswamy and S. L. Brock, *Chemical Communications*, 2011, **47**, 12334-12336.

49. M. A. Hettiarachchi, E. Abdelhamid, B. Nadgorny and S. L. Brock, *Journal of Materials Chemistry C*, 2016, **4**, 6790-6797.

50. C. W. Burrows, A. Dobbie, M. Myronov, T. P. A. Hase, S. B. Wilkins, M. Walker, J. J. Mudd, I. Maskery, M. R. Lees, C. F. McConville, D. R. Leadley and G. R. Bell, *Crystal Growth & Design*, 2013, **13**, 4923-4929.

51. F. Ishikawa, K. Koyama, K. Watanabe and H. F. Wada, *Jpn. J. Appl. Phys.* , 2003, 918-920.

52. V. I. Klimov, in *Semiconductor and Metal nanocrystals: Synthesis and Electronic and Optical Properties*, Marcel Dekker, 2004, vol. 87, ch. New York, N. Y., pp. 484-pp.

53. P. Desai, K. Song, J. Koza, A. Pariti and M. Nath, *Chem. Mater.*, 2013, **25**, 1510-1518.

54. N. G. Bastús, J. Comenge and V. Puntes, *Langmuir*, 2011, **27**, 11098-11105.

55. D. Ferreira, F. Silva, L. Viol, M. Schiavon, P. Licinio, M. Valadares, L. Cury, J. Alves, M. l. Caldas and N. Studart, 2010.

56. Y. Yin and A. P. Alivisatos, *Nature*, 2005, **437**, 664-670.

57. F. Wang, Y. Han, C. S. Lim, Y. Lu, J. Wang, J. Xu, H. Chen, C. Zhang, M. Hong and X. Liu, *Nature*, 2010, **463**, 1061-1065.

58. L. R. Bradshaw, J. W. May, J. L. Dempsey, X. Li and D. R. Gamelin, *Physical Review B*, 2014, **89**, 115312.

59. J. Yang, R. Fainblat, S. G. Kwon, F. Muckel, J. H. Yu, H. Terlinden, B. H. Kim, D. Iavarone, M. K. Choi, I. Y. Kim, I. Park, H.-K. Hong, J. Lee, J. S. Son, Z. Lee, K. Kang, S.-J. Hwang, G. Bacher and T. Hyeon, *Journal of the American Chemical Society*, 2015, **137**, 12776-12779.

60. H. Guo, X. Song, Z. Zhuo, J. Hu, T. Liu, Y. Duan, J. Zheng, Z. Chen, W. Yang, K. Amine and F. Pan, *Nano Letters*, 2016, **16**, 601-608.

61. G. M. Dalpian and J. R. Chelikowsky, *Physical Review Letters*, 2006, **96**, 226802.

62. M.-H. Du, S. C. Erwin and A. L. Efros, *Nano Letters*, 2008, **8**, 2878-2882.

63. Y. Zhang, R. Regmi, Y. Liu, G. Lawes and S. L. Brock, *ACS Nano*, 2014, **8**, 6814-6821.

64. V. A. Vlaskin, C. J. Barrows, C. S. Erickson and D. R. Gamelin, *Journal of the American Chemical Society*, 2013, **135**, 14380-14389.

65. A. Sahu, M. S. Kang, A. Kompch, C. Notthoff, A. W. Wills, D. Deng, M. Winterer, C. D. Frisbie and D. J. Norris, *Nano Letters*, 2012, **12**, 2587-2594.

66. H. Meyers and H. Myers, *Introductory solid state physics*, CRC press, 1997.

67. Y.-w. Jun, J.-w. Seo and J. Cheon, *Accounts of Chemical Research*, 2008, **41**, 179-189.

68. C. W. Jung, J. M. Rogers and E. V. Groman, *Journal of magnetism and magnetic materials*, 1999, **194**, 210-216.

69. J.-B. Peng, X.-J. Kong, Q.-C. Zhang, M. Orendáč, J. Prokleška, Y.-P. Ren, L.-S. Long, Z. Zheng and L.-S. Zheng, *Journal of the American Chemical Society*, 2014, **136**, 17938-17941.

70. A. A. Wagh, K. Suresh, P. A. Kumar and S. Elizabeth, *Journal of Physics D: Applied Physics*, 2015, **48**, 135001.

71. J. Romero Gómez, R. Ferreiro Garcia, A. De Miguel Catoira and M. Romero Gómez, *Renewable and Sustainable Energy Reviews*, 2013, **17**, 74-82.

72. K. A. GschneidnerJr, V. Pecharsky and A. Tsokol, *Reports on Progress in Physics*, 2005, **68**, 1479.

73. J. D. Zou, H. Wada, B. G. Shen, J. R. Sun and W. Li, *Europhys. Lett.*, 2008, **81**, 47002.

74. E. Yüzüak, G. Durak, I. Dincer and Y. Elerman, *J. Alloy Comp.*, 2012, **541**, 256-262.

75. X. Tan, C. Ping, C. M. Thompson and M. Shatruk, *J. Am. Chem. Soc.*, 2013, **135**, 9553-9557.

76. H. Wada and Y. Tanabe, *Appl. Phys. Lett.*, 2001, **79**, 3302-3304.

77. I. Rungger and S. Sanvito, *Phys. Rev. B* 2006, 024429.

78. P. Tian, Y. Zhang, K. Senevirathne, S. L. Brock, A. Dixit, G. Lawes and S. J. L. Billinge, *ACS Nano*, 2011, **5**, 2970-2978.

79. J. B. Goodenough and J. A. Kafalas, *Physical Review*, 1967, **157**, 389-395.

80. M. Ramsteiner, H. Y. Hao, A. Kawaharazuka, H. J. Zhu, M. Kästner, R. Hey, L. Däweritz, H. T. Grahn and K. H. Ploog, *Physical Review B*, 2002, **66**, 081304.

81. Y. Takagaki, C. Herrmann, E. Wiebicke, J. Herfort, L. Däweritz and K. H. Ploog, *Applied Physics Letters*, 2006, **88**, 032504.

82. D. G. Ramlan, S. J. May, J.-G. Zheng, J. E. Allen, B. W. Wessels and L. J. Lauhon, *Nano Letters*, 2006, **6**, 50-54.

83. N. K. Sun, W. B. Cui, D. Li, D. Y. Geng, F. Yang and Z. D. Zhang, *Applied Physics Letters*, 2008, **92**, 072504.

84. A. F. Roger, R. , *Mater. Res. Bull*, 1968, 253-264.

85. M. Balli, D. Fruchart, D. Gignoux and R. Zach, *Applied Physics Letters*, 2009, **95**, 072509.

86. K. Shimomura, P. Bakule, F. L. Pratt, K. Ishida, K. Ohishi, I. Watanabe, Y. Matsuda, K. Nagamine, E. Torikai and K. Nishiyama, *Physics Procedia*, 2012, **30**, 224-226.

87. C. Chu, F. Chen, M. Gooch, A. Guloy, B. Lorenz, B. Lv, K. Sasmal, Z. Tang, J. Tapp and Y. Xue, *Physica C: Superconductivity*, 2009, **469**, 326-331.

88. J. Kim, T. Blasius, E. Kim and G. Stewart, *Journal of Physics: Condensed Matter*, 2009, **21**, 342201.

89. N. Sun, S. Xu, D. Li and Z. Zhang, *Phys. stat. solidi (a)*, 2011, **208**, 1950-1952.

90. F. Wang, R. Tang, J. L. F. Kao, S. D. Dingman and W. E. Buhro, *J. Am. Chem. Soc.*, 2009, **131**, 4983-4994.

91. B. D. Cullity and S. R. Stock, *Elements of x-ray diffraction*, Prentice Hall, Upper Saddle River, NJ, 2001.

92. I. P. Parkin and I. P. Parkin, *Applied organometallic chemistry*, **14**, 227-228.

93. L. Smart and E. Moore, *Solid state chemistry : an introduction*, Chapman & Hall, London, 1995.

94. A. L. Patterson, *Physical Review*, 1939, **56**, 978-982.

95. *Materials Characterization*, 1995, **34**, 289.

96. R. F. Egerton, *Physical principles of electron microscopy: an introduction to TEM, SEM, and AEM*, Springer Science & Business Media, 2006.

97. P. J. Goodhew, F. J. Humphreys and R. Beanland, *Electron microscopy and analysis*, Taylor & Francis, London; New York, 2001.

98. P. Hawkes, *Journal of Materials Science*, 2017, **52**, 2989-2994.

99. A. Montaser, *Inductively coupled plasma mass spectrometry*, J. Wiley, New York, 1998.

100. C. Muirheud, *Advanced Materials*, 1992, **4**, 527-527.

101. N. Sun, S. Xu, D. Li and Z. Zhang, *physica status solidi (a)*, 2011, **208**, 1950-1952.

102. P. S. Shah, M. B. Sigman, C. A. Stowell, K. T. Lim, K. P. Johnston and B. A. Korgel, *Advanced Materials*, 2003, **15**, 971-974.

103. G. Fischer and W. Pearson, *Canadian Journal of Physics*, 1958, **36**, 1010-1016.

104. T. Hesjedal and T. Phung, *Applied Physics Letters*, 2010, **96**, 072501.

105. S. C. Erwin, L. Zu, M. I. Haftel, A. L., A. L. Efros, T. A. Kennedy and D. J. Norris, *Nature*, 2005, **436**, 91-94.

106. D. J. Norris, N. Yao, F. T. Charnock and T. A. Kennedy, *Nano Lett.*, 2001, **1**, 3-7.

107. X. Peng, J. Wickham and A. P. Alivisatos, *Journal of the American Chemical Society*, 1998, **120**, 5343-5344.

108. X. Peng, *Advanced Materials*, 2003, **15**, 459-463.

109. D. C. Gary, M. W. Terban, S. J. L. Billinge and B. M. Cossairt, *Chemistry of Materials*, 2015, **27**, 1432-1441.

110. R. Xie, Z. Li and X. Peng, *Journal of the American Chemical Society*, 2009, **131**, 15457-15466.

111. J. W. Mullin, *Crystallization*, Butterworth-Heinemann, Oxford; Boston, 2001.

112. T. Ishizaki, K. Yatsugi and K. Akedo, *Nanomaterials*, 2016, **6**, 172.

113. A. Zieba, K. Seite, A. Kjekshus and A. Andresen, *Acta Chem. Scand. A*, 1978, **32**.

114. H. Fjellvåg, A. F. Andresen and K. Bärner, *Journal of Magnetism and Magnetic Materials*, 1984, **46**, 29-39.

115. V. M. Kaganer, B. Jenichen, F. Schippan, W. Braun, L. Däweritz and K. H. Ploog, *Physical Review Letters*, 2000, **85**, 341-344.

116. L. B. Steren, J. Milano, V. Garcia, M. Marangolo, M. Eddrief and V. H. Etgens, *Physical Review B*, 2006, **74**, 144402.

117. A. de Campos, D. L. Rocco, A. M. G. Carvalho, L. Caron, A. A. Coelho, S. Gama, L. M. da Silva, F. C. G. Gandra, A. O. dos Santos, L. P. Cardoso, P. J. von Ranke and N. A. de Oliveira, *Nat Mater*, 2006, **5**, 802-804.

118. J. B. Rivest and P. K. Jain, *Chemical Society Reviews*, 2013, **42**, 89-96.

119. N. Menyuk, J. A. Kafalas, K. Dwight and J. B. Goodenough, *Physical Review*, 1969, **177**, 942-951.

120. J. Stöhr and H. C. Siegmann, *Magnetism : from fundamentals to nanoscale dynamics*, Springer, Berlin; [London], 2006.

121. B. J. Beberwyck and A. P. Alivisatos, *Journal of the American Chemical Society*, 2012, **134**, 19977-19980.

ABSTRACT

ELUCIDATION OF THE CATION AND THE ANION DOPING MECHANISM OF NANOPARTICULATE MANGANESE ARSENIDE: EFFECT OF DOPING ON THE MAGNETOSTRUCTURAL PROPERTIES

by

ROSHINI PIMMACHCHARIGE

May 2017

Advisor: Dr. Stephanie L. Brock

Major: Chemistry

Degree: Doctor of Philosophy

The evolution of MnAs nanoparticles in solution-phase synthesis and incorporation of P has been quantitatively assessed and the knowledge obtained from adventitious doping is extended to independently control nanoparticle size and P incorporation in order to understand the roles of size and dopant concentration on the magnetostructural properties. During the solution-phase synthesis, the dimensions of the nanoparticles change simultaneously with the monomer concentration in the bulk solution and the particles become morphologically uniform when the temperature stabilizes. The temperature at which the nanoparticles were isolated controls the particle size and polydispersity. High temperature isolation of nanoparticles is required to achieve narrow polydispersity and ultimately leads to a highly reproducible product. Adventitious phosphorus incorporation from the solvent TOPO occurs during nucleation, and P is subsequently lost, likely due to self-purification.

The reaction conditions for synthesis of nanoparticles of similar sizes with different P concentrations and different particle sizes with similar P concentrations were established and the effect on magnetic and structural properties was evaluated. Temperature-dependent XRD studies and magnetic measurements suggest that the transformation from β to α structure upon cooling is

reversible, but occur with hysteresis. As a consequence of P-doping, the phase transition temperature has shifted below room temperature and a large region of phase co-existence is observed. The magnetic and structural properties appear to be correlated.

The conditions for Fe-doping on type-B MnAs nanoparticles are established and the consequence on magnetic and structural properties is probed. The core-shell morphology, particle size and β-MnAs structure are retained upon incorporation of iron at relatively lower temperature (100 ^{o}C) with a short reaction time (15 minutes). Iron incorporation appears to compress lattice parameters and lower the magneto-structural phase transition temperature.

Overall, the changes in intrinsic properties observed with doping on the cation and anion lattice may be arising mainly due to volumetric effect in unit cell. This dissertation research reveals synthetic pathways to produce inaccessible phases from accessible phases by exploiting ion-exchange routes and direct syntheses.

AUTOBIOGRAPHICAL STATEMENT

ROSHINI PIMMACHCHARIGE

Education

- 2010-2017 Ph.D. Inorganic Chemistry, Wayne State University, Detroit, MI

  Dissertation: Elucidation of the cation and anion doping mechanism of nanoparticulate manganese arsenide: Effect of doping on the magnetostructural properties

  Advisor: Prof. Stephanie L. Brock
- 2004-2008 B.S. (honors) in Chemistry, University of Kelaniya, Sri Lanka

Research and Work Experience

- 2010-2017 Graduate Teaching/Research assistant, Department of Chemistry, Wayne State University, Detroit, MI
- 2015-2016 Explainer/Facilitator, Michigan Science Center, Detroit, MI
- 2008-2010 Assistant Lecturer, Department of Chemistry, University of Kelaniya, Sri Lanka
- 2007-2008 Student Research Assistant, Industrial Technology Institute, Colombo, Sri Lanka

Technical Skills

- Experienced with Powder X-ray Diffraction (PXRD), Transmission Electron Microscopy (TEM), Energy Dispersive Spectroscopy (EDS), Optical Microscopy, UV-Visible and Infra-Red Spectroscopy (UV-vis and FTIR), Atomic Absorption Spectroscopy (AAS), Inductively Coupled Plasma Mass Spectrometry (ICP-MS)
- Handling air sensitive materials and performing synthesis employing inert atmosphere techniques

Publications

- Solution-Phase Growth Mechanism of Phosphorus-doped MnAs Nanoparticles: Size, Polydispersity and Dopant Control on the Nanoscale- Roshini Pimmachcharige, Yanhua Zhang, Rajesh Regmi, Gavin Lawes, Stephanie L. Brock, Journal of Materials Chemistry C, 2017

Professional Affiliations

- American Chemical Society (2012-present)
- Michigan Microscopy and Microanalysis Society (2014-present)
- Sri Lanka Association for the Advancement of Science (2009-present)